Since 1955

Strojniški vestnik
Journal of Mechanical Engineering

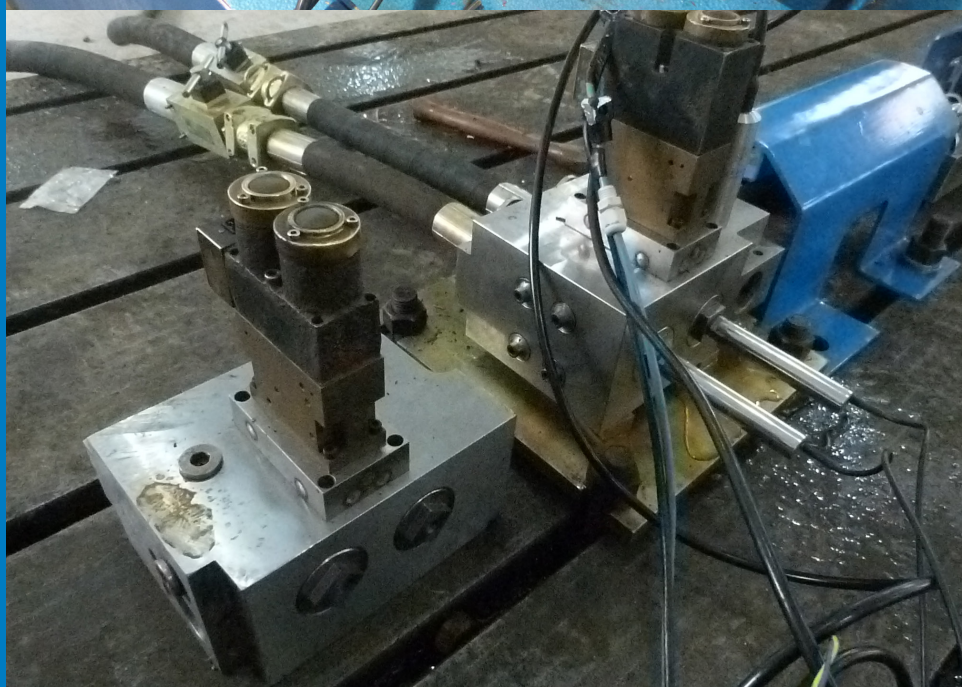

no. 6
year 2015
volume 61

Strojniški vestnik – Journal of Mechanical Engineering (SV-JME)

Aim and Scope
The international journal publishes original and (mini)review articles covering the concepts of materials science, mechanics, kinematics, thermodynamics, energy and environment, mechatronics and robotics, fluid mechanics, tribology, cybernetics, industrial engineering and structural analysis.
The journal follows new trends and progress proven practice in the mechanical engineering and also in the closely related sciences as are electrical, civil and process engineering, medicine, microbiology, ecology, agriculture, transport systems, aviation, and others, thus creating a unique forum for interdisciplinary or multidisciplinary dialogue.
The international conferences selected papers are welcome for publishing as a special issue of SV-JME with invited co-editor(s).

Editorial Office
University of Ljubljana, Faculty of Mechanical Engineering
SV-JME, Aškerčeva 6, SI-1000 Ljubljana, Slovenia
Phone: 386 (0)1 4771 137
Fax: 386 (0)1 2518 567
info@sv-jme.eu, http://www.sv-jme.eu

Print: Grafex, d.o.o., printed in 380 copies

Founders and Publishers
University of Ljubljana, Faculty of Mechanical Engineering, Slovenia
University of Maribor, Faculty of Mechanical Engineering, Slovenia
Association of Mechanical Engineers of Slovenia
Chamber of Commerce and Industry of Slovenia, Metal Processing Industry Association

President of Publishing Council
Branko Širok
University of Ljubljana, Faculty of Mechanical Engineering, Slovenia

Vice-President of Publishing Council
Jože Balič
University of Maribor, Faculty of Mechanical Engineering, Slovenia

Cover:
There is an urgent need of the 1000L/min electro-hydraulic directional valve at present, thus a traditional single-channel valve is designed. A 16 L/min small flow test bench and a 1000 L/min large flow test bench have been established to test the dynamic characteristics of the designed valve, but the valve shows different dynamic characteristics on the two test benches. Then a double-channel valve is designed and also tested on the two test benches to investigate the flow behavior of the large flow valve.

Courtesy: Taiyuan University of Technology, College of Mechanical Engineering, China

ISSN 0039-2480

General information
Strojniški vestnik – Journal of Mechanical Engineering is published in 11 issues per year (July and August is a double issue).

Institutional prices include print & online access: institutional subscription price and foreign subscription €100,00 (the price of a single issue is €10,00); general public subscription and student subscription €50,00 (the price of a single issue is €5,00). Prices are exclusive of tax. Delivery is included in the price. The recipient is responsible for paying any import duties or taxes. Legal title passes to the customer on dispatch by our distributor.

Single issues from current and recent volumes are available at the current single-issue price. To order the journal, please complete the form on our website. For submissions, subscriptions and all other information please visit: *http://en.sv-jme.eu/.*

You can advertise on the inner and outer side of the back cover of the journal. The authors of the published papers are invited to send photos or pictures with short explanation for cover content.

We would like to thank the reviewers who have taken part in the peer-review process.

The journal is subsidized by Slovenian Research Agency.

Strojniški vestnik - Journal of Mechanical Engineering is available on http://www.sv-jme.eu, where you access also to papers' supplements, such as simulations, etc.

Contents

Strojniški vestnik - Journal of Mechanical Engineering
volume 61, (2015), number 6
Ljubljana, June 2015
ISSN 0039-2480

Published monthly

Papers

Strojniški vestnik - Journal of Mechanical Engineering 61(2015)6, 355-364

DOI:10.5545/sv-jme.2015.2487
Original Scientific Paper
Received for review: 2015-02-03
Received revised form: 2015-04-14
Accepted for publication: 2015-05-06

Research and Analysis of the Hysteresis Characteristics of a Large Flow Directional Valve

Yaoyao Liao[1,2] – Hongbing Yuan[1,2,*] – Zisheng Lian[1,2] – Jiling Feng[3] –Yongchang Guo[1,2]

[1] Taiyuan University of Technology, College of Mechanical Engineering, China
[2] Shanxi Key Laboratory of Fully Mechanized Coal Mining Equipment, China
[3] Manchester Metropolitan University, School of Engineering, UK

The 1000 L/min large flow hydraulic system for the hydraulic support used in a coal mine is currently a topic of great interest. The large flow directional valve is a key component for hydraulic systems, so the design of the 1000 L/min large flow directional valve is essential. The designed single-channel valve shows serious hysteresis characteristics in a 1000 L/min large flow condition, but it does not happen in a 16 L/min small flow condition. Based on this phenomenon, the computational fluid dynamics (CFD) technology was used to simulate the flow in the valve. It was discovered that the single-channel caused unbalanced pressure in the annular region and on the surface of the valve spool, so the valve spool is subjected to great radial unbalanced force. Then a double-channel valve was designed to improve the pressure distribution. The simulated radial unbalanced force on the double-channel valve is 67.2% lower than that of the single-channel valve. The experimental results showed that the hysteresis characteristics also disappeared under the 1000 L/min large flow condition. Therefore, the conclusion can be drawn that the hysteresis characteristics of the single-channel valve is due to the radial unbalanced force caused by the unsymmetrical flow field. The results show that the maximum radial unbalanced force the valve spool can withstand is 170 N. Furthermore, symmetrical flow passages have to be taken into account in large flow conditions. This paper provides valuable references for the design of large flow valves.
Keywords: large flow directional valve, radial unbalanced force, hysteresis, CFD, hydraulic roof support

Highlights
- *A combination of CFD and experimental tests was used to study the hysteresis effect.*
- *The hysteresis effect is due to the radial unbalanced force on the valve spool.*
- *The maximum radial unbalanced force the valve spool can withstand is 170 N.*
- *A double-channel valve is designed for the 1000 L/min large flow condition.*
- *Symmetrical flow passages have to be taken into account for large flow valves.*

0 INTRODUCTION

In recent years, many thick coal seams have been discovered, so the larger mining height hydraulic roof support is needed. The bigger cylinder on a large mining height hydraulic roof support requires a larger flow to meet the operating time requirements. There is an urgent need for a 1000 L/min hydraulic system used in the hydraulic roof support. The large flow directional valve is a key component of the hydraulic system, but the present NS12 valve and NS20 valve, of which the flow capacities are 200 L/min and 400 L/min respectively, have difficulty in meeting the large flow demand, so design of the 1000 L/min large flow directional valve (the NS25 valve represents the 1000 L/min large flow valve) is essential.

The existing NS12 valve and NS20 valves both apply the single-channel structure to supply liquid, so the NS25 valve is also designed with the single-channel. Surprisingly, the NS25 valve has insufficient close capability, showing great hysteresis characteristics when switched off on the 1000 L/min large flow test bench, but it exhibits good characteristics on the 16 L/min small flow test bench, so the hysteresis phenomenon is not due to the insufficient spring stiffness. It is highly dangerous in the coal mine if the valve closes slowly, so solving the hysteresis effect of the valve is very essential.

There have been several papers related to the radial unbalanced force on the hydraulic valves. Park **[1]** and **[2]** added pressure-equalizing grooves on the valve spool to prevent the valve spool from getting stuck due to the eccentric gap between the valve spool and the valve sleeve. Zeng et al. **[3]** and Jia et al. **[4]** studied the influences of pressure groove numbers, pressure groove shapes, and pressure groove dimensions on the clamping force of the valve spools. Zhao et al. **[5]** analysed the clamping force due to the thermal deflection of the tethers on a microvalve in a microfuel cell system. A special device was used to reduce the clamping force resulting from the thermal deflection. The thermal stability of the device was simulated via the finite element method.

Computational fluid dynamics (CFD) technology is an effective method for solving problems in fluid engineering. Lisowski et al. **[6]** and Amirante et

*Corr. Author's Address: Taiyuan University of Technology, College of Mechanical Engineering, Yingze West Avenue 79, Taiyuan, China, yhb1961@126.com

al. [7] researched the axial flow forces using CFD technology. Tic et al. [8] used CFD simulation to help design a modern hydraulic tank. Yang et al. [9] researched the cavitation performance through CFD technology. Tsukahara et al. [10] took advantage of CFD to study the vortex flow in a cylinder. Han et al. [11] investigated the flow coefficients of a contra-push check valve through CFD technology. Kocaman [12] even used CFD to predict the backwater profiles when a bridge was designed.

In this paper, in order to make new discoveries about the hysteresis characteristics of the NS25 valve, the CFD code Fluent was used to simulate the fluid flow and the radial unbalanced force on the valve spool.

1 STRUCTURE AND WORKING PRINCIPLE

Fig. 1 shows the schematic diagram of a large flow directional valve used in the hydraulic roof support. Fig. 2 shows the detailed structure of the single-channel NS25 large flow directional valve. All the screw-in cartridge valves are integrated into one valve body. P represents the inlet channel, where the high-pressure liquid is supplied. O stands for the outlet channel, where the low-pressure liquid is back. The upper half of the large flow valve in Fig. 2 is the working state, and the lower half is the off state. The large flow valve is controlled by the pilot valve. When the solenoid valve is powered, the pilot valve opens due to the output force of the solenoid valve, *F*. The pressure liquid would flow to port K which is the control port of the large flow valve. Then the valve spool quickly moves to the right. Thus, the large flow valve begins to work, supplying liquid from P to A. When the power of the solenoid valve is off, the pilot valve and the large flow valve will return to the initial off state.

The problem is that the single-channel NS25 valve shows great hysteresis characteristics when switched off on the 1000 L/min large flow test bench, but it exhibits good characteristics on the 16 L/min small flow test bench. It is clear that both the inlet channel and the outlet channel are connected to one side of the annular region. This may lead to the unsymmetrical pressure on the valve spool. A double-channel NS25 valve was proposed to improve the pressure distribution. CFD technology can then be used to complete the comparison.

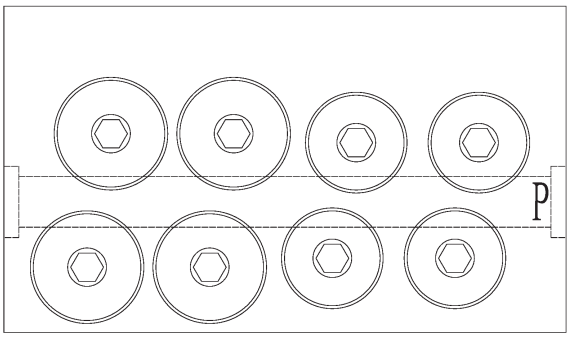

Fig. 1. *Outline of the integrated large flow directional valves*

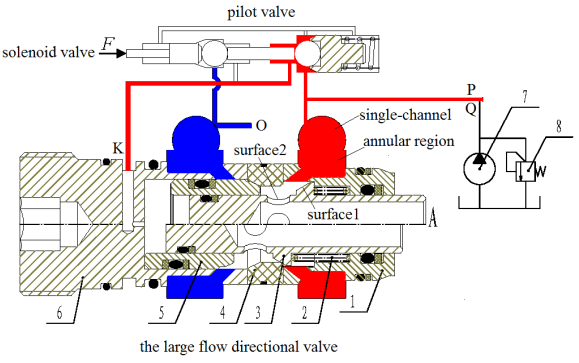

Fig. 2. *Detailed structure of the large flow directional valve; 1-inlet valve sleeve, 2-spring, 3-poppet valve spool, 4-valve seat, 5-return valve spool, 6-return valve sleeve, 7-pump, 8-relief valve*

2 SIMULATION ANALYSIS

2.1 The Models

Two structures, the old single-channel structure and the newly designed double-channel structure, were designed to compare the fluid flow and the unbalanced force on the NS25 valve spool. Fig. 3 shows the two flow passage models of the valve. It is not suitable to use the symmetric boundary condition or the periodic boundary condition because of the unsymmetrical flow characteristics of the valve. In addition, the flow passage of the valve is very complex, so the two completed flow passage models are generated in Pro/engineer software. What needs to be noticed is that the equivalent cross-sectional areas of the inlet channels under the two structures are the same in order to ensure the same average velocities in the inlet channels, which is crucial in the modeling process. The mesh models are generated in Gambit, which is the preprocessor of Fluent. The two flow passage models are meshed with a Tet/Hybrid unit, which is highly appropriate for complex models. The grids

are refined in some critical areas as the enlargement shows in Fig. 4. The grid numbers of the two models are all nearly 1.8 million.

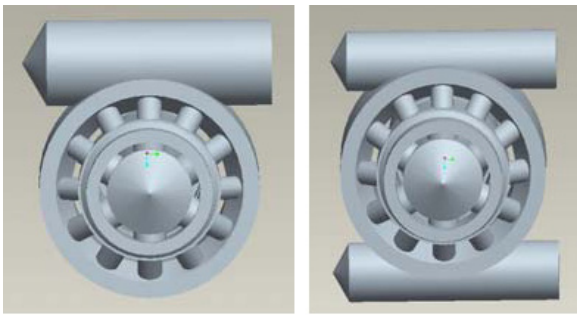

a) b)

Fig. 3. *Flow passage models under two structures; a) single-channel, b) double-channel*

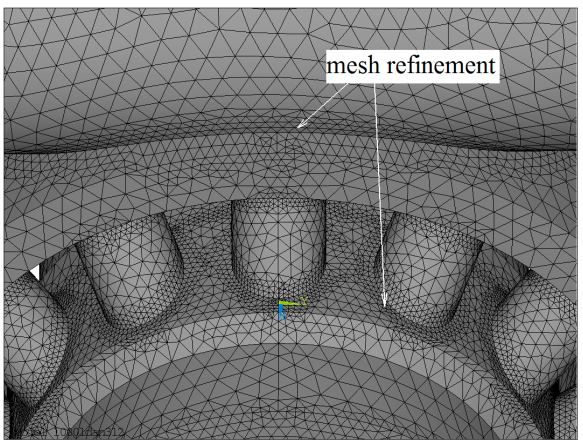

Fig. 4. *Enlargement of the mesh model*

2.2 Boundary Conditions

The pressure-based solver is used to carry out the steady state flow simulation. The renormalization group (RNG) $k-\varepsilon$ model is applied to the turbulent flow. The non-equilibrium wall function is applied for the near-wall treatment to treat the effects of pressure gradient and non-equilibrium. The inlet boundary condition is the velocity inlet. The outlet boundary condition is the pressure outlet, which is at the standard atmospheric pressure. The SIMPLEC algorithm is used. The First-order upwind scheme is used for the discrete equations so as to accelerate the convergence rate.

2.3 Simulation Results and Analysis

Fig. 5 shows the velocity vectors of the central sectional plane across the channel under the single-channel structure. The plane passes through the centre of the inlet channel. It can be seen that the flow field in the annular region differs strongly in the Y- and Y+ directions. Most liquid flows into the annular region in the Y- direction from the inlet channel because the flow path is smooth, which can be seen in the enlargement A. However, there is a sharp corner in the Y+ direction, causing dramatic changes in the flow angle, so only a small amount of liquid flows into the annular region in the Y+ direction, which is clearly displayed in enlargement B. The larger flow leads to a greater velocity in the Y- direction. The liquid in the Y- annular region flows along path line C, and the liquid in the Y+ annular region flows along path line D. The two flows join where the arrows point to in the Y+ direction. Here. the velocity of the flow decreases sharply. According to Bernoulli's equation, the pressure in this area would increase correspondingly, so overall the pressure in the Y+ direction would be higher than that in the Y- direction under the single-channel structure. The velocity vectors of the central sectional plane across the channel under the double-channel structure are shown in Fig. 6. There are confluences in both the Y+ direction (G and H) and Y- direction (E and F) under double-channel structure, while there is a confluence only in Y+ direction under single-channel structure, which is the main difference between the two models. The pressure in the Y- annular region under the double-channel structure also increases, so the unsymmetrical pressure difference between the Y- and Y+ directions would be weakened for the double-channel model. Moreover, the flow field in the Z direction is completely symmetrical.

The above descriptions can be verified in Fig. 7. In the single-channel structure, the pressure of region d in Y+ direction is much higher than that of region b in Y- direction. The corresponding pressure difference is about 3 MPa. However, the pressure difference between region d' and b' in the double-channel structure is almost exactly 1 MPa, which is much lower than that of the single-channel structure. It should be noted that the pressure of region b' is higher than that of region d' because of the larger flow confluence in the Y- direction in double-channel structure. In addition, the pressure of region a is higher than that of region c in single-channel structure because of the unsymmetrical structure. However, in double-channel structure, the pressure of region a' and c' is the same, so not only the pressure difference in Z direction is eliminated but also the pressure difference in Y direction is dramatically weakened.

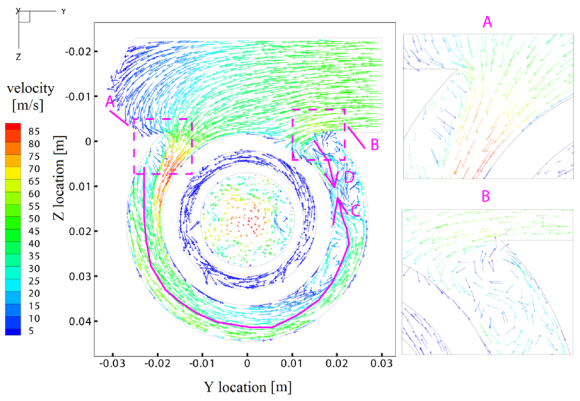

Fig. 5. *Velocity vectors of the central sectional plane across the channel under single-channel structure*

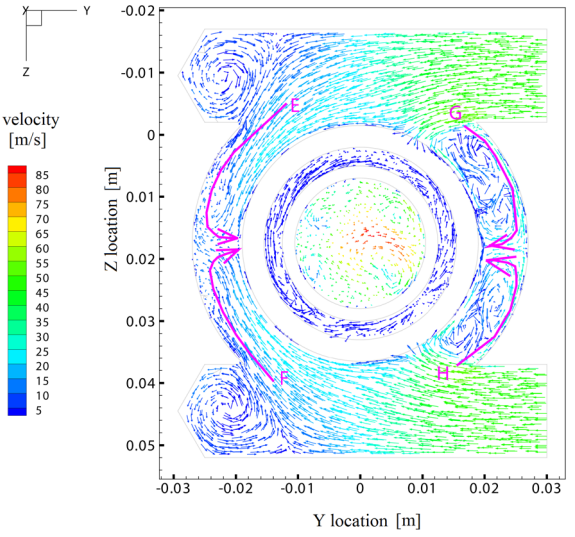

Fig. 6. *Velocity vectors of the central sectional plane across the channel under double-channel structure*

Fig. 8 displays the pressure on the poppet surface1 (see Fig. 2) which is washed by the liquid when the valve is in working state in the two models. It is known that the pressure in Y+ annular region is much higher than that in the Y- direction according to the previous analysis of the single-channel model, so the velocity of the liquid washing on surface1 along the radial holes is bigger in Y+ direction, resulting in much higher pressure on the Y+ poppet surface1 of the valve spool. This result is well displayed in Fig. 8a. In the double-channel model, as Fig. 8b shows, the pressure on surface1 tends to be more balanced because of the weakened pressure difference between the Y+ annular region and the Y- annular region. Comparing Fig. 8a and Fig. 8b, it is known that not only the pressure difference but also the area subjected to great unbalanced pressure is much smaller in the double-channel model.

Fig. 9 shows the pressure on the wall surface2 (see Fig. 2) which is also washed by the liquid when the valve is in working state in the two models. The pressure on surface2 in the two models exhibits similar characteristics to the pressure on the poppet surface1. The pressure on Y+ surface2 is much greater than the pressure in the Y- direction in the single-channel model while it is much closer on both sides in the double-channel model.

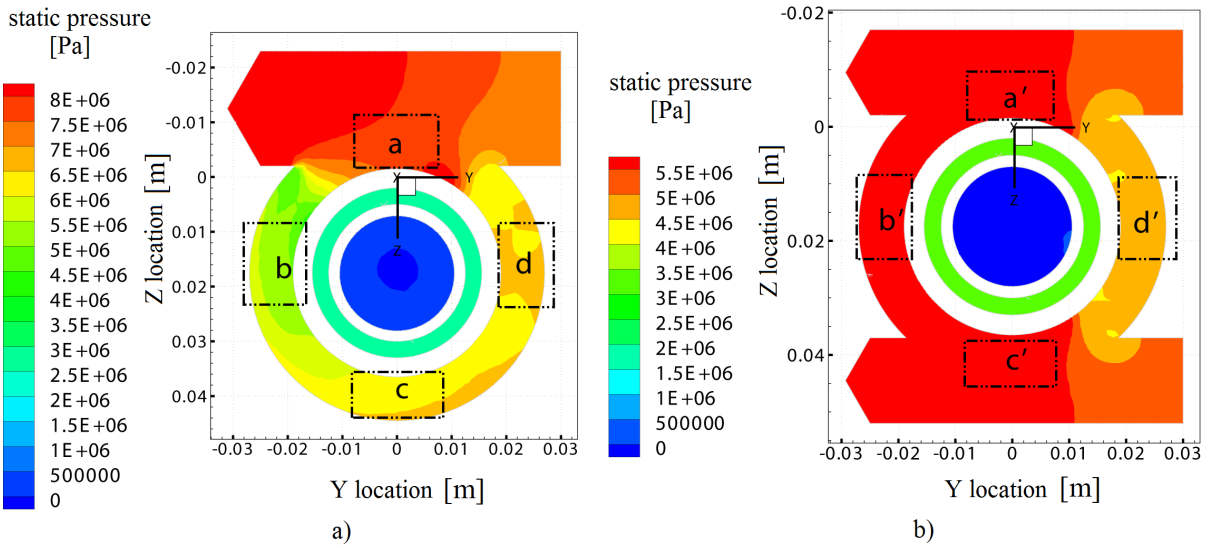

Fig. 7. *Pressure contours of the central sectional plane; a) across single-channel, b) across double-channel*

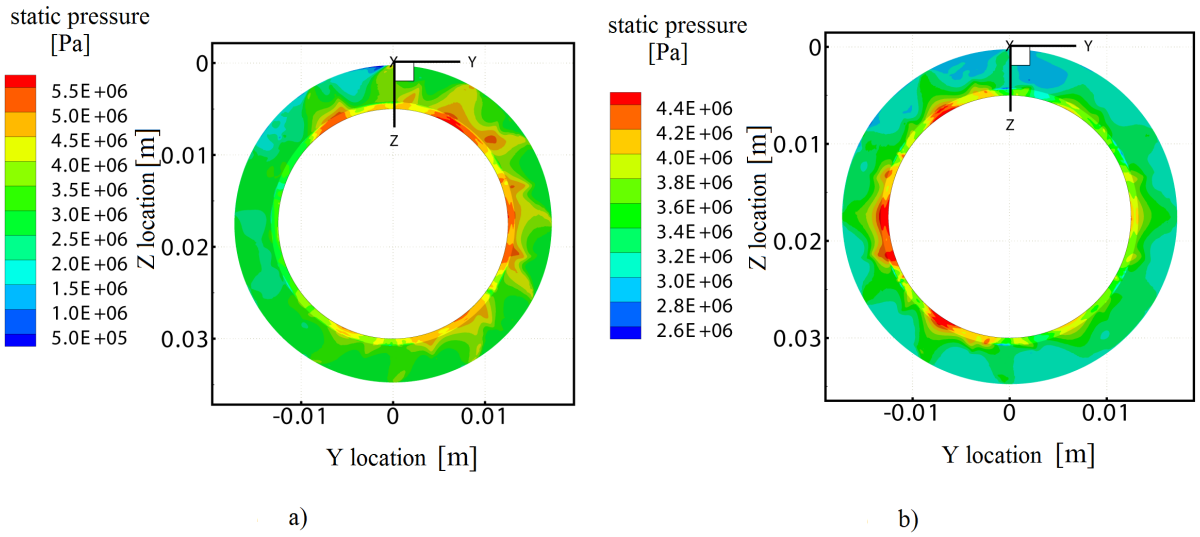

Fig. 8. *Pressure distributions on the poppet surface1 of the poppet valve spool; a) single-channel, b) double-channel*

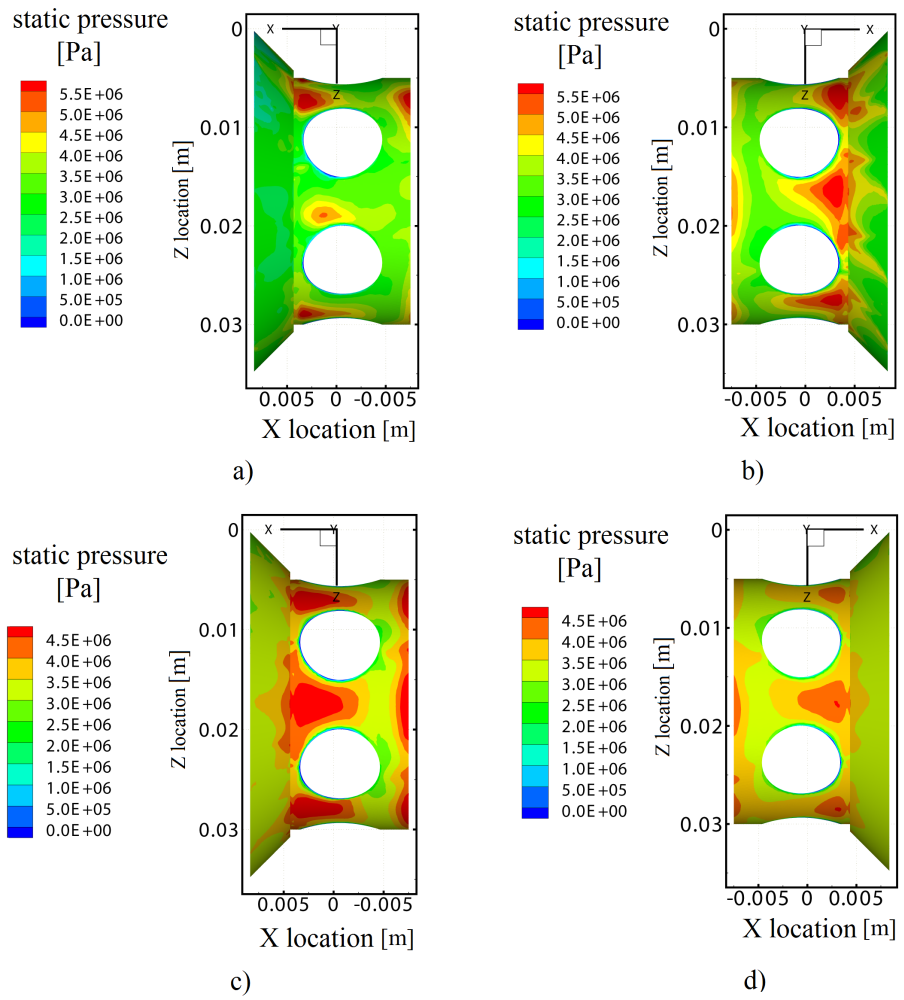

Fig. 9. *Pressure distributions on the wall surface2 of the poppet valve spool; a) single-channel, Y- direction, b) single-channel, Y+ direction, c) double-channel, Y- direction, d) double-channel, Y+ direction*

The unbalanced pressure would produce an unbalanced force on the valve spool. Fig. 10 shows the unbalanced forces on the three valve spools, NS12, NS20, and NS25, with the corresponding nominal flows 200 L/min, 400 L/min and 1000 L/min under the single-channel structure. It is shown that the unbalanced force increases with the increase of nominal flow. The unbalanced force on NS25 valve is up to 250 N, which is about three times than that on NS20 valve. The valve dimensions are bigger while the corresponding rated flow is larger, which results in the larger area subjected to the unbalanced pressure. This can explain the results in Fig. 10. Conclusions can be drawn that it is not suitable to apply the conventional single-channel structure for NS25 valve; otherwise, the unexpected behaviors of the valve may appear during the opening and the closing process.

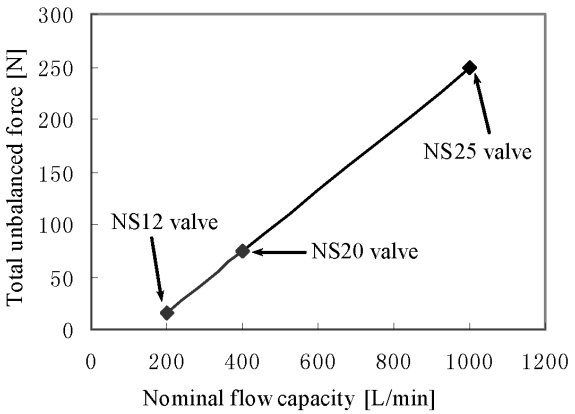

Fig. 10. *Unbalanced forces on the three poppet valve spools*

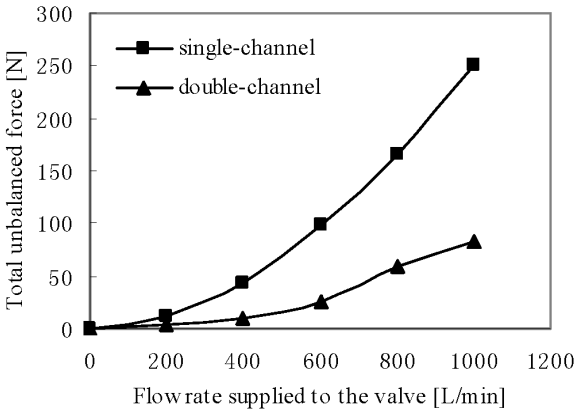

Fig. 11. *Unbalanced forces on the poppet valve spool of NS25 valve under different structures*

Fig. 11 reveals the unbalanced force on the poppet spool of NS25 valve under the two structures. The unbalanced force on the valve spool under double-channel structure is much lower than that of the single-channel structure. When the flow rate supplied to the NS25 valve reaches its nominal flow, 1000 L/min, the unbalanced force under double-channel model is just 82 N, 67.2 % lower than that of the single-channel model, nearly equal to that of the NS20 valve at its nominal flow, 400 L/min. Therefore, the double-channel structure has significant effects on decreasing the unbalanced force on large flow valves.

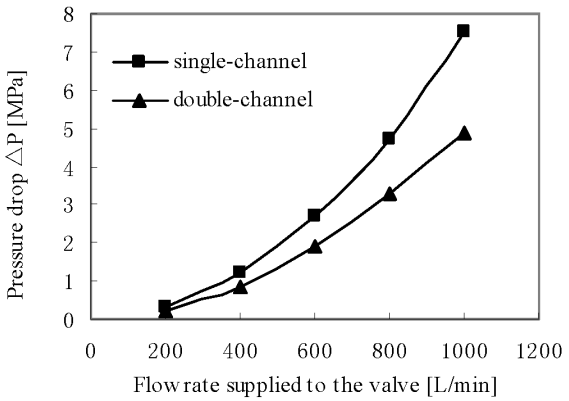

Fig. 12. *Pressure drops of the DN25 valve under different structures*

Fig. 12 displays the pressure drop characteristics of NS25 valve under the two structures. Because of the larger flow area between the inlet channel and the annular region, the flow resistance decreases, the pressure drop under double-channel structure is lower than that of the single-channel structure, so the double-channel structure is also helpful for energy saving. The effect is more obvious at its nominal flow of 1000 L/min. The energy saving rate is 34.7 %.

3 EXPERIMENTAL TESTS

3.1 Experimental Setup and Principle

The single channel valve and the double channel valve were manufactured, and the responses of the valve displacement in the valve returning process were tested to compare the hysteresis characteristics of the two valves. The experimental tests are carried out in two flow conditions, the 16 L/min small flow condition and the 1000 L/min large flow condition, as Fig. 13 shows. The 16 L/min small flow is easy to get on the small flow test bench because the rated flow is 16 L/min, but the 1000 L/min large flow is not easy to obtain because it is hard to get such a large flow

pump, so a large accumulator was used to provide the 1000 L/min large flow, as Fig. 13c shows.

Fig. 14 shows the experimental principle of the large flow test bench. The valve displacement was tested by the displacement sensor, and the flow was tested by a flow gauge. The throttle valve was used to adjust the back pressure. Before the test, the accumulator should be filled with liquid to a certain pressure that can be set according to the simulation results to ensure the 1000 L/min steady flow. The tests

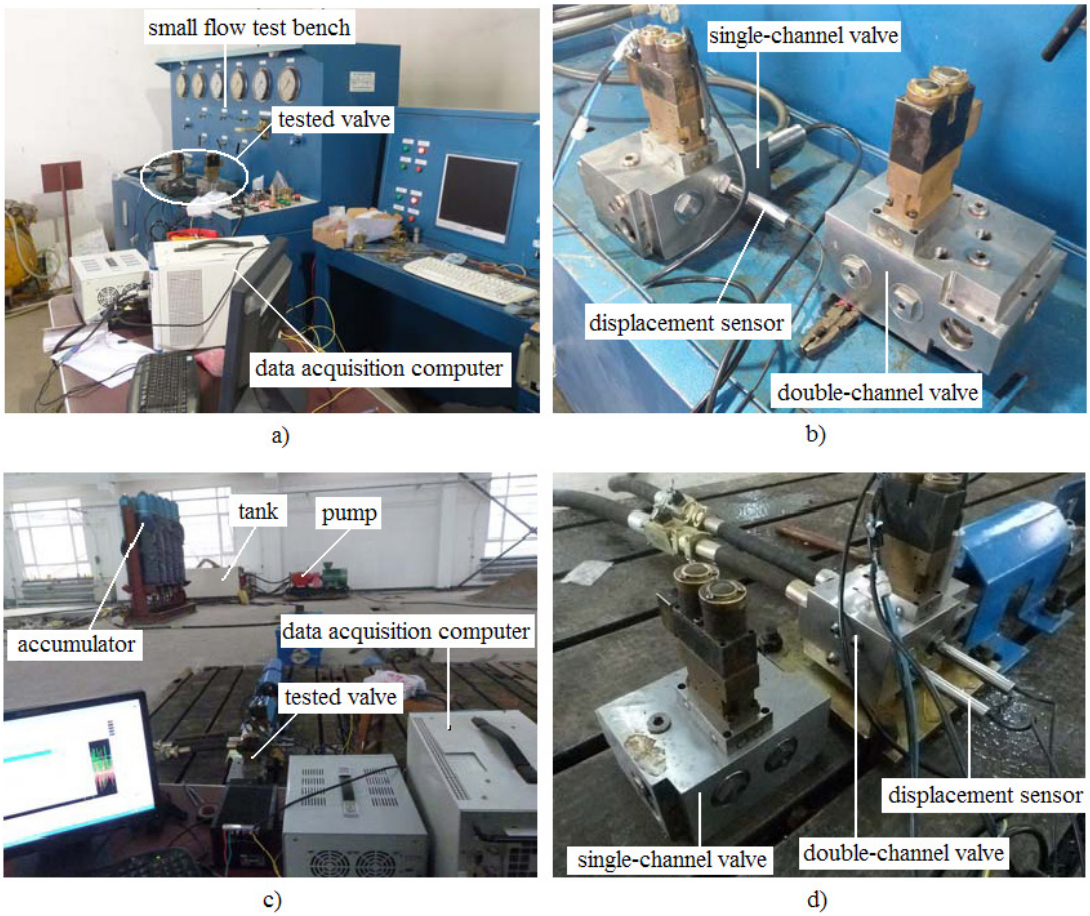

Fig. 13. *The two flow condition test benches; a) 16 L/min small flow test bench, b) the two tested valves under small flow conditions, c) 1000 L/min large flow test bench, d) the two tested valves under large flow conditions*

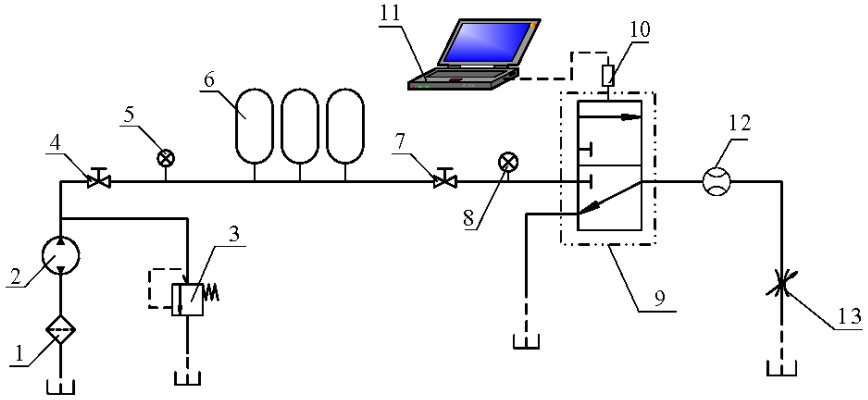

Fig. 14. *The experimental principle; 1- filter, 2-pump, 3-relief valve, 4,7-shut-off valve, 5,8-pressure gauge, 6-accumulator, 9-tested valve, 10-displacement sensor, 11-data acquisition computer, 12-flowmeter, 13-throttle valve*

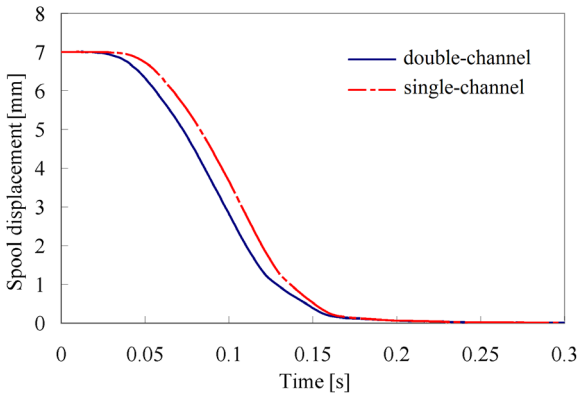

Fig. 15. *Displacement curves of the two valves under 16 L/min small flow condition*

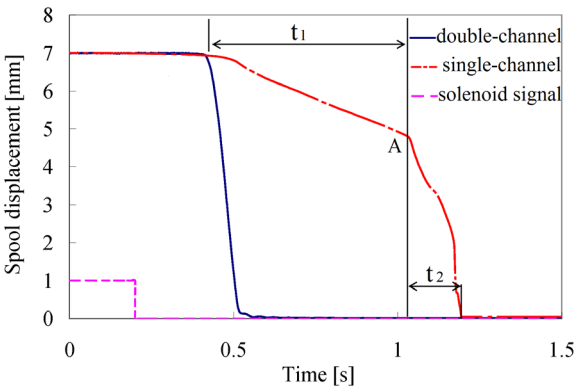

Fig. 16. *Displacement curves of the two valves under 1000 L/min large flow condition*

Table 1. *The results of the three test groups*

No.	Valve type	Inlet pressure [MPa]	Outlet pressure [MPa]	Flow [L/min]	Moving time [ms]		
					t_1	t_2	t_1+t_2
1	Single-channel	7.5	0	1000	600	200	800
	Double-channel	5				150	
2	Single-channel	11.5	4		580	200	780
	Double-channel	9				130	
3	Single-channel	4.7	0	800	200	150	350
	Double-channel	3.3				140	
4	Single-channel	8.7	4		190	150	340
	Double-channel	7.3				130	
5	Single-channel	2.7	0	600		150	
	Double-channel	1.9				140	
6	Single-channel	6.7	4			130	
	Double-channel	5.9				130	

can begin when the 1000 L/min steady flow is well adjusted. It is imperative to note that the stiffness of the reset spring remains constant to avoid its influence on the results of the different tests.

3.2 Experimental Results

Fig. 15 shows the displacement curves of the two valves in the returning process under the 16 L/min small flow condition. It can be seen that the two valves close rapidly and nearly have no hysteresis effect. However, in the 1000 L/min large flow condition test, the single-channel valve shows serious hysteresis characteristics compared with the double-channel valve as displayed in Fig. 16. The double-channel valve closes in about 0.3 s when the solenoid valve is turned off, but the single-channel valve needs about 1 s to complete the process. The hysteresis effect happens mainly when the valve spool begins to move. The movement time of the double-channel valve is about 150 ms. However, the movement time of the single-channel valve is 800 ms. Furthermore, the displacement curve of the single-channel valve shows two time periods clearly, t_1 and t_2, which are 600 ms and 200 ms respectively. It can be seen that the hysteresis effect happens mainly during the t_1 period. This can be explained as follows: the valve opening is large during the t_1 period, and the flow is also large, the friction force is big due to the great unbalanced force on the valve spool, so the single-channel valve closes slowly, showing strong hysteresis characteristics. When the valve turns off at point A, which is the end of t_1 and the beginning of t_2, the valve opening is smaller, and the flow is much less, therefore the unbalanced force on the valve spool decreases greatly, so the hysteresis effect is much weaker during t_2 period.

A number of tests have been carried out under different boundary conditions. The results are listed in Table 1. These results show that the movement time of the two valves is nearly the same when the flow decreases to 600 L/min; in other words, there is no hysteresis effect when the flow is below 600 L/min. The hysteresis effect increases sharply when the flow rises from 800 L/min to 1000 L/min. In other words, the hysteresis effect begins to show apparently when the flow reaches up to 800 L/min. According to the simulation results in Fig. 11, it can be concluded that the maximum radial unbalanced force that the valve spool can withstand is 170 N; otherwise, the hysteresis effect will occur.

4 DISCUSSIONS AND CONCLUSIONS

Based on the hysteresis phenomenon of the old single-channel NS25 valve, the paper researched the radial unbalanced forces on the valves with CFD technology. The conventional single-channel structure leads to unsymmetrical flow field in the annular region, which results in unbalanced pressure on the poppet spools. The radial unbalanced forces are mainly generated on the poppet surface and the nearby surface washed by the high-pressure liquid. For the common NS12 valve and NS20 valve, the radial unbalanced forces are just 15 N and 75 N. The hysteresis characteristics are not obviously shown on these two valves because the radial unbalanced forces are small. However, when the nominal flow capacity increases, the corresponding valve dimensions also increase, which results in a larger area subjected to the unbalanced pressure. The radial unbalanced force on the NS25 valve rises to 250 N at its nominal flow, leading to great friction force on the NS25 valve, so the single-channel NS25 valve shows that there is insufficient shut-off capability. Then a novel double-channel structure was proposed to improve the pressure distribution using the knowledge of Bernoulli's equation. The radial unbalanced force on the spool of the double-channel NS25 valve decreases by 67.2 % compared to that of the single-channel valve, just 82 N, and the hysteresis effect disappeared in the 1000 L/min flow condition test. Moreover, the double-channel valve has the larger flow area between the inlet channel and the annular region; as a result, the flow resistance decreases accordingly. The pressure drop of the double-channel valve is 34.7 % lower than that of the single-channel valve, so it is also significant for energy saving.

In summary, the innovations and contributions of this paper are:

(1) The small flow and the large flow conditions were used to implement the experimental tests. The results indicated that the hysteresis phenomenon of the single-channel NS25 valve was not due to the stiffness of the spring, but the radial unbalanced force resulted from large flow condition.
(2) The maximum radial unbalanced force that the valve spool can withstand is 170 N, which is obtained through a combination of two methods: the CFD technology and the experimental tests. Thus, the CFD simulation can be used to replace the experimental tests when a larger flow valve is designed in the future, thus resulting in financial saving and time saving.
(3) The mechanism of producing radial unbalanced force in this paper is different from that of the previous papers. This paper applied the double-channel structure rather than the common pressure grooves to treat the unbalanced force. Furthermore, it is not suitable to use a larger stiffness spring to treat the hysteresis characteristics of the single-channel NS25 valve, because the great friction force caused by the radial unbalanced force would result in the wear and tear of the valve spool and the seals.
(4) Symmetrical flow passages have to be taken into account when a large flow hydraulic component is designed in the future.

5 ACKNOWLEDGEMENTS

The authors thank the support of Shanxi Science and Technology Department, under the projects number 20111101025 and MJ2014-07. We also thank the support of the Science and Technology Innovation Fund of Taiyuan University of Technology.

6 REFERENCES

[1] Park, S.H. (2009). Development of a proportional poppet-type water hydraulic valve. *Proceedings of the Institution of Mechanical Engineers, Part C: Jounal of Mechanical Engineering Science*, vol. 223, no. 9, p. 2099-2107, **DOI:10.1243/09544062JMES1380**.

[2] Park, S.H. (2009). Design and performance characteristic analysis of servo valve-type water hydraulic poppet valve. *Journal of Mechanical Science and Technology*, vol. 23, no. 9, p. 2468-2478, **DOI:10.1007/s12206-009-0705-9**.

[3] Zeng, Q.L., Cui, J., Zhao, W.M. (2012). Simulation analysis for hydraulic clamping force of bidirectional hydraulic lock' valve spool based on Fluent. *Advanced Materials Research*, vol. 542-543, p. 1091-1095, **DOI:10.4028/www.scientific.net/AMR.542-543.1091**.

[4] Jia, W.H., Yin, C.B., Cao, D.H. Yi, Y. (2013). The gap seal's influences on the leakage and clamping of multi-way directional valves. *Sensors and Transducers*, vol. 23, p. 44-48.

[5] Zhao, H.B., Stanley, K., Wu, Q.M.J., Czyzewska, E.(2005). Structure and characterization of a planar normally closed bulk-micromachined piezoelectric valve for fuel cell applications. *Sensors and Actuators, A: Physical*, vol. 120, no. 1, p. 134-141, **DOI:10.1016/j.sna.2004.11.037**.

[6] Lisowski, E., Czyżycki, W., Rajdab, J. (2013). Three dimensional CFD analysis and experimental test of flow force acting on the spool of solenoid operated directional control valve. *Energy Conversion and Management*, vol. 70, p. 220-229, **DOI:10.1016/j.enconman.2013.02.016**.

[7] Amirante, R., Del Vescovo, G, Lippolis, A. (2006). Evaluation of the flow forces on an open center directional control valve by means of a computational fluid dynamic analysis. *Energy Conversion and Management*, vol. 47, no. 13-14, p. 1748-1760, **DOI:10.1016/j.enconman.2005.10.005**.

[8] Tič, V., Lovrec, D. (2012). Design of modern hydraulic tank using fluid flow simulation. *International Journal of Simulation Modelling*, vol. 11, no. 2, p. 77-88, **DOI:10.2507/IJSIMM11(2)2.202**.

[9] Yang, W., Xiao, R.F., Wang, F.J., Wu, Y.L. (2014). Influence of splitter blades on the cavitation performance of a double suction centrifugal pump. *Advances in Mechanical Engineering*, vol. 2014, Art. ID 963197, **DOI:10.1155/2014/963197**.

[10] Tsukahara, T., Ishikawa, M., Kawaguchi, Y. (2013). DNS study of the turbulent Taylor-Vortex flow on a ribbed inner cylinder. *Advances in Mechanical Engineering*, vol. 5, Article ID 628490, 12 pages, **DOI:10.1155/2013/628490**.

[11] Han, H., Guang, Z.M., Qi, Y.Y. (2011). Hydrodynamic characterization and optimization of Contra-push check valve by numerical simulation. *Annals of Nuclear Energy*, vol. 38, no. 6, p. 1427-1437, **DOI:10.1016/j.anucene.2011.01.013**.

[12] Kocaman, S. (2014). Prediction of backwater profiles due to bridges in a compound channel using CFD. *Advances in Mechanical Engineering*, vol. 6, Article ID 905217, **DOI:10.1155/2014/905217**.

Strojniški vestnik - Journal of Mechanical Engineering 61(2015)6, 365-373
DOI:10.5545/sv-jme.2014.2178
Original Scientific Paper
Received for review: 2014-09-12
Received revised form: 2015-02-05
Accepted for publication: 2015-04-22

Superplastic Forming of a Three-Stage Hemispherical 5083 Aluminium Profile

Muthusamy Balasubramanian[1] – Pasupathy Ganesh[2] –
Kalimuthu Ramanathan[3] – Velukkudi Santhanam Senthil Kumar[2,*]

[1]Anna University, University College of Engineering-Ramanathapuram, India
[2]Anna University, College of Engineering-Guindy, India
[3]Alagappa Chettiar College of Engineering and Technology-Karaikudi, India

Three-stage superplastic blow forming characteristics of 5083 aluminium sheets in a hemispherical die cavity have been studied as a function of forming pressure, die entry radius, coefficient of friction, forming time and forming height, both experimentally and using finite element method in this work. Optimum forming pressure for achieving uniform thickness in a complex three-stage radius dome profile has been established. Variations in thickness profile are observed experimentally and in FEM analysis in three different die entry regions. The thickness profile has also been predicted as a function of the friction coefficient and die entry radius. The changes in pole thickness, relative height and relative radius of the profile along with the thinning factor are discussed.

Keywords: superplastic forming, three-stage radius hemispherical shape, experimental, FEM, 5083 Al alloy

Highlights

- *Three-stage hemispherical profile has been performed by single blow forming operation.*
- *Optimum pressure conditions were predicted to obtained uniform thickness distribution in a proposed parametric model.*
- *Finite element modelling results were found to be in fair agreement with the experimental results.*
- *Minimum forming time and uniform thickness profile obtained from function of friction coefficient.*
- *Analysis and obtained uniform thickness profile with a function of die entry radius.*

0 INTRODUCTION

Superplastic forming plays an important role in many industrial and aerospace applications. It is a superior technique for causing large amounts of deformation under low strain rates and flow stresses, in comparison with techniques such as deep drawing [1] and [2], hot rolling [3], cold rolling [4], incremental forming [2], [5] and [6] and other heat treatment processes [7].

Studies on superplastic forming techniques are frequently based on single-stage forming operations. For example, Jovane [8] has determined superplastic forming parameters, such as k and m, by varying the applied pressure in increments and thus optimized the pressure at which change in strain rate becomes insignificant. Luckey et al. [9] have developed a two-stage complex dome employing a superplastic forming process in order to improve the thickness profile and prevent wrinkling effects in AA 5083 alloy sheets. Ragab [10] has examined sticking between the contact surface of the sheet and die in the single-stage forming of a cylindrical cup and further investigated thickness distribution under plane-strain conditions. Aoura et al. [11] have proposed a constant stress control method combined with a pressure prediction algorithm to maintain maximum strain rate during the bulge forming process to obtain uniform thickness distribution in a conical cup in a single stage.

Karthikeyan et al. [12] have reported micro-structural changes for better mechanical properties and formability characteristics of AA 6063-T6 alloy in a multiple friction stir-processing method of a hemispherical cup. Yogesha and Bhattacharya [13] have analysed a single stage hemispherical dome for its superplastic deformation characteristics in terms of micro-structure, forming time, thickness strain, pole thickness, thinning factor and temperature using a Ti-Al-Mn alloy. Senthil Kumar et al. [14] have studied the forming of a single stage hemispherical die, both experimentally and using the finite element method in terms of relative height, forming time, pressure, temperature and thickness distribution.

Pradeep et al. [15] have investigated the effect of coefficient of friction between the surface of the die and the sheet, and reported uniform thickness distribution at lower friction values. Xiaomei and Steven [16] have investigated the effects of sheet thickness, flow stress distribution, target stresses, grain size and contact accuracy between the alloy sheet and the ceramic die on the superplastic forming of the Ti-6Al-4V alloy by incorporating a dental ridge augmentation membrane (RAM). Luckey et al. [17] have developed a pressure prediction algorithm in

*Corr. Author's Address: Anna University, Department of Mechanical Engineering, CEG Campus, Chennai-600 025, Tamil Nadu, India, vssk70@gmail.com

order to maintain a predetermined strain rate under the average scheme method and reported 20 % of the average scheme to improve the pressure cycle and maintain target strain rate throughout the forming cycle.

Ng et al. [18] have studied the prediction of localized thinning and thickness distribution in a superplastic forming sheet by introducing a new set of element sizes, mass scaling, and adaptive meshing processes. Jarrar et al. [19] have reported an approach for predicting the gas pressure profile variation as a function of time. This approach combines the pressure with a material constitutive model implemented in ABAQUS for predicting the pressure profile. Wu [20] has analysed the cavitations of SP5083 aluminium alloy in a single stage rectangular pan. It has been found that a two-step strain rate process has reduced the cavitations during superplastic forming. Dezelak et al. [21] have analysed the effect of twist spring back method for a metal sheet by using elastic-plastic shell elements in a FEM simulation. Hojjati et al. [22] investigated the optimization of SPF parameters by employing the hydro forming process for an AA5083 alloy and proved that the maximum strain rate could be controlled via a logarithmic algorithm.

Though extensive research has been carried out using the single-stage superplastic forming of aluminium alloys, such as AA 5083, studies on these materials involving two or more stages of forming in a hemispherical die are very limited. Applications such as aircraft wings, automobile exterior components, and turbine blades have various dimensions to be created in a single-forming operation. In such situations, prior knowledge based on a multistage (three-stage) superplastic forming operations will be highly relevant. In this research work, therefore, an attempt has been made to investigate the three-stage superplastic forming of AA5083 (three different die radii with parametric design) in a hemispherical die. Parameters such as forming height, pole thickness, thickness distribution, average thickness, thinning factor, and forming time, have been studied as a function of forming pressure, friction coefficient and die entry radius in a three-stage parametric model.

1 EXPERIMENTAL PROCEDURE

Uniaxial tensile tests were carried out at different temperatures in order to identify the optimum temperature for the superplastic forming of AA5083, the chemical composition of which is given in Table1. From the hot tensile test results, the optimum temperature was identified as 450 ºC at an initial strain rate of $(\dot{\varepsilon})$ 1.2 $\times 10^{-3}$ s^{-1}, strain rate sensitivity index, m, of 0.3, material constant, k, of 159 MPa/s and flow equation of $\sigma = k\,\dot{\varepsilon}^{m}$, where σ is flow stress.

Table 1. *Chemical composition of AA 5083 alloy (% weight)*

Si	Fe	Cu	Mg	Mn	Cr	Zn	Ti	Al
0.128	0.185	0.001	0.171	2.96	0.052	0.051	0.023	Balance

The experimental setup is shown schematically in Fig. 1. The superplastic forming die consists of male and female parts. The female part consists of three die radii of 18 mm, 27 mm and 30 mm with the first die entry radius of 3 mm, while the second and third die entry radius are each of 1 mm. The die radius is in the ratio of 6:9:10 and represented in the parametric design as 6α:9α:10α, where α is the parametric value. Correspondingly, the three dome depths are in the ratio of 4:3:3 (12 mm, 9 mm and 9 mm in height).

A 70-mm diameter slot was provided in the female die with a depth of 1 mm. The entire die setup, consisting of both the male and female parts, was surrounded without any air gap by a band heater and the entire assembly was placed in a 100 kN hydraulic press under air tight conditions. The die setup was heated up to the desired temperature of 450 °C and maintained until the experiment was completed. The 70-mm diameter and 1.5 mm thick specimens kept between male and female parts. Next, constant argon gas pressure was applied and used to measure the different stages of bulge height as a function of forming time through the LVDT arrangement.

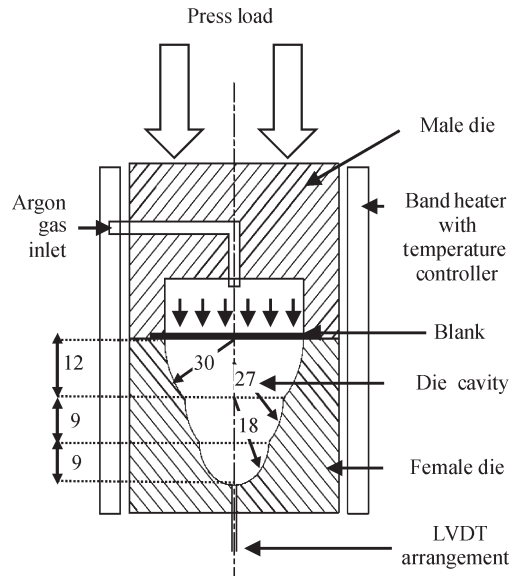

Fig. 1. *Schematic arrangement of three stage die*

For three-stage superplastic forming, pressure was varied from 0.1 MPa to 0.8 MPa and for each pressure, superplastic forming experiments were conducted at (5, 8, 9, 10, 12, 15, 18, 20, 25, 27, 29 and 30) mm of bulge height to predict the optimum pressure required for uniform thickness distribution. For each bulge height, individual components were formed and the parameters of pole thickness, thickness distribution, relative bulge height, relative bulge radius, forming time, average thickness and thinning factor were determined.

2 FINITE ELEMENT ANALYSES

The three-stage superplastic forming process has been simulated by finite element analysis (FEA) using ABAQUS. In the pre-processing stage of FEA, the geometry of the die is assumed as discrete rigid and the blank material as an elasto-plastic deformation body. 3D finite element analysis for a quarter section has been performed. The blank was meshed with the shell element [17] with 1597 nodes; the rigid die was meshed with the R3D3 element and the nodes formed in the die were 1542.

The blank was placed over the die, its periphery was firmly clamped along the rigid die with the boundary conditions ($U_1 = U_2 = U_3 = UR_1 = UR_2 = UR_3 = 0$) as shown in Fig. 2, and constant pressure was then applied uniformly over the entire blank surface. The blank behaved like an elasto-plastic material in the manner expected according to the Newton-Raphson method.

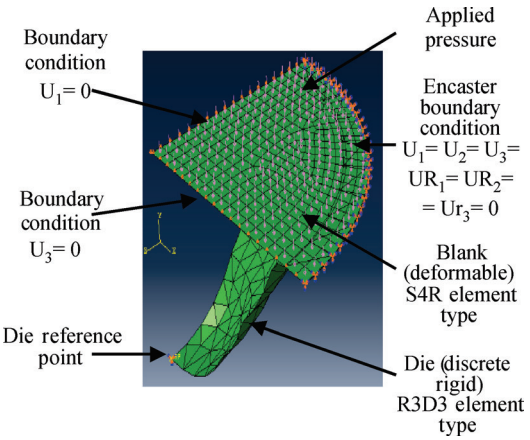

Fig. 2. *Boundary conditions for superplastic forming process*

FEA was carried out using Coulomb's friction condition. The coefficient of friction values were kept at 0, 0.2 and 0.4 between the die surface and the blank. An optimum value of the coefficient of friction was determinedin order to obtain uniform thickness in all the three stages of the profile.

In the solution phase, displacement with respect to time, pole thickness, thickness distribution, forming time, relative bulge height and relative bulge radius were declared as variables to be determined at constant pressure, different coefficients of friction for each pressure and different die entry radius. In

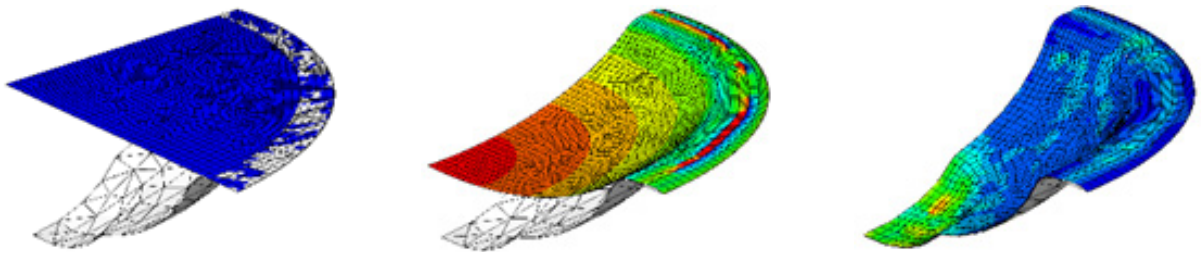

a1) Before forming (t=0) *a2) During forming (t=12 min)* *a3) End of forming (t=19.9 min)*

b1) Before forming (t=0) *b2) During forming (t=12 min)* *b3) End of forming (t=20.2 min)*

Fig. 3. *Various stages of superplastic forming in a) FEA and b) during experiment at 0.5 MPa with function of time*

the post-processor phase, various SPF parameters are obtained.

Fig. 3a and b shows different stages of superplastic forming components both in FEA and actual experiments.

3 RESULTS AND DISCUSSIONS

The three-stage superplastic forming behaviour of the AA5083 alloy has been experimentally studied as a function of pressure, forming height, coefficient of friction and die entry radius. During the experiments, the optimum temperature of 450 °C for a specific forming period was maintained until the perfect forming of the profile was achieved. This is in contrast with single-stage superplastic forming, for which the formation of the profile is relatively simple. The results of the experiments conducted under closely monitored conditions are discussed in the following section.

3.1 Relationship between Forming Pressure and Forming Time to Reach Maximum Height

Relative forming height, the ratio between instantaneous forming height and the actual height (h_i/h), has been followed as a function of forming time at different pressure levels; the results are shown in Table 2 and in Fig. 4. From Table 2, it can be observed that the forming time decreases with increasing forming pressure in the stepped profile.

For example, the time required to reach the final height is about 124 minutes at a pressure of 0.1 MPa but on increasing to 0.2 MPa, the time dropped by half, to 65 minutes. Therefore, when the pressure is increased, the time decreases significantly and a better shape of the profile is obtained.

The final forming height values determined from actual experiments have been found to be very close to the values obtained using finite element model, with a maximum percentage error of 2.73 % at 0.1 MPa.

The prediction of the forming height as a function of pressure and forming time by the FEM and the values obtained through the experiments agree very well with the minimum error at still higher pressures, as can be seen from Table 2.

Variation in relative bulge height as a function of time and pressure is plotted in Fig. 4. It is observed that the forming time decreases with increasing pressure. The sigmoidal variation of bulge height with time may be attributed to the relatively large stresses existing in the early stages of forming, as the relative height (h_i/h) is small.

Table 2. Effect of pressure on final forming time to reach the maximum height (h_i/h =1)

Pressure [MPa]	Final forming time [min]		Error in forming time [%]
	Experimental	FEM	
0.1	124.4	121.1	2.73
0.2	65.3	63.8	2.35
0.3	38.8	37.8	2.65
0.4	25.2	24.6	2.44
0.5	20.2	19.9	1.51
0.6	16.1	15.8	1.89

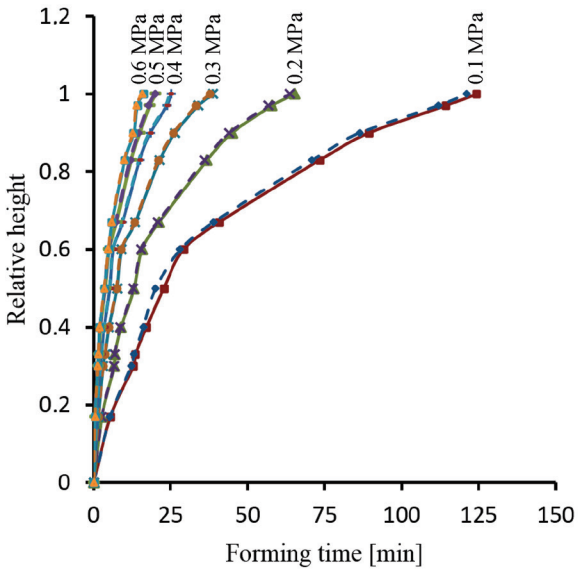

Fig. 4. *Variation of relative bulge height (h_i/h) with time*

3.2 Relationship between Forming Height and Relative Radius (r_i/r)

The relative radius is defined as the ratio of instantaneous radius r_i to the corresponding base radius r of each stage. For the determination of the instantaneous radius, the dome is divided into thin concentric rings during blow forming, and the radius of any particular ring r_i has been measured with reference to the central axis. The change in relative radius as a function of forming height is shown in Fig. 5. It is evident that both height and radius change simultaneously during blow forming throughout the first stage of the radius. At the end of first stage (Point B), there is a small rise in radius with respect to height, which continues to rise gradually until the end of second stage (Point C) beyond which a predominant change in radius can be observed as the height increases further. After this significant rise at the beginning of stage 3, the radius starts

decreasing rapidly as the increase in height becomes more prominent than the change in radius until reaching the final height. The relative radius obtained experimentally and the finite element model follow the same trend as a function of forming height with minor variations observed from stage 1 to stage 2 and stage 2 to stage 3 of forming.

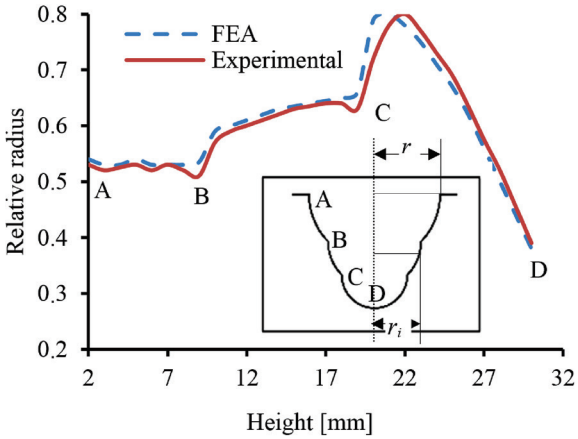

Fig. 5. *Relative radius as a function of forming height at 450 °C*

3.3 Relationship between Forming Height and Pole Thickness

It is generally observed that the pole thickness gradually decreases as a function of forming height in most of the single-stage forming operations. In the present work, however, discontinuities are observed in an otherwise gradual reduction of thickness at pole points where the forming process changes from stage 1 to stage 2 and stage 2 to stage 3, as shown in Fig. 6.

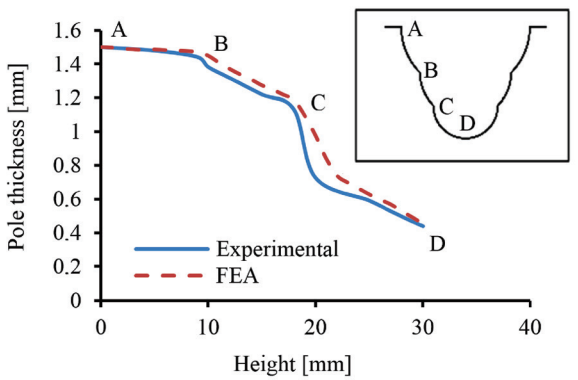

Fig. 6. *Pole thickness as a function of forming height at 450 °C*

The pole thickness does not show any appreciable reduction as a function of forming height during the first stage. However, the reduction in pole thickness is significant when the forming process approaches the second stage, and it is predominant during the third stage of forming. It is clearly indicated that thickness decreases gradually until the sample contacts the first stage radius of die where the blank is more likely to stick to the die surface leading to a drop in thickness; this is also observed during the second stage. The blank continues blow forming during the third stage, and the thickness decreases continuously as a function of the forming height, which ultimately reaches the pole height. It is seen from Fig.6 that the experimental values are in good agreement with the FEA results, with the maximum percentage error of 1.9.

3.4 Effect of Time and Pressure on Pole Thickness

The variation of pole thickness as a function of time at different pressures ranging from 0.1 MPa to 0.6 MPa is presented in Fig. 7. The forming time has been found to decrease upon increasing the pressure. Both the experimentally determined and the finite element modelled dome thickness, average thickness and thinning factor values of the fully formed final components at different pressures are given in Tables 3 and 4, respectively. On comparison of these values, it can be seen that the experimental and FEA values are in good agreement.

The data in Tables 3 and 4 indicate that though variation in thinning factor is not significant as a function of applied pressure, the highest value is found to be at a pressure of 0.5 MPa followed by a drop in thinning factor when the pressure is increased further. The thinning factor, the ratio of thickness at the dome to the average sheet thickness, plays a vital role in predicting the uniformity of thickness in the formed profile with the highest value indicating more uniform thickness in the product.

Therefore, from the experimental result, it may be understood that, in this case, the uniform thickness has been achieved when optimum applied pressure is at 0.5 MPa. As the pressure is increased beyond 0.6 MPa, tearing in the blank sheet occurs at a particular height and pole thickness, as shown in Fig. 8, and the corresponding experimental values of forming height, forming time and thickness are shown in Table 5. Finally it is observed that 0.5 MPa constant pressures was the optimum value at the given specified model.

3.5 Effect of Friction Coefficient on Thickness Profile

Friction is an important parameter to be considered during the superplastic forming of components. The SPF process is numerically simulated using three

different coefficient of friction (μ) values. The five important forming parameters, such as thickness distribution, dome thickness, average thickness, thinning factor and forming time are observed by varying the coefficient of friction. The friction is assumed to be uniform along the contact surface with coefficient values of 0.0, 0.2 and 0.4 for FEA analysis. Fig. 9 shows the thickness distribution obtained by FEA with various coefficients of friction values (0, 0.2, 0.4) under 0.5 MPa. Once the material starts flowing, the initial contact between the die and the blank takes place at the die entry point. Due to sliding under pressure, the thickness of the profile varies as a function of friction coefficient.

The thickness decreases if the coefficient of friction is high and vice versa. The results of the FEA analysis show that the thickness is reduced as the coefficient of friction is increased, and, therefore, a lesser coefficient of friction results in uniform thickness.

Table 6 shows the effect of the coefficient of friction on the dome thickness, the average thickness, and the thinning factor obtained using the FEA model. From the results, it is observed that the dome thickness and thinning factor decrease significantly with increases in the friction coefficient while the average thickness shows only a negligible drop. Increasing the coefficient of friction creates localised thinning in the dome of the sheet and, therefore, results in large

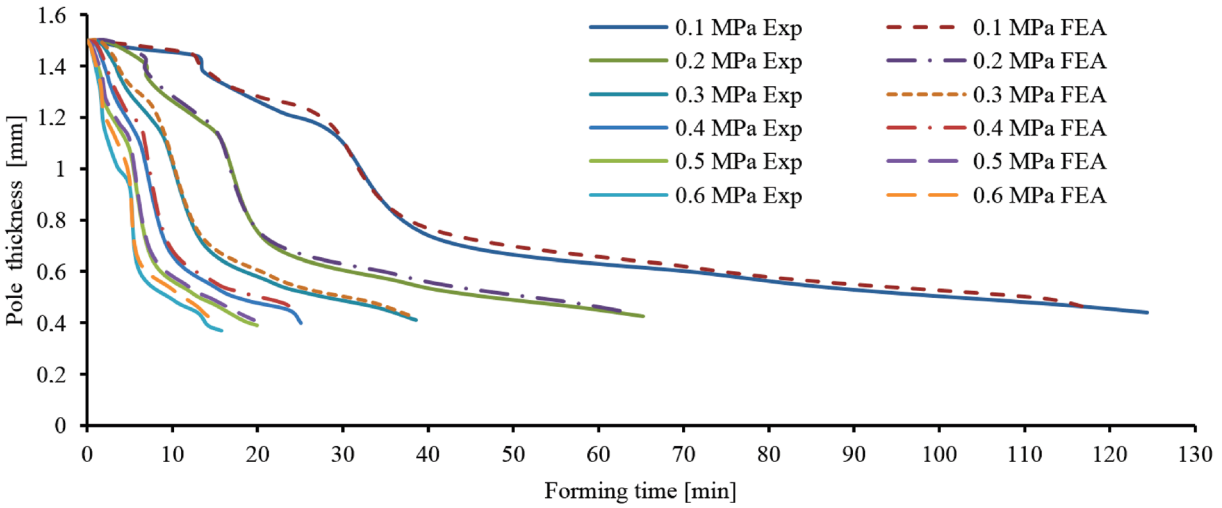

Fig. 7. *Pole thickness as a function of forming time at 450 °C*

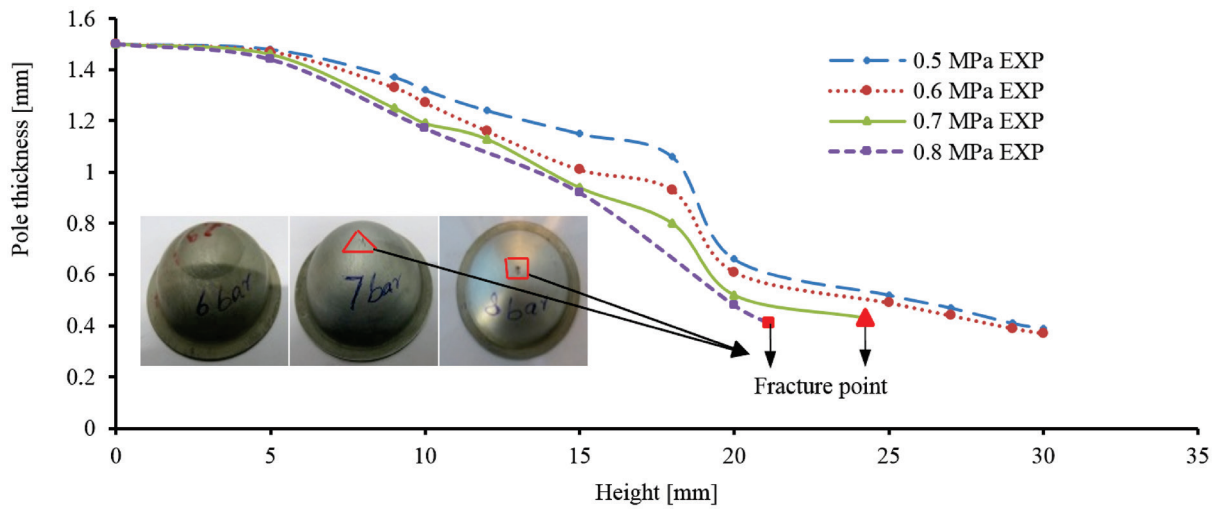

Fig. 8. *Pole thickness as a function of forming height at tearing point and 450 °C*

variations in the dome thickness. Thickness variations can be minimized achieved by ensuring lower friction coefficient. In addition, a higher coefficient of friction will also affect the forming time in a negative manner as shown in Table 7.

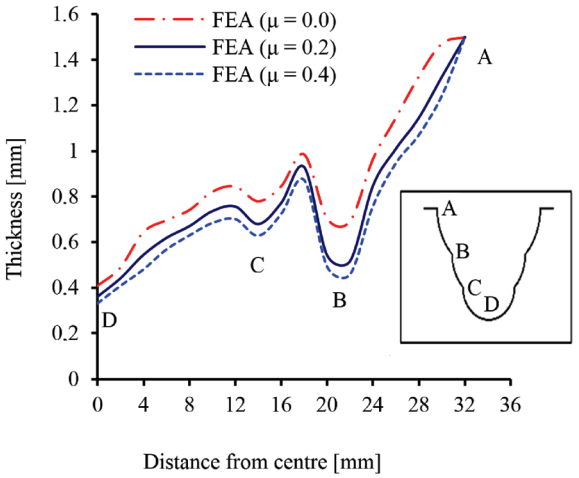

Fig. 9. *Thickness distribution from the centre as a function of friction coefficient*

Table 3. *Effect of pressure on forming characteristics at 450 °C from Experimental data*

Description	0.1 [MPa]	0.2 [MPa]	0.3 [MPa]	0.4 [MPa]	0.5 [MPa]	0.6 [MPa]
Dome thickness [mm]	0.44	0.43	0.41	0.40	0.39	0.37
Average thickness [mm]	0.99	0.98	0.92	0.90	0.87	0.83
Thinning factor [%]	44.63	44.67	44.69	44.71	44.73	44.71

Table 4. *Effect of pressure on forming characteristics at 450 °C in FEA*

Description	0.1 [MPa]	0.2 [MPa]	0.3 [MPa]	0.4 [MPa]	0.5 [MPa]	0.6 [MPa]
Dome thickness [mm]	0.45	0.44	0.43	0.42	0.41	0.39
Average thickness [mm]	0.99	0.97	0.94	0.92	0.89	0.85
Thinning factor [%]	45.62	45.65	45.68	45.70	45.72	45.71

Table 5. *Bulge height, forming time and thickness at fracture point*

Description	Pressure [MPa]	Forming height [mm]	Forming time [min]	Pole thickness [mm]
Fracture point	0.7	24.3	7.3	0.43
	0.8	21.2	6.3	0.44

Table 6. *Effect of friction coefficient on forming characteristics at 450 °C*

Description	FEA		
	$\mu = 0.0$	$\mu = 0.2$	$\mu = 0.4$
Dome thickness [mm]	0.41	0.36	0.33
Average thickness [mm]	0.92	0.91	0.9
Thinning factor [%]	44.53	39.61	36.64

Table 7. *Forming time at different friction coefficient*

Coefficient of friction (FEA)	Forming time [min]
$\mu = 0.0$	20
$\mu = 0.2$	22
$\mu = 0.4$	23

3.6 Effect of Die Entry Radius and Time on Pole Thickness

In the superplastic forming process, the die entry radius is bound to affect the SPF parameters, such as the thickness of the formed profile, the pole thickness and forming time. In order to maximise the uniformity of thickness in a three-stage dome profile, it is important to understand the effect of the die entry radius of a female die on the characteristics of the formed profile.

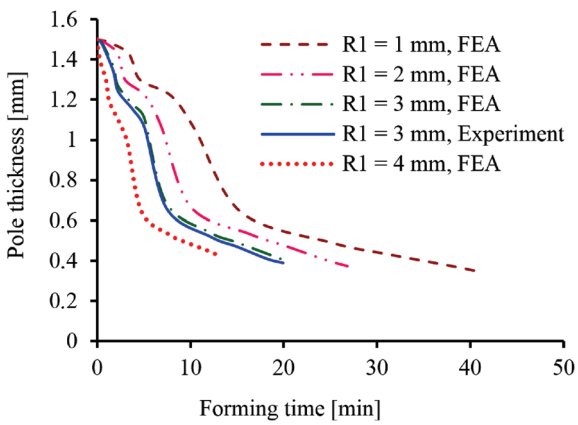

Fig. 10. *Pole thickness with a function of forming time at different die entry radii*

In the experimental and FEA studies, the assigned values for die entry radius are 3 mm, 2 mm and 1 mm for the first, second and third die entry points, respectively. In the FEA model, the first die entry values have been changed to 1 mm, 2 mm and 4 mm, while the second and third die entry radius values have been kept at 1mm for all these die entry radius values, the pole thickness is given as a function of forming time is in Fig. 10. It is evident from Fig.10 that the total forming time decreases with increases in

the die entry radius, and that the pole thickness has been found to increase with the increase in die entry radius. The thickness of the profiles, as obtained from the FEA studies, from the centre point of dome along the profile towards the edge of it is shown in Fig. 11.

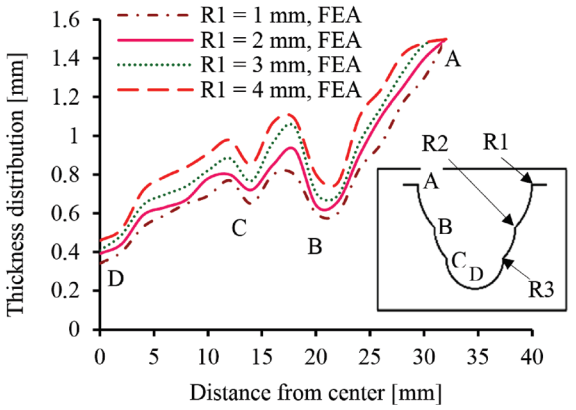

Fig. 11. *Thickness distribution with respect to distance from centre at different die entry radii*

Table 8. *Effect of die entry radius on forming characteristics at 450 °C*

Description	FEA (R2 = R3 = 1 mm)			
	R1 = 1 mm	R1 = 2 mm	R1 = 3 mm	R1= 4 mm
Dome thickness [mm]	0.34	0.37	0.41	0.45
Average thickness [mm]	0.78	0.84	0.92	0.97
Thinning factor [%]	42.3	43.9	44.5	46.9

Fig. 11 shows the simulated results obtained from FEA studies on the effect of die entry radius on the thickness distribution in the profile with reference to its centre. It is evident that the thickness is at its maximum at the edges of the profile and that it decreases as the reference points move close to the centre. However, the reduction in thickness of the profile as one move from the edge of the profile towards its centre is not gradual and continuous. At the second and third die entry regions of the female die, the thickness is first found to undergo a significant drop followed by a corresponding increase before it starts decreasing again gradually. These two discontinuity-like behaviours could be attributed to the localized thinning around the die entry regions. Table 8 shows the FEA results on the variation of dome thickness, average thickness and thinning factor as a function of die entry radius. From the results, it is observed that dome thickness and thinning factor increase with an increase in the die entry radius. The higher thinning factor, due to higher die entry radius, indicates more uniformity in thickness and, therefore, it canbe concluded that the die entry radius has a vital effect in controlling the thickness of the formed profile.

4 CONCLUSIONS

Experimental investigations and finite element analysis of the three-stage forming process have been carried out and analysed in terms of important forming characteristics. Three-stage superplastic forming of the 5083 aluminium alloy into a hemispherical die has been carried out at different forming pressures in order to predict the optimum forming pressure required to obtain uniform profile thickness. FEA has been used as a guide for performing the three-stage superplastic forming process and studied the thickness uniformity in the profile.

Discontinuities in the thickness of the formed profile have been observed due to the transition of radius from one stage to the next. Experimental studies have revealed that an optimum pressure of 0.5 MPa for achieving uniform thickness in the profile exists. Moving away from the optimum pressure leads either to variations in thickness or instabilities in the profile.

For the three-stage simulation under identical forming conditions, it has been shown that the uniformity in thickness of the profile is possible by taking the coefficient friction value below 0.1 and keeping the die entry radius greater than 4 mm. In the three-stage superplastic forming, the parameters obtained are in good correlation for both the experimental and FE simulation method.

5 REFERENCES

[1] Cebeli, Ö., Engin, Ü. (2011). Optimization and modeling of angular deep drawing process for square cups. *Journal of Materials and Manufacturing Process*, vol. 26, no. 9, p. 1117-1125, **DOI:10.1080/10426914.2010.532526**.

[2] Petek, A., Gantar, G., Pepelnjak, T., Kuzman, K. (2007). Economical and ecological aspects of single point incremental forming versus deep drawing technology. *Trans Tech Publications*, vol. 344, p. 931-938, DOI:**10.4028/www.scientific.net/KEM.344.93**.

[3] Wang, L.R., Zhao, Y.Q., Zhou, L. (2012). Effect of hot rolling on the structure of TC21 alloy with acicular alpha. *Journal of Materials and Manufacturing Process*, vol. 27, no. 2, p. 154-159, **DOI:10.1080/10426914.2011.566662**.

[4] Nițu, E., Iordache, M., Marincei, L., Charpentier, I., Le Coz, G., Ferron, G., Ungureanu, I. (2011). FE-modeling of cold rolling by in-feed method of circular grooves. *Strojniški vestnik - Journal of Mechanical Engineering*, vol. 57, no. 9, p. 667-673, **DOI:10.5545/sv-jme.2010.244**.

[5] Petek, A., Pepelnjak, T., Kuzman, K. (2005). New method for determination of fld in digital environment. *Strojniški vestnik - Journal of Mechanical Engineering*, vol. 51, no. 6, p. 330-345.

[6] Emmens, W.C., Sebastiani, G., Van den Boogaard, A.H. (2010). The technology of incremental sheet forming. *Journal of Materials Processing Technology*, vol. 210, no. 8, p. 981-997, **DOI:10.1016/j.jmatprotec.2010.02.014**.

[7] Burtchen, M., Hunkel, M., Lübben, T., Hoffmann, F., Zoch, H.W. (2009). Simulation of quenching treatments on bearing components. *Strojniški vestnik - Journal of Mechanical Engineering*, vol. 55, no. 3, p. 155-159.

[8] Jovane, F. (1968). An approximate analysis of the superplastic forming of a thin circular diaphragm. *Theory and experiments. International Journals of Mechanical Science*, vol. 10, no. 5, p. 403-427, **DOI:10.1016/0020-7403(68)90005-2**.

[9] Luckey, S.G.Jr., Friedman, P.A., Weinmann, K.J. (2009). Design and experimental validation of a two-stage superplastic forming die. *Journals of Materials Processing Technology*, vol. 209, no. 4, p. 2152-2160, **DOI:10.1016/j.jmatprotec.2008.05.019**.

[10] Ragab, A.R. (2002). Thermoforming of superplastic sheet in shaped dies. *Metal Materials Technology*, vol. 10, no. 1, p. 340-348, **DOI:10.1179/030716983803291262**.

[11] Aoura, Y., Ollivier, D., Ambari, A., Dal Santo, P. (2004). Determination of material parameters for 7475 Al alloy from bulge forming tests at constant stress. *Journal of Materials Processing Technology*, vol. 145, no. 3, p. 352-359, **DOI:10.1016/j.jmatprotec.2003.09.002**.

[12] Karthikeyan, L., Senthil Kumar, V.S., Padmanabhan, K.A. (2013). Investigations on superplastic forming of friction stir-processed AA6063-T6 aluminium alloy. *Journal of Materials and Manufacturing Process*, vol. 28, no. 3, p. 294-298, **DOI:10.1080/10426914.2012.667895**.

[13] Yogesha, B., Bhattacharya, S.S. (2011). Superplastic hemispherical bulge forming of a Ti-Al-Mn alloy. *International Journal of Scientific & Engineering Research*, vol. 2, no. 12, p. 1-4.

[14] SenthilKumar, V.S., Viswanathan, D., Natarajan, S. (2006). Theoretical prediction and FEM analysis of superplastic forming of AA7475 aluminum alloy in a hemispherical die. *Journal of Material Processing Technology*, vol. 173, no. 3, p. 247-251, **DOI:10.1016/j.jmatprotec.2005.04.112**.

[15] Pradeep, L., Menezes, K., Satish, V.K. (2010). Influence of die surface textures during metal forming—a study using experiments and simulation. *Journal of Materials and Manufacturing Process*, vol. 25, no. 9, p. 1030-1039, **DOI:10.1080/10426914.2010.499037**.

[16] Xiaomei, L., Steven, S. (2010). Numerical simulation of the superplastic forming of a dental ridge augmentation membrane. *Journal of Materials and Manufacturing Process*, vol. 25, no. 12, p. 1470-1476, **DOI:10.1080/10426914.2010.512653**.

[17] Luckey, S.G.Jr., Friedman, P.A., Weinmann, K.J. (2007). Correlation of finite element analysis to superplastic forming experiments. *Journals of Materials Processing Technology*, vol. 194, no. 1-3, p. 30-37, **DOI:10.1016/j.jmatprotec.2007.03.122**.

[18] Ng, J.C., Luckey,S.G., Kridli, G.T., Friedman, P.A. (2011). Validation of a modified material model for use with shell elements to improve the predictive accuracy of the thickness distribution in superplastic forming of sheet metals. *Journal of Materials Processing Technology*, vol. 211, no. 8, p. 1386-1394, **DOI:10.1016/j.jmatprotec.2011.03.012**.

[19] Jarrar, F.S., Louis, G.H.Jr., Marwan, K.K., Allan, F.B. (2010). New approach to gas pressure profile prediction for high temperature AA5083 sheet forming. *Journal of Material Processing Technology*, vol. 210, no. 6-7, p. 825-834, **DOI:10.1016/j.jmatprotec.2010.01.002.**

[20] Wu, H.-Y. (2000). Influence of deformation variables on cavitation of a superplastic 5083 Aluminium alloy. *Journal of Materials and Manufacturing Process*, vol. 15, no. 2, p. 231-245, **DOI:10.1080/10426910008912985**.

[21] Dezelak, M., Stepisnik, A., Pahole, I., Ficko, M. (2014). Evaluation of twist springback prediction after an AHSS forming process. *International Journal of Simulation Modelling*, vol. 13, no. 2, p. 171-182, **DOI:10.2507/IJSIMM13(2)4.261**.

[22] Hojjati, M.H., Zoorabadi, M., Hosseinipour, S.J. (2008). Optimization of superplastic hydro forming process of Aluminium alloy 5083. *Journal of Materials Processing Technology*, vol. 205, no. 1-3, p. 482-488, **DOI:10.1016/j.jmatprotec.2007.11.208**.

Strojniški vestnik - Journal of Mechanical Engineering 61(2015)6, 374-382

DOI:10.5545/sv-jme.2014.2224 Original Scientific Paper
Received for review: 2014-10-08
Received revised form: 2015-03-23
Accepted for publication: 2015-04-08

Design of Anti-Roll Bar Systems Based on Hierarchical Control

Balázs Varga[1] – Balázs Németh[2] – Péter Gáspár[1,2,*]

[1] Budapest University of Technology and Economics, Department of Control for Transportation and Vehicle Systems, Hungary
[2] Hungarian Academy of Sciences, Institute for Computer Science and Control, Systems and Control Laboratory, Hungary

This paper proposes the modelling and control design of active anti-roll bars. The aim is to design and generate active torque on the chassis in order to improve roll dynamics. The control system also satisfies the constraint of limited control current derived from electrical conditions. The dynamics of the electro-hydraulic anti-roll bar are formulated with fluid dynamical, electrical and mechanical equations. A linear model is derived for control-oriented purposes. Several different requirements and performances for the control influence the hierarchical handling of the control design. In the hierarchical architecture, a high level improves chassis roll dynamics via a gain-scheduling linear quadratic (LQ) control, while a low level guarantees the input limitation and produces the necessary actuator torque by a constrained LQ control. The operation of the designed anti-roll bar control system is illustrated through simulation examples.

Keywords: anti-roll bar, hydraulic actuator, gain-scheduling, LQ, automotive control application

Highlights

- *Electro-hydraulic actuator modelling of an anti-roll bar system.*
- *Constrained LQ control design for the actuator control.*
- *Development of a gain-scheduling strategy for the control of roll dynamics.*
- *Handling slow and fast roll dynamics performances together in the control.*

0 INTRODUCTION AND MOTIVATION

The improvement of roll dynamics is a relevant problem in vehicles with a high centre of gravity. Several roll-control systems that enhance the protection of cargo and improve roll stability have been developed. One of the most preferred roll-control solutions is anti-roll bars, which increase the stiffness of the suspension system. In this control system, torsion bars connect the left- and right-side suspensions on an axle. Active anti-roll bars can adapt to the current road conditions and lateral effects, while roll stability is improved.

Several papers propose methods to reduce the chassis roll motion of road vehicles. Three different active systems are applied: anti-roll bars, auxiliary steering angle and differential braking forces [1]. Active anti-roll bars commonly apply hydraulic actuators to achieve appropriate roll moment [2]. In [3], an active roll-control system based on a modified suspension system is developed with the distributed control architecture. Active steering uses an auxiliary steering angle to reduce the rollover risk of the vehicle. However, this method also influences the lateral motion of the vehicle significantly [4]. The advantages of the differential braking technique are its simple construction and low cost [5]. In this case, different braking forces are generated on the wheels to reduce the lateral force. Several papers deal with the integration of the systems mentioned above. In [6], the integration of the active anti-roll bar and active braking is presented, while [7] investigates the coordination of active control systems, which could be controlled to alter the vehicle rollover tendencies of the vehicle. The benefits of the integration of anti-roll bars and the lateral control are presented in [8]. Furthermore, the control design of anti-roll bars for the articulated vehicles is a significant and novel topic in [9]. An analysis of the snaking stability of a tractor-light trailer vehicle, in which the trailer contains anti-roll bars is presented in [10]. A special construction of semi-active anti-roll bars, which guarantees both ride and roll performances is shown in [11]. The ride and roll performances for an active anti-roll system using a PID control are analysed in [12].

The active system proposed in this paper integrates an electro-hydraulic actuator into an anti-roll bar. The system contains a high-level controller, which improves the roll dynamics of the chassis using active torque; thus, the roll motion of the chassis is influenced. The high-level control strategy is realized with a gain-scheduling Linear Quadratic (LQ) controller. The actuator of the anti-roll bar is an oscillating hydromotor with a servo valve on the low level. The actuator control guarantees the generation of the necessary active torque and satisfies the input constraint of the electric circuit. The control design is based on a constrained LQ method [13]. The goal of this paper is to demonstrate a multi-level control design of an anti-roll bar system.

The paper is organized as follows. Section 1 presents the control-oriented formulation of chassis

*Corr. Author's Address: Budapest University of Technology and Economics, H-1111, 2. Stoczek utca, Budapest, Hungary, gaspar.peter@mail.bme.hu

roll dynamics and the electro-hydraulic actuator using fluid dynamical, electrical and mechanical equations. Section 2 describes the architecture of the active anti-roll bar control system and details the design methods of the vehicle dynamics and actuator controllers with demonstration examples. The actuation of the control system is illustrated with a simulation example in Section 3. Finally, Section 4 summarizes the contributions of the paper.

1 CONTROL-ORIENTED SYSTEM MODELLING

In this section, the mechanical and hydraulic equations expressing the operation of the actuator are presented. The linear vehicle model, describing the roll dynamics of the chassis is modelled, which is enhanced with the active anti-roll bar system. The actuator for this system consists of a hydromotor and a valve. The four degrees-of-freedom vehicle dynamic model is illustrated in Fig. 1.

1.1 Modelling of Chassis Roll Dynamics

Concerning the rolling motion of the chassis (sprung mass), an anti-roll bar is required so as to reduce the effect of load transfer and roll angle.

The intervention of the anti-roll bar system is a force couple on the unsprung masses, which is provided by an active torque of the electro-hydraulic actuator M_{act}. Lateral force F_{lat} on the vehicle chassis and road excitations on the wheels g_{01}, g_{02} are disturbances active in the system. In the model, the masses, spring stiffness, damping ratios and geometrical parameters are constants. h is the distance between the roll centre of the chassis, and its centre of gravity and r is the half-track of the vehicle. The length of the anti-roll bar arm in the longitudinal direction is denoted by a_{arm}. In the model, the effects of the side-slip angle and under-/oversteering are ignored.

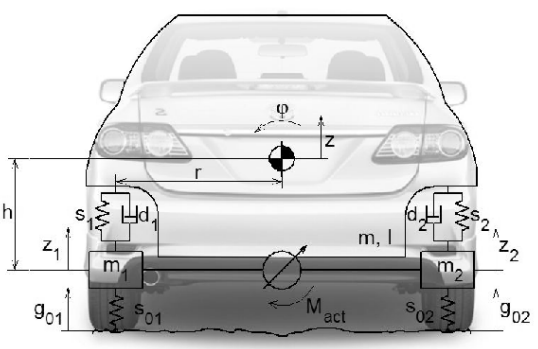

Fig. 1. *Illustration of the vehicle model*

The vehicle dynamics are derived from the Euler-Lagrange formalism in four second-order differential equations:

$$m\ddot{z} = -(d_1 + d_2)\dot{z} - (d_2 r - d_1 r)\dot{\varphi} + d_1\dot{z}_1 + d_2\dot{z}_2 - \\ -(s_1 + s_2)z - (s_2 r - s_1 r)\varphi + s_1 z_1 + s_2 z_2, \quad (1a)$$

$$I\ddot{\varphi} = -(d_2 - d_1)r\dot{z} - (d_1 + d_2)r^2\dot{\varphi} - d_1 r\dot{z}_1 + d_2 r\dot{z}_2 - \\ -(s_2 - s_1)rz - (s_1 + s_2)r^2\varphi, \quad (1b)$$

$$m_1\ddot{z}_1 = d_1\dot{z} - d_1 r\dot{\varphi} - d_1\dot{z}_1 + s_1 z + s_1 r\varphi - \\ -(s_1 + s_{01})z_1 + s_{01}g_{01} + \frac{M_{act}}{2a_{arm}}, \quad (1c)$$

$$m_2\ddot{z}_2 = d_2\dot{z} + d_2 r\dot{\varphi} - d_2\dot{z}_2 + s_2 z - s_2 r\varphi - \\ -(s_2 + s_{02})z_2 + s_{02}g_{02} - \frac{M_{act}}{2a_{arm}}. \quad (1d)$$

The vertical dynamics of the sprung mass m, and its roll dynamics are described in Eqs. (1a) and (1b). The vertical dynamics of the unsprung masses m_1, m_2 are expressed in Eqs. (1c) and (1d). The proposed dynamical equations, Eq. (1) are transformed into state-space form as:

$$\dot{x}_{veh} = Ax_{veh} + B_{1,veh}w_{veh} + B_{2,veh}u_{veh}, \quad (2)$$

where the state vector of the vehicle $x_{veh} = [z_1,\ z_2,\ z,\ \varphi,\ \dot{z}_1,\ \dot{z}_2,\ \dot{z},\ \dot{\varphi}]^T$ incorporates the vertical displacements of unsprung z_1, z_2 and sprung masses z, the chassis roll angle φ and their derivatives. The control input $u_{veh} = M_{act}$ of the system is the active torque generated by the electro-hydraulic actuator. The disturbances of the system $w_{veh} = [g_{01},\ g_{02},\ F_{lat}]^T$ are road excitations on the wheels and lateral forces.

1.2 Electro-Hydraulic Actuator Model of Anti-Roll Bar System

The active torque M_{act} is generated by the electro-hydraulic actuator. The actuator that realizes the torque is an oscillating hydromotor, see Fig. 2. An oscillating hydromotor is a rotary actuator with two cells, separated by vanes. The pressure difference between the vanes generates a torque on the central shaft, which has a limited rotation angle. The anti-roll bar is split in two halves, and the motor connects them. The shaft of the motor is connected to one side of the roll bar, and the housing is to the other. When the vehicle chassis rolls, a torque appears in the house,

which can be countered by the pressure difference in the two chambers provided by a pump.

The hydromotor is connected to a symmetric 4/2 four-way valve, and the spool displacement of this valve is realized by a permanent magnet flapper motor. Since the presented system has high energy density, it requires little space and has low mass. Furthermore, the actuator has a simple construction, but it requires an external high-pressure pump [14].

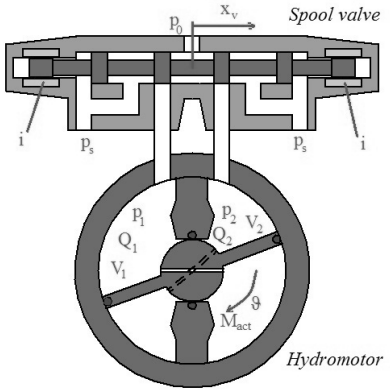

Fig. 2. *Electro-hydraulic actuator*

The physical input of the actuator is the valve current i, the output is the active torque M_{act}. The flapper motor and the spool can be modelled as a second order linear system, which creates a linear dependence between the valve current and the spool displacement. The motion of valve is modelled as:

$$\frac{1}{\omega_v^2}\ddot{x}_v + \frac{2D_v}{\omega_v}\dot{x}_v + x_v = k_v i, \tag{3}$$

where k_v valve gain equals $k_v = \frac{Q_N}{\sqrt{\Delta p_N / 2}}\frac{1}{u_{vmax}}$, where Q_N is the rated flow at rated pressure and maximum input current, p_N is the pressure drop at rated flow and u_{vmax} is the maximum rated current. D_v is the valve damping coefficient, which can be calculated from the apparent damping ratio. D_v stands for the natural frequency of the valve [15]. Note that the modelling of the valve motion poses several difficulties. Although Eq. (3) results in a suitable form for control-oriented purposes, the null positioning of the valve is a crucial problem.

The pressures in the chambers depend on the flows of the circuits Q_1, Q_2. p_L is the load pressure difference between the two chambers. The average flow of the system, assuming supply pressure p_s is constant:

$$Q_L(x_v, p_L) = C_d A(x_v)\sqrt{\frac{1}{\rho}\left(p_s - \frac{x_v}{|x_v|}p_L\right)}. \tag{4}$$

This equation can be linearized around $(x_{v,0}; p_{L,0})$ see [14]

$$Q_L = K_q x_v - K_c p_L, \tag{5}$$

where K_q is the valve flow gain coefficient and K_c is the valve pressure coefficient. In this modeling principle, the hydromotor model does not take into account the friction force and the external leakage flow. The compressibility of the fluid is considered constant [14].

The volumetric flow in the chambers is formed as:

$$\dot{p}_L = \frac{4\beta_E}{V_t}\left(Q_L - V_p\dot{\vartheta} + c_{l1}\dot{\vartheta} - c_{l2}p_L\right), \tag{6}$$

where β_E is the effective bulk modulus, V_t is the total volume under pressure and V_p is proportional to the areas of vane cross-sections. c_{l1} and c_{l2} are parameters of the leakage flow.

The motion equation of the shaft rotation due to the pressure difference $\dot{p}_L$ and the external load M_{ext} is:

$$J\ddot{\vartheta} = -d_a\dot{\vartheta} + V_p p_L + M_{ext}, \tag{7}$$

where J is the mass of the hydromotor shaft and vanes, and d_a is the damping constant of the system. M_{ext} is the effect of disturbances on the chassis roll dynamics. In the linear form, the nonlinearities of the friction are ignored.

The active torque of the actuator is determined by p_L. The relationship is written as follows:

$$M_{act} = 2p_L A_v a_{arm}, \tag{8}$$

where A_v is the area of the vanes, and is the arm of the stabilizer bar in the longitudinal direction.

The control design of the actuator requires the transformation of the previous equations into a state-space form. Eqs. (3), (6) and (7) are the necessary differential equations, Eq. (5) is a part of Eq. (6):

$$\dot{x}_{act} = A_{act}x_{act} + B_{1,act}w_{act} + B_{2,act}u_{act}, \tag{9a}$$

$$y_{act} = c_{act}x_{act}. \tag{9b}$$

The state vector of the actuator model $x_{act} = \begin{bmatrix} x_v & \dot{x}_v & p & \dot{\vartheta} \end{bmatrix}^T$ contains the spool displacement x_v and its derivative $\dot{x}_v$, the load pressure p and the shaft angular velocity $\dot{\vartheta}$. The output $y_{act} = M_{act} = u_{veh}$ of the system is formulated

using Eq. (8). The control input is $u_{act}=i$, while the disturbance is the external load $w_{act}=M_{ext}$.

Finally, the model of the anti-roll bar, incorporating vehicle dynamics (Eq. (2)) and actuator dynamics (Eq. (9)) is formulated as:

$$\dot{x} = Ax + B_1 w + B_2 u, \tag{10}$$

where $x=[x_{veh}, x_{act}]^T$, disturbance vector is $w=[w_{veh}, w_{act}]^T$, the input is $u=u_{act}$ and the matrices are:

$$A = \begin{bmatrix} A_{veh} & B_{2,veh}C_{act} \\ 0 & A_{act} \end{bmatrix},$$

$$B_1 = \begin{bmatrix} B_{1,veh} & 0 \\ 0 & B_{1,act} \end{bmatrix}, \qquad B_2 = \begin{bmatrix} 0 \\ B_{2,act} \end{bmatrix}.$$

2 HIERARCHICAL DESIGN OF ANTI-ROLL BAR CONTROL

2.1 Performances of the Control Problem

In the previous section, the roll dynamics and the electro-hydraulic actuator were modeled, and a control-oriented model for active anti-roll bar control design was built. This section proposes the architecture and the optimal design of the control system.

The anti-roll bar control system must fulfil several requirements. The role of the system is to enhance the roll dynamics of the vehicle, which has two main components: the roll angle φ and the roll angular acceleration $\ddot{\varphi}$. First, the roll angle of the chassis influences the traveling comfort of the vehicle, and the high roll angle increases the risk of the rollover motion. Second, it is essential to take into account the roll angular acceleration, due to the impulse-like excitations. These road excitations lead to the intense angular acceleration of the chassis, while the roll angle remains small. With the minimization of $\ddot{\varphi}$, the risk of rollover caused by sudden effects can be reduced. The vehicle dynamic performances are formulated such as:

$$z_1 = \varphi \quad |z_1| \rightarrow min, \tag{11a}$$

$$z_2 = \ddot{\varphi} \quad |z_2| \rightarrow min. \tag{11b}$$

The performances z_1, z_2 are arranged in a vector form, such as:

$$z = \begin{bmatrix} z_1 & z_2 \end{bmatrix}^T. \tag{12}$$

Another requirement for the control system is the minimization of the current i, for which there are two main reasons. First, there is the applied control energy, which is an economy requirement. Since the valve has a frequent intervention, the minimization of actuation energy is necessary. Second, the current has technical limits, such as $-i_{limit} \le i \le i_{limit}$. Thus, the control input $u=i$ must be minimized:

$$|u| \rightarrow min, \quad |u| \le i_{limit}. \tag{13}$$

Criteria in Eqs. (11) and (13) show that the anti-roll bar system must fulfil several requirements. In the following, a cost function J, which incorporates the previous requirements, is formulated. The goal of the control design is to find a controller which minimizes the cost function:

$$J = \frac{1}{2}\int_0^\infty \left[z^T Q z + u^T R u \right] dt \rightarrow min, \tag{14}$$

where Q and R are constant weights that influence the solution of the minimization problem. The role of the weights is to find a balance between the performances and the control input.

Although the design criterion (Eq. (14)) provides an adequate description of the control problem, it is difficult to find an appropriate solution. The overall formulation of the system (Eq. (10)) contains two subsystems (Eqs. (2) and (9)), whose dynamics are different: the dynamics of the chassis are slower than that of the hydraulic actuator. Moreover, the consideration of the input constraint in Eq. (13) also poses difficulties in high-order systems. It is beneficial to reduce the states of the system, which is guaranteed by the separation of the two subsystems. Furthermore, it is not necessary to constantly guarantee both of the performances (Eq. (11)). Using a changeable balance between the performances a less conservative controller can be achieved. However, it requires the reduction of the system order, which is guaranteed by the separation. In practice, dividing the optimization problem (Eq. (14)) into two sub-problems is recommended. This results in two optimal solutions to the sub-problems; however, they are suboptimal, considering the original problem.

In the following, the overall system (Eq. (10)) is divided into the vehicle (Eq. (2)), and actuator (Eq. (9)) subsystems. These are the high level and the low level in the hierarchy. The input of the high-level vehicle system is the actuator torque M_{act}, which is the output of the low-level actuator. The interconnection between the subsystems is created by M_{act}.

During the separation, the requirements for the controllers must be redefined. The high-level controller must fulfil the vehicle dynamic performances (Eq. (2)). The control input of the

high level in anti-roll bar is the active torque M_{act}. Due to economy and technical aspects, M_{act} must be minimized:

$$u_{veh} = M_{act}, \quad |u_{veh}| \rightarrow min. \tag{15}$$

Using the control input M_{act}, the roll dynamic performances (Eq. (2)) must be guaranteed. However, physically, it is the output of the actuator, see (Eq. (9)). The required control input is computed with the high-level controller and is denoted by $M_{act,ref}$. The purpose of the low-level control is to guarantee the minimum error between the required and the physical torque. Thus, the next performance is formed for the low-level control design:

$$z_{act} = M_{act,ref} - M_{act} \quad |z_{act}| \rightarrow min. \tag{16}$$

A further requirement for the control input of low-level i is defined in Eq. (13).

Based on the separation of vehicle dynamics and actuator, the optimization problem of the cost function J is divided into two parts:

$$\min_{K} J \leq \min_{K_{high}} J_{veh} + \min_{K_{low}} J_{act}, \tag{17}$$

where

$$J_{veh} = \frac{1}{2}\int_0^{\infty}\left[z^T Q_{veh} z + u_{veh}^T R_{veh} u_{veh}\right]dt, \tag{18a}$$

$$J_{act} = \frac{1}{2}\int_0^{\infty}\left[z_{act}^T Q_{act} z_{act} + u^T R_{act} u\right]dt, \tag{18b}$$

where K is the optimal controller of the problem (Eq. (14)), K_{high} is the vehicle dynamic controller and K_{low} is the actuator controller. Note that the solution of the minimizations in Eq. (17) results in a suboptimal solution to the original minimization problem (Eq. (14)). However, in this way, a solution to the constrained optimization problem can be found. The architecture of the hierarchical control is illustrated in Fig. 3.

2.2 Vehicle Level Control Design

In the following, the control design of the high level is presented. The roll dynamic performances of the system are the minimization of the roll angle and the roll angular acceleration, see Eq. (11). A further requirement for the control system is the minimization of the control input M_{act} in Eq. (15). Note that it is not necessary to simultaneously guarantee all of the requirements. There are priorities among them, which depend on the current vehicle dynamic status. The priority between the performances is represented with a scheduling variable ρ_{veh}, which is chosen as a linear combination of φ and $\ddot{\varphi}$:

$$\rho_{veh}(\varphi, \ddot{\varphi}) = a\varphi + b\ddot{\varphi}, \tag{19}$$

where a and b are design parameters, which represent the balance between φ and $\ddot{\varphi}$. ρ_{veh} is calculated during the measurements of the roll angle and angular acceleration signals. The scheduling variable is taken into consideration in the further design of the control architecture.

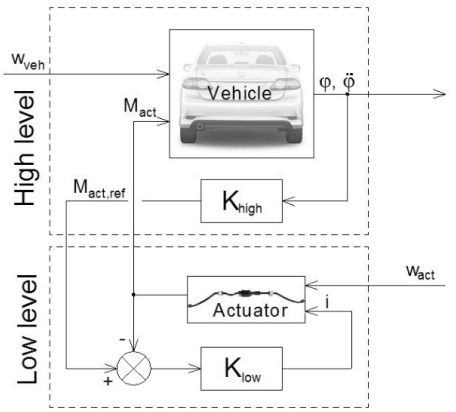

Fig. 3. *Architecture of control system*

Three criteria are defined in Section 2: the minimization of φ, $\ddot{\varphi}$ and M_{act}. Using ρ_{veh}, different weights are defined for these criteria:

$$\xi_i(\rho_{veh}) = e^{-\frac{(\rho_{veh}-m_i)^2}{\sigma_i}}, \quad |\xi_i(\rho_{veh})| \leq 1, \quad i = [1;2;3], \tag{20}$$

where m_i and σ_i are scale parameters of the curves belonging to the respective criteria. ξ_i weights depend on ρ_{veh}, and the functions have symmetric bell curve shapes, see Fig. 4. This is adequately chosen to express the importance of each criterion at a given ρ_{veh}. Where $\xi_i(\rho_{veh})$ has a high value, the consideration of the related criterion has a high priority.

Based on the J_{veh} cost function minimization problem, three different LQ controllers $K_{high,i}$ $i=[1;2;3]$ are designed. The resulting $K_{high,i}$ are LQ controllers computed with different Q_{veh}, R_{veh} weights.

- $K_{high,1}$ operates at low roll angles and low angular accelerations. In the absence of a critical situation, the actuator intervention is not necessary. As it saves energy, it is an economical mode of the anti-roll bar system. The weights of the LQ control design are $Q_{veh}=R_{veh}$.
- $K_{high,2}$ controller is activated when φ and $\ddot{\varphi}$ increase. It is essential to take into account both conditions, e.g. at impulse-like excitations

angular acceleration of the chassis increases, while the roll angle is still small. With this approach, the risk of a rollover caused by sudden effects can be reduced. The weights of the LQ control design are , $Q_{veh}>R_{veh}$ which guarantees the appropriate actuation.

- $K_{high,3}$ has an important role in the limitation of M_{act}, see Eq. (16). This controller prevents the actuator from being overload. The weights of the LQ control design are $Q_{veh}<R_{veh}$, which guarantees reduced actuation. If a common Lyapunov function P_{high} of the controllers $K_{high,i}$, then the global stability of the closed-loop systems is guaranteed [16].

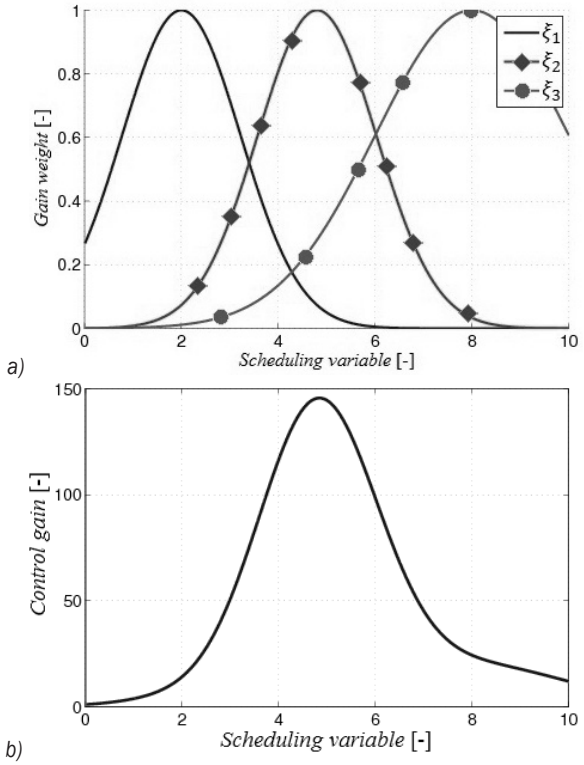

Fig. 4. *Scheduling variable dependence in high-level control; a) $\xi_i(\rho_{veh})$ functions and b) example on a K_{high} element*

The control strategy of the high-level control is based on the designed $K_{high,i}$ controllers and the scheduling variable-dependent $\xi_i(\rho_{veh})$ weights. In this way, a gain-scheduling LQ controller is formed:

$$K_{high}=\frac{\xi_1(\rho_{veh})K_1+\xi_2(\rho_{veh})K_2+\xi_3(\rho_{veh})K_3}{\xi_1(\rho_{veh})+\xi_2(\rho_{veh})+\xi_3(\rho_{veh})}, \quad (21)$$

where K_{high} is the convex combination of $K_{high,i}$. The convexity is guaranteed by the existence of P_{high} and the condition $|\xi_i(\rho_{veh})|\leq 1$. Thus, K_{high} is inside of the convex hull of $K_{high,i}$. Fig. 4 illustrates an example in which an element of K_{high} based on Eq. (21) is computed.

2.3 Actuator Level Control Design

The torque-tracking low-level actuator design is proposed below. The controller K_{act} is designed based on the minimization of J_{act}, using the constrained LQ control method. The purpose of the controller is to guarantee the required active torque of the high-level dynamic controller and satisfy the input constraint of the low level, see Eqs (16) and (13).

The low-level LQ controller is based on a piecewise linear control strategy. This method can be used for the approximation of nonlinear systems using linear sections. Piecewise linear systems are special types of switched linear systems with state-space partition-based switching. The main difficulty in this strategy is the switching between the controllers, which can cause transients in the control system [17].

The tracking criterion in Eq. (16) of the control system requires the reformulation of the state-space equation described in Eq. (9). The plant in Eq. (9) is augmented with an integrator on signal M_{act} to achieve zero steady-state error. The augmented system is as follows:

$$\begin{bmatrix}\dot{x}_{act}\\ \dot{z}_{act}\end{bmatrix}=\begin{bmatrix}A_{act} & 0\\ -c_{act} & 0\end{bmatrix}\begin{bmatrix}x_{act}\\ z_{act}\end{bmatrix}+\begin{bmatrix}B_{1,act}\\ 0\end{bmatrix}w_{act}+$$
$$+\begin{bmatrix}B_{2,act}\\ 0\end{bmatrix}u+\begin{bmatrix}0\\ 1\end{bmatrix}M_{act,ref}=$$
$$=\tilde{A}_{act}\tilde{x}_{act}+\tilde{B}_{1,act}w_{act}+\tilde{B}_{2,act}u+\begin{bmatrix}0\\ 1\end{bmatrix}M_{act,ref}. \quad (22)$$

The LQ controller design is based on the minimization of the following cost function (Eq. (17)), which incorporates the previous conditions of Eqs. (16) and (13) and the augmented plant in Eq. (22). The weights Q_{act} and R_{act} have an important role in satisfying input constraints. The minimization $\min_{K_{low}} J_{act}$ problem leads to a continuous-time control algebraic Riccati equation:

$$P_{low}\tilde{A}_{act}+\tilde{A}_{act}^{T}P_{low}-P_{low}\tilde{B}_{2,act}R_{act}^{-1}\tilde{B}_{2,act}^{T}P_{low}+Q_{act}=0, \quad (23)$$

where P_{low} is the solution to Riccati equation, $\tilde{A}_{act}$ and $\tilde{B}_{2,act}$ are the block matrices of Eq. (22). The optimal state feedback LQ controller K_{low} is derived from P_{low}.

Since the electric circuit of the actuator has physical limits, it is necessary to prevent the valve current from exceeding the limit u_{const}. In the conventional formulation of the LQ problem (Eq. (17)), it can be ensured by a high R_{act} weight.

It results in a conservative controller K_{low} with small gain, which leads to a reduced control input and the simultaneous degradation of z_{act} tracking performance. Moreover, a large LQ gain enhances the tracking performance, but it is likely to violate the input constraint u_{const}. A way to guarantee (Eq. (16)) and input constraint satisfaction is presented in [13]. In this paper, an iterative LQ control design method is proposed, which yields a switching LQ controller. In the method, numerous controllers are designed using different R_{act} weights. The iterative function for control design is as follows:

$$R_{act,i} = \frac{\sqrt{\rho_{act,i}}}{u_{const}} \sqrt{\left(\tilde{B}_{2,act}^{T} P_{low,i-1} \tilde{B}_{2,act}\right)}. \quad (24)$$

In this method, the different $R_{act,i}$ weights are used at fixed Q matrices, $\rho_{act,i}$ is the actual gain scaling parameter and u_{const} is the input constraint. $P_{low,i-1}$ is the solution of the $(i-1)^{\text{th}}$ Ricatti equation (Eq. (23)).

The solution to i^{th} Riccati equation is $P_{low,i}$, from which the i^{th} optimal LQ control can be computed. Furthermore, $P_{low,i}$ determines an ellipsoidal invariant set ε_i in the state-space, where the input constraint can be satisfied. As a result of the iterative design, numerous LQ gains and invariant sets are computed. The controller with the largest LQ gain belongs to the smallest ellipsoid. Based on the invariant sets, a switching strategy is defined to guarantee the input constraint. In the strategy, the trajectory of $\tilde{x}_{act}$ is monitored. When the trajectory reaches the set border of an ellipsoid and moves outwards, the system switches to a more conservative controller with a smaller LQ gain. The switching function is formulated as follows:

$$sign(\rho_{(act,i)} - \tilde{x}_{act}^{T} P_{(low,i)} \tilde{x}_{act}) < 1. \quad (25)$$

If Eq. (25) is not satisfied, then $\tilde{x}_{act}$ is out of the i^{th} ellipsoid; thus, it is necessary to switch to the $(i-1)^{\text{th}}$ controller.

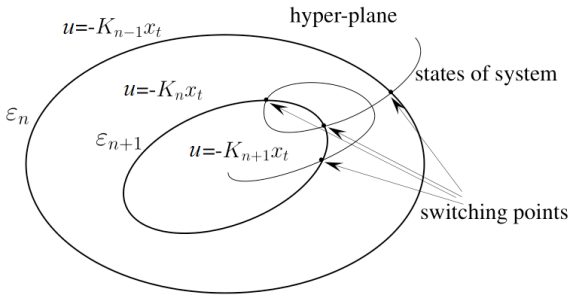

Fig. 5. *Invariant sets and switching of a two-state system*

The solution of the switching algorithm is always the smallest ellipsoid, which contains $\tilde{x}_{act}$. In this method, it is necessary to guarantee that $\tilde{x}_{act}$ never departs the largest ellipsoid ε_i. Therefore, $\rho_{act,i}$ must be chosen sufficiently high so as to not violate this condition. Since the system states are always in the outermost invariant set, the stability of the system is guaranteed. The switching algorithm described above is illustrated in Fig. 5.

3 SIMULATION EXAMPLE

In this section, the operation of the active anti-roll bar control is presented during a simulation example. The data of the full vehicle are presented in Table 1.

Table 1. *Data of vehicle and actuator models*

m	1300 kg	d_1	4500 Ns/m	d_2	4500 Ns/m
I	500 kgm^2	s_1	50000 N/m	s_2	50000 N/m
r	0.8 m	h	0.7 m	s_{01}	80000 N/m
a_{arm}	0.3 m	ω_v	7301 1/s	s_{02}	80000 N/m
k_v	0.523 1/A	K_q	11.02 m^2	K_c	10^{-12} N/m
β_e	6.9×10^8 Pa	V_t	1.95×10^{-4} m^3	V_p	1.95×10^{-4} m^3
c_{l1}	7.85×10^{-15} m^{3}s	c_{l2}	3.14×10^{-6} m^3/Pa	J	5 kgm^2
d_a	1000 Ns/m	A_v	0.0026 m^3	D_v	0.071
m_1	120 kg	m_2	120 kg		

The vehicle contains one anti-roll bar on the rear axle, which actuates to improve the roll dynamics of the vehicle.

The high-level gain-scheduling LQ control computes the currently required torque $M_{act,ref}$. The parameters in the scheduling function $\rho_{veh}(\varphi,\ddot{\varphi})$ are chosen as $a=1.92$ and $b=0.528$. In the low-level constrained LQ control $n=7$ controllers are designed. In the example, $n=1$, and LQ control has the highest gain, which improves the tracking performance, while $n=7$ is the most conservative, which satisfies the constraint $i_{limit}=0.3$ A. Scheduling variable and the number of the low-level controls are chosen based on the previously defined control strategy during the simulations.

The simulation example is illustrated in Figs. 6 and 7. The driver performs an abrupt cornering manoeuvre with 0.2 g maximum lateral acceleration, see Fig. 6. It results in the increase of φ and $\ddot{\varphi}$, as shown in Figs. 7a and b. In the figure, two scenarios are compared: a vehicle with an anti-roll bar and an uncontrolled case. The improvement of roll dynamics can be seen during the reduction of φ and $\ddot{\varphi}$ signals. The anti-roll bar is able to reduce the peak of the roll and angular acceleration signals, see e.g. at 42 s. Thus,

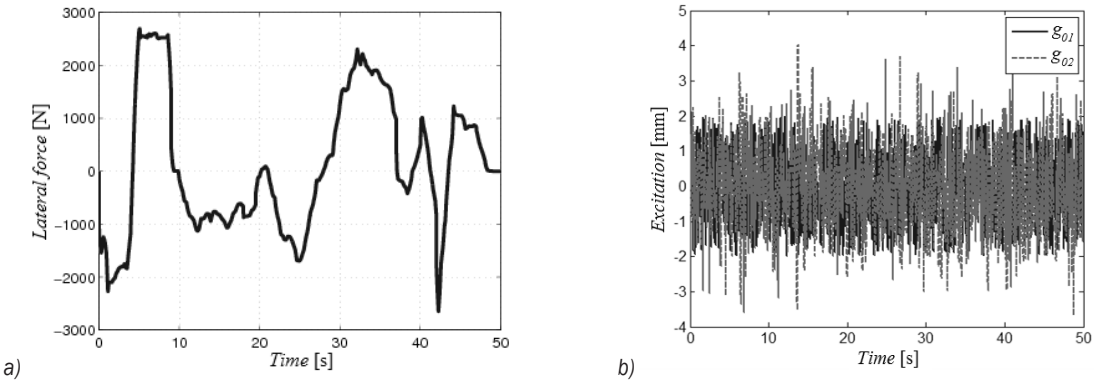

Fig. 6. *Disturbances on the vehicle; a)* F_{lat} *disturbance on chassis, and b) road excitations*

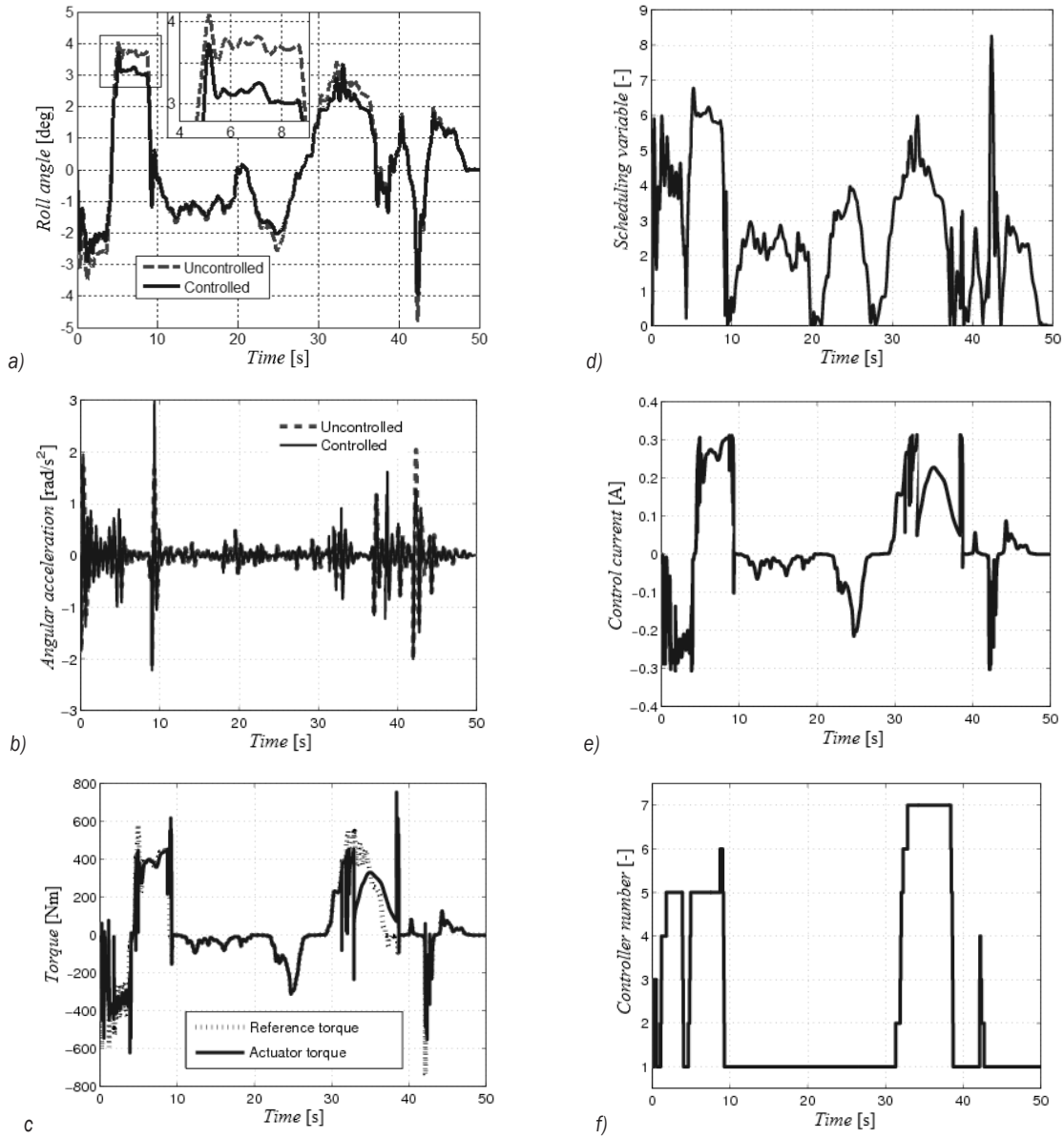

Fig. 7. *Simulation results of the control system; a) roll angle* φ*, b) Roll acceleration* $\ddot{\varphi}$ *, c) reference tracking* $M_{act,ref}$*, d) scheduling variable* ρ_{veh}*, e) low level control input* i*, and f) low level control switching sequence*

the performances of the entire system Eq. (11) are guaranteed.

The required torque $M_{act,ref}$ for the roll dynamics improvement by the high level control is illustrated in Fig. 7c. The changes in ρ_{veh} (Fig. 7d) guarantee the balance between φ, $\ddot{\varphi}$ and $M_{act,ref}$. For example, at 20 s the disturbance F_{lat} is around zero, and actuation is unnecessary. Therefore, ρ_{veh} has a low value. At a high F_{lat} (e.g. 5 s to 10 s), the signal ρ_{veh} is increased to avoid extremely high $M_{act,ref}$. The operation of the low level control is evaluated based on the torque-tracking performance Eq. (15), which is guaranteed with an appropriate threshold in most of the simulation. Moreover, the control system satisfies the input constraint i_{limit}, see Fig. 7e. During the actuation of the current, the low level switches to the appropriate LQ control, as shown in Fig. 7f. For example, between 31 s and 39 s the current i reaches i_{limit}, thus the controller switches to $n=7$ to avoid limit violation. However, it results in the degradation of torque tracking, see 7c.

4 CONCLUSIONS

The paper has proposed the design of anti-roll bars based on a hierarchical control architecture. The design is based on the modelling of the chassis and the electro-hydraulic actuator, in which the performance specifications and the uncertainties are formed. In the high level, the gain-scheduling LQ control is applied to design actuator torque, and the chassis roll dynamics are improved. In the low level, a constrained LQ control is applied to generate actuator torque, while the input limitation is taken into consideration. Within the hierarchical structure, the interaction between the two levels is handled. The simulation example shows that the control system improves roll dynamics and handles the input constraint simultaneously.

5 ACKNOWLEDGMENT

This paper was supported by the János Bolyai Research Scholarship of the Hungarian Academy of Sciences.

6 REFERENCES

[1] Shibahata, Y. (2005). Progress and future direction of chassis control technology. *Annual Reviews in Control*, vol. 29, no. 1, p. 151-158, **DOI:10.1016/j.arcontrol.2004.12.004**.

[2] Sampson, D., Cebon, D. (2003). Active roll control of single unit heavy road vehicles. *Vehicle System Dynamics*, vol. 40, no. 4, p. 229-270, **DOI:10.1076/vesd.40.2.229.16540**.

[3] Sampson, D., McKevitt, G., Cebon, D. (1999). The development of an active roll control system for heavy vehicles. *Proceedings of 16th IAVSD Symposium on the Dynamics of Vehicles on Roads and Tracks*, p. 704-715.

[4] Odenthal, D., Bunte, T., Ackermann, J. (1999). Nonlinear steering and braking control for vehicle rollover avoidance, *Proceedings of European Control Conference*.

[5] Palkovics, L., Semsey, A., Gerum, E. (1999). Rollover prevention system for commercial vehicles - additional sensorless function of the electronic brake system. *Vehicle System Dynamics*, vol. 32, no. 4-5, p. 285-297, **DOI:10.1076/vesd.32.4.285.2074**.

[6] Gáspár, P., Szaszi, I., Bokor, J. (2004). The design of a combined control structure to prevent the rollover of heavy vehicles. *European Journal of Control*, vol. 10, no. 2, p. 148-162, **DOI:10.3166/ejc.10.148-162**.

[7] Allan, Y.L. (2002). Coordinated control of steering and anti-roll bars to alter vehicle rollover tendencies. *Journal of Dynamic Systems, Measurement, and Control*, vol. 124, no. 1, p. 127-132, **DOI:10.1115/1.1434982**.

[8] Yim, S., Jeon, K., Yi, K. (2012). An investigation into vehicle rollover prevention by coordinated control of active anti-roll bar and electronic stability program. *International Journal of Control, Automation, and Systems*, vol. 10, no. 2, p. 275-287, **DOI:10.1007/s12555-012-0208-9**.

[9] Huang, H-H., Yedavalli, R.K. (2010). Active roll control for rollover prevention of heavy articulated vehicles with multiple-rollover-index minimization. *ASME Dynamic Systems and Control Conference*, **DOI:10.1115/DSCC2010-4278**.

[10] Šušteršič, G., Prebil, I., Ambrož, M. (2014). The snaking stability of passenger cars with light cargo trailers. *Strojniški vestnik - Journal of Mechanical Engineering*, vol. 60, no. 9, p. 539-548, **DOI:10.5545/sv-jme.2014.1690**.

[11] Stone, E.J., Cebon, D. (2008). An experimental semi-active anti-roll system. *Proceedings of Institution of Mechanical Engineers, Part D: Journal of Automobile Engineering*, vol. 222, no. 12, p. 2415-2433, **DOI:10.1243/09544070JAUT0650**.

[12] Zulkarnain, N., Imaduddin, F., Zamzuri, H., Mazlan, S.A. (2012). Application of an active anti-roll bar system for enhancing vehicle ride and handling. *IEEE Colloquium on Humanities, Science & Engineering Research*, **DOI:10.1109/chuser.2012.6504321**.

[13] Wredenhangen, G., Bélanger, P. (1994). Piecewise-linear LQ control for systems with input constraints. *Automatica*, vol. 30, no. 3, p. 403-416, **DOI:10.1016/0005-1098(94)90118-X**.

[14] Meritt, H.E. (1967). *Hydraulic Control Systems*. John Wiley & Sons Inc., Hoboken.

[15] Šulc, B., Jan, J.A. (2002). Non linear modelling and control of hydraulic actuators. *Acta Polytechnica*, vol. 42, no. 3, p. 173-182.

[16] Boyd, S., Ghaoui, L.E., Feron, E., Balakrishnan, V. (1997). *Linear Matrix Inequalities in System and Control Theory*. Society for Industrial and Applied Mathematics, Philadelphia.

[17] Zhendong, S. (2010). Stability of piecewise linear systems revisited. *Annual Reviews in Control*, vol. 34, no. 2, p. 221-231, **DOI:10.1016/j.arcontrol.2010.08.003**.

Strojniški vestnik - Journal of Mechanical Engineering 61(2015)6, 383-391
DOI:10.5545/sv-jme.2015.2404
Original Scientific Paper
Received for review: 2015-01-03
Received revised form: 2015-03-30
Accepted for publication: 2015-04-22

Proposal for an Experimental-Numerical Method for Friction Description in Sheet Metal Forming

Tomasz Trzepieciński[1] – Hirpa G. Lemu[2,*]

[1] Rzeszow University of Technology, Department of Materials Forming and Processing, Poland
[2] University of Stavanger, Department of Mechanical and Structural Engineering and Materials Technology, Norway

During the forming of draw pieces with complex shapes, such as car bodies, it is necessary to use dies with varying outline curvatures and varying radii of edge fillets. In such conditions, using the cylindrical counter-samples for friction modelling on the die fillet surface does not fully reflect the friction conditions on the edge of the die. In this article, a proposal for an experimental numerical method of friction determination on the rounded profiles of punch edges is presented. The method involves a bending under tension (BUT) test that is devised to simulate the frictional conditions over the punch radii. Numerical simulations of BUT tests were conducted with ABAQUS software. An elastic-plastic approach with Hill's (1948) anisotropic material formulation and isotropic strain hardening were considered. Results of both experimental and numerical approaches confirmed the usefulness of the proposed method.

Keywords: bending-under-tension, BUT test, finite element method, friction, friction coefficient

Highlights

- *An experimental-numerical method of friction determination on the rounded profiles of forming punch edges is proposed*
- *A bending under tension test is devised to simulate the frictional conditions over the punch radii.*
- *The numerical simulations of bending under tension tests are conducted with ABAQUS software.*
- *The surface topographies of DDQ steel sheet at different strain states and lubrication conditions are studied.*

0 INTRODUCTION

Frictional resistance in sheet metal forming depends on physical and chemical factors, among others, acting on the contact surface, the roughness and topography of sheet and tools, the dynamics of the loads, lubrication conditions, and the temperature [1] and [2]. Many kinds of friction tests have been developed to determine the coefficient of friction in sheet metal forming. Among the available methods, the most frequently used are the strip-drawing test, the draw bead simulator friction test and bending the under tension test.

The bending under tension (BUT) test is a group of tests in which a work piece is stretched and bent during the experiment so that the friction coefficient is measured under conditions similar to those encountered in the real forming process. The traditional way of performing BUT tests is with differential measurements in which two tests are carried out after each other, one by drawing the work piece over a fixed circular cylindrical tool-pin, the other over a freely rotating pin, with the understanding that no sliding takes place. The difference in front tension measured in two tests gives an estimate of the friction. One drawback of this method is the stochastic variations, which may cause large scatter, and the fact that steady-state conditions must be present while measuring.

Many BUT tests have contributed to the knowledge about sheet-forming tribology [3] and [4]. A new methodology to determine the friction coefficient via a BUT test, considering the pressure non-uniformity, has been suggested by Kim et al. [5]. Miguel et al. [6] used a BUT test to evaluate pressure in the die radius and the corresponding lubricated regime under multi-axial stress conditions.

Deng and Lovell [7] and Lovell and Deng [8] studied the influence of stamping process parameters and wear mechanisms on the characterization of interfacial friction in coated steel sheets. In these studies, it was determined that the lubricant properties had little influence on the final surface roughness of the deformed sheet. Considering the influence of the pin size, the results showed that the friction coefficient increased with decreasing pin radius values.

Intending to improve the chance of success before production trials of more environmentally benign tribo-systems, many researchers [9] and [10] described the equipment for realization of BUT tests and developed a methodology for off-line evaluation of tribo-systems for sheet metal forming. Furthermore, the BUT investigations conducted on the friction of galvannealed interstitial free sheet steels by Garza and Van Tyne [11] shown that the coefficient of friction also increases as the amount of iron content in the coating decreased. Alingner and Van Tyne [12] examined the change in the die profile of five

*Corr. Author's Address: University of Stavanger, 4036 Stavanger, Norway; Hirpa.g.lemu@uis.no

coated die materials tested in conjunction with three automotive steel sheets. The zirconia die material exhibited the least amount, but the most significant change.

Based on the experimental results of the BUT test, Wiklund et al. [13] developed a theoretical model to predict that the effective hardness of a surface is reduced by the presence of underlying plastic flow. The results of investigations of Pereira et al. [14] provide a qualitative description of the evolution and distribution of contact pressure at the die radius for a typical channel-forming process. The proposed contact pressure behaviour for the BUT test was compared to other results available in the literature. Both experimental and numerical approaches to the BUT test carried out by the authors [15] showed that, although the sheet was drawn over a cylindrical pin, the plane strain state assumed over the entire width of the sample is affected by the behaviour of the sample during bending. The stretch-drawing type tests (i.e. BUT) are widely used to investigate the influence of several material and technological parameters [16] and [17].

In this article, we propose an experimental-numerical method of friction determination on a punch edge with a rounded profile as a modification of the classic BUT test method.

1 DESCRIPTION OF BUT TEST METHOD

The BUT test is performed in two steps. First, a strip is drawn over a freely turning roller (Fig. 1), and the values of both pulling F_1 and back tension F_2 forces are determined. The difference between F_{1t} and F_{2t} forces is the force F_b due to bending and unbending of the sample over the roller. A second strip is then drawn over a fixed roller, and the corresponding pulling F_1 and back tension forces F_2, are determined.

Assuming that there is a constant friction coefficient μ in the contact region and that the wrap angle γ (Fig. 1) is constant during the test according to the equilibrium of all forces acting on an elemental cut of the strip $d\gamma$, it can be shown that:

$$F + q\mu wRd\gamma - (F + dF) = 0, \tag{1}$$

$$qwRd\gamma - F\sin\frac{d\gamma}{2} - (F + dF)\sin\frac{d\gamma}{2} = 0, \tag{2}$$

where q is the unit normal contact pressure and w is the width of the strip.

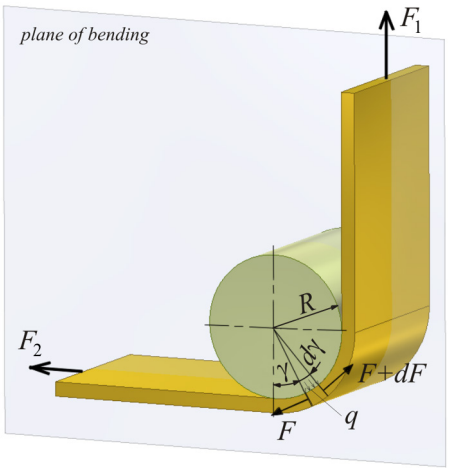

Fig. 1. *Forces acting on an elemental cut of the strip*

For a very small $d\gamma$ one can assume that $\sin\frac{d\gamma}{2} \approx \frac{d\gamma}{2}$ and $dF << F$. Thus, combining Eq. (1) and Eq. (2) gives:

$$\mu d\gamma = \frac{dF}{F}. \tag{3}$$

Integrating Eq. (3) and taking into account $\gamma = \pi/2$, the coefficient of friction is determined to be:

$$\mu = \frac{2}{\pi}\ln\left(\frac{F_1}{F_2}\right). \tag{4}$$

Formulas given by several authors take into consideration roller radius R and sheet thickness g. For a 90° bend angle, the friction coefficient μ can be determined from the formulae:

$$\mu = \frac{2}{\pi}\left(\frac{R + g/2}{R}\right)\ln\left(\frac{F_1 - F_b}{F_2}\right), \tag{5}$$

2 MOTIVATIONS

Separation of frictional resistance and bending resistance in the BUT test is only possible by using a cylindrical counter-sample. The use of non-cylindrical counter-samples does not allow carrying out the test in terms of rotational counter-sample.

Assuming the plane strain state of the sample in the theoretical analysis of friction tests is, therefore, a simplification. During the forming of draw pieces with complex shapes, such as car bodies, there are dies with varying outline curvatures (R) and varying radii of edge fillets (r) (Fig. 2).

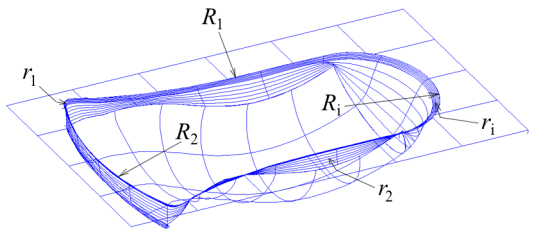

Fig. 2. *Example of a die shape for sheet forming with varying outline curvature (R_i) and varying radii of edge fillet of die (r_i)*

In such conditions, using a cylindrical counter-sample for friction modelling on the die fillet surface does not fully reflect the friction conditions on the edge of the die, which outline changes along the perimeter of the die hole. During the standard BUT test, the flat sample is bent in the plane perpendicular to the axis of the counter-sample (Fig. 1). Analysing the simplest case of forming of the axisymmetric draw-piece, it is seen that tri-axial stress occurs state on the die edge with additional peripheral compressive stresses (Fig. 3). The tri-axial state of stress in the contact area of the sheet with the non-cylindrical counter-sample makes the nature of the changes in the surface topography of the sheet closer to reality than when using a cylindrical counter-sample. The stress state at the rounded edges of the tools, depending on the geometry of these edges, has a significant effect on the nature of the plastic deformation of sheet over the rounded die and the change of its topography.

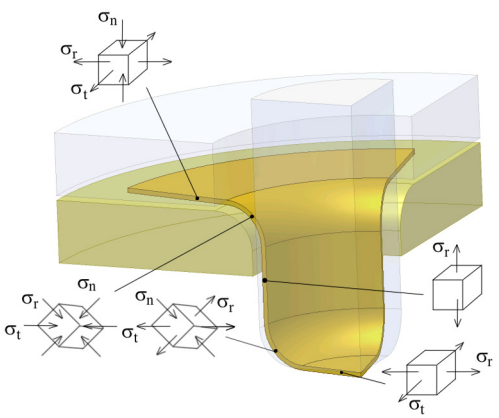

Fig. 3. *Stress state during forming of axi-symmetrical draw piece; σ_r, σ_t, σ_n - stresses: radial, tangential and normal, respectively*

3 METHOD OF FRICTIONAL RESISTANCE DETERMINATION

A major issue is the development of a realistic test that allows the separation of the frictional resistance and the bending resistance of the sample on rounded profiles of the die and the punch. The proposed method provides the ability to determine the coefficient of friction at the rounded edge of the tools. The formula for determining the friction coefficient is in accordance with the method for cylindrical counter-samples. The shape of the proposed counter-samples makes it necessary to use a different method for determining the test forces in the condition of friction elimination via the following steps:

- experimental determination of pulling and back tension forces during the friction test using the counter-sample with the non-cylindrical profile,
- numerical determination of the pulling and back tension forces under frictionless conditions ($\mu = 0$) using the counter-sample with the non-cylindrical profile.

The proposed method and counter-sample shapes for friction coefficient evaluation in the BUT test are not covered in the literature. Assuming that, during the friction test, the sample is bent at an angle of 90°, the coefficient of the friction is determined by modification of Eq. (5) as:

$$\mu = \frac{2}{\pi}\left(\frac{R + g/2}{R}\right)\ln\left(\frac{F_{1\exp} - \left(F_{1num} - F_{2num}\right)}{F_{2\exp}}\right), \quad (6)$$

where R is the radius of countersample rounding, g the sheet thickness, F_{1exp} the experimentally determined pulling force, F_{1num} the numerically determined pulling force, F_{2exp} the experimentally determined back tension force, F_{2num} the numerically determined back tension force.

During the experiment, the sheet metal is drawn on the stationary counter-sample with the convex (Fig. 4a) or the concave (Fig. 4b) profile.

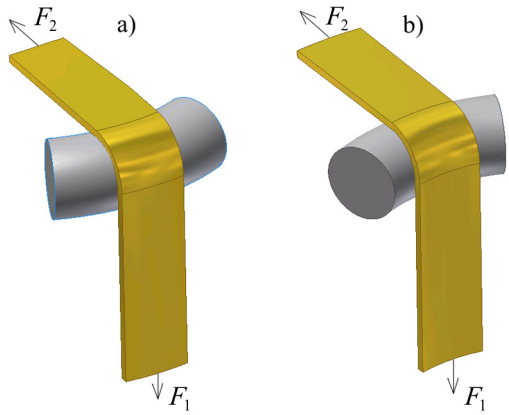

Fig. 4. *Proposed methods of determination of friction coefficient on die edge with a) convex and b) concave profile*

The greater the curvature of the tool edge, the more the strain state occurring in the contact area deviates from the plane strain state occurring in a classic BUT test. The value of the bending force increases nonlinearly with increasing degree of deformation of the sheet resulting from the strain-hardening phenomenon. To separate the frictional and bending resistances, the pulling force must be determined in conditions that eliminate the friction between the sheet and the counter-sample.

4 NUMERICAL SIMULATION OF THE PROPOSED APPROACH

The shape of the die and the punch profile determines the occurrence of the specific distribution and the value of strains in the sample, and the distribution of contact shear stress. To compare the mentioned parameters, the numerical simulations for the three profiles of counter-samples (cylindrical, convex and concave) were carried out. The radius of the die edge rounding was 7.5 mm, and the radius of the curvature for counter-samples with concave and convex contours was 40 mm. The material is assumed to be deep drawing quality (DDQ) steel sheet with a thickness of 1.5 mm. The width and the length of the sample were 85 mm and 11 mm, respectively. The sample was modelled with eight-node reduced integration, general-purpose linear brick elements, called C3D8R in ABAQUS terminology. Kim et al. [18] and Ramezani et al. [19] successfully used these types of elements to study the contact pressure distribution in BUT test.

An elasto-plastic material model approach has been implemented. The plastic behaviour of the metal is described by the von Mises yield criterion. Further, an isotropic strain hardening described by Hollomon's law with C and n parameter values according to the values in Table 1 are assumed. The rest of mechanical parameter values are assumed as follows:

- Young's modulus $E = 210000$ MPa,
- Poisson's ratio $\nu = 0.3$,
- density $\rho = 7860$ kg·m^{-3}.

To analyse the influence of different counter-sample profiles on the strain and pressure distribution, the contact phenomena in all cases are considered the same. The friction properties are described by Coulomb's law of friction coefficient whose value is equal to 0.2. One end of the sheet is restrained, while a displacement equal to 4 mm is applied to the second end.

The strain distribution for the third analysed counter-sample profiles, corresponding to this displacement, is shown in Fig. 5. The counter-sample profile determines the distribution and values of equivalent plastic strain of the sheet; for the concave profile (Fig. 5b) the maximum pressure is greater, whereas for the convex profile (Fig. 5c) it is less than the maximum plastic strain obtained for the cylindrical profile (Fig. 5a).

As depicted in Fig. 6, in the cross section of the bend sample a neutral layer exists on which the sign of the longitudinal strains is changed.

In the middle part of the sample width on the internal side, there are longitudinal compressive

Table 1. *The mechanical properties of DDQ steel sheet* [20]

Sample orientation	Yield stress R_e [MPa]	Ultimate tensile strength R_m [MPa]	Hardening coefficient C [MPa]	Hardening exponent n	Lankford's coefficient
0°	162	310	554	0.21	1.55
45°	163	322	542	0.20	1.27
90°	168	312	530	0.21	1.67
average value	164.3	314.7	542	0.207	1.497

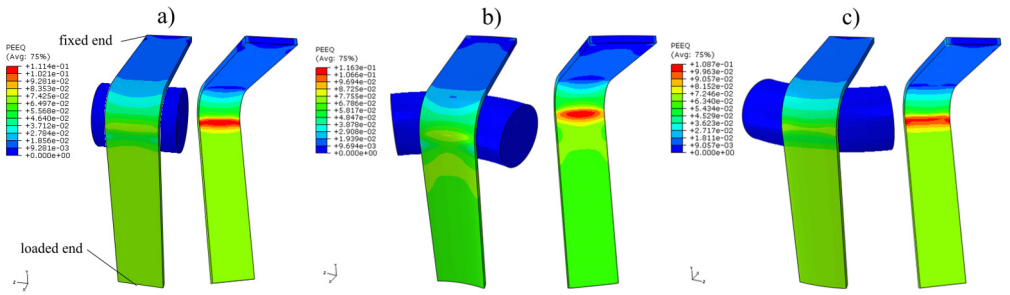

Fig. 5. *Distribution of equivalent plastic strain after sheet elongation of 4 mm for edges of a) cylindrical, b) concave and c) convex profile*

stresses, and the strain increment is negative; on the external side, the longitudinal stresses are negative, and the strain growth is negative.

At the sample edge, the aforementioned stress and strain state is disturbed (Fig. 6) by increasing the longitudinal dimensions of the tensional layers and reducing the corresponding dimensions of the compressed layers of the sample. The use of cylindrical counter-samples in the BUT test disturbs the initial rectangular cross-section of the sample, and the middle part of the sample width is also curved.

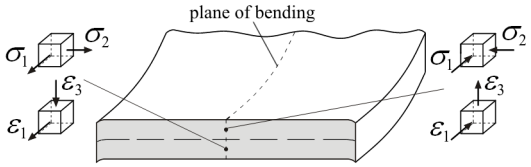

Fig. 6. *Stress and strain state during bending of sheet strip, σ – stress, ε - strain*

After the elongation of the sample by 2 mm, the distribution of contact pressure at surface nodes (Fig. 7) is not uniform across the width of the sheet, even when using a cylindrical counter-sample (Fig. 8). The large ratio of the width to the thickness of the sample (20/1) determines the occurrence of a specific stress and strain state on the sample thickness.

There is a significant difference in the value of the maximum pressure for the analysed profiles, from about 146 MPa for cylindrical counter-sample (Fig. 7a) to about 178 MPa for counter-sample with concave profile (Fig. 7c).

Such a large difference in the pressure between these profiles confirms the hypothesis of the existence of different conditions of friction and necessitates using the proposed method for determining the coefficient. After the samples were stretched to 4 mm, the difference between the maximum values of pressure for all counter-samples varied between 8 (Figs. 7a and 8a) and 15 MPa (Figs. 7c and 8c). It is also noted that there is a clear difference in the location of maximum pressure for the convex profile (Figs. 7b and 8b) and concave profile (Figs. 7c and 8c). The increase of the sample strain implies that contact pressure peaks appear near the entry and exit regions of the strip (Fig. 8), which is in agreement with the results of Kim et al. [5]. Contact pressure evolution at the die radius in sheet metal forming is studied by Pereira et al. [21], who identified three distinct phases through the numerical analysis of the BUT test: bending, an intermediate stage when the region of the sheet that was deformed at the start of the die radius has not reached the side-wall, and the final stage, which exhibits steady state contact conditions at the die radius.

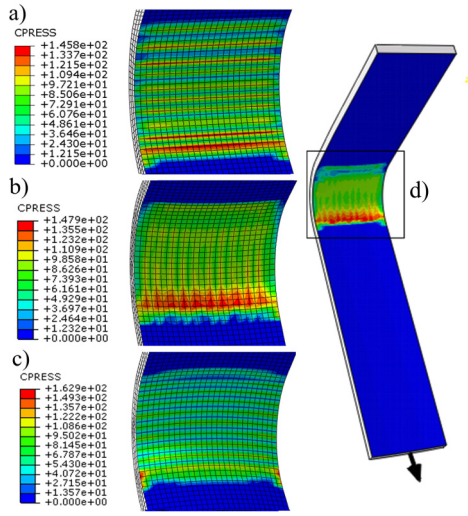

Fig. 7. *Distribution of contact pressure [MPa] on the sheet surface after sheet elongation of 2 mm for edge of a) cylindrical, b) convex and c) concave profile; d) location of contact pressure measurement*

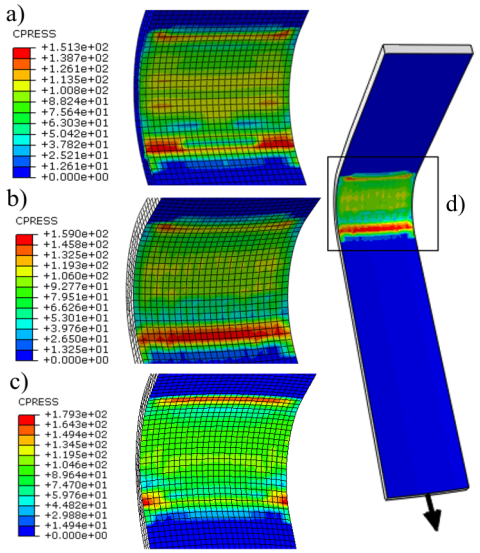

Fig. 8. *Distribution of contact pressure (MPa) on the sheet surface after sheet elongation of 4 mm for edge of a) cylindrical, b) convex and c) concave profile; d) location of contact pressure measurement*

5 VERIFICATION OF METHOD

5.1 Experimental Procedure

The schematic view of the test device is shown in Fig. 11. A test strip was held at one end in a grip supported by a load cell. A specimen of 8 mm width

and 1 mm thick (no. 3 in Fig. 9) is wrapped around a cylindrical fixed roll with diameter of 20 mm and loaded in a tensile testing machine ensuring contact at an angle of 90°. The application of the fixed pin allows setting up the rolls in four positions to utilize the full circumference of the roll. The test was carried out using the roll made of tool steel with roughness qualities Ra = 0.32 µm measured parallel with the roll axis.

The forces F_1 and F_2 were measured simultaneously during the test. A major advantage of this test apparatus is that strain does not have to be measured to determine the coefficient of friction. For some tests, the effect of strain on the value of the coefficient of friction may be of interest.

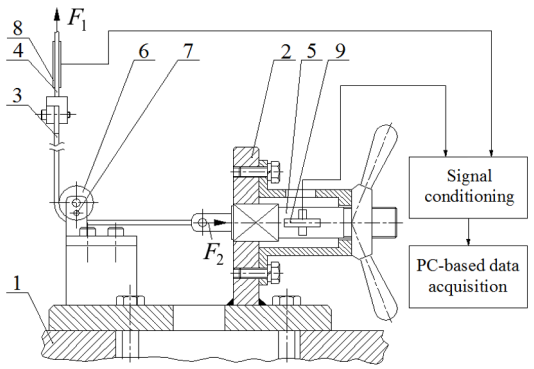

Fig. 9. *Schematic view of testing device; 1 – machine base, 2 – device frame, 3 – specimen, 4 and 5 – tension members, 6 – working roll, 7 - fixing pin, 8 and 9 – strain gauges*

5.2 Numerical Modelling

We simulated a numerically frictionless BUT test by assuming that the friction coefficient value between the sheet and the counter-sample was μ=0. The sample was modelled with eight-node reduced integration C3D8R brick elements. To the best possible description of the frictionless conditions of a real BUT test, Hill's anisotropic (1948) [22] material formulation with isotropic strain hardening was implemented in the finite element (FE) model. The rest of the parameters and the mechanical property values are given in Section 4.

6 DISCUSSION OF RESULTS

The values of both the pulling F_1 and back tension F_2 forces increase linearly after sample yielding and then increase proportionally (Fig. 10). Furthermore, the relation between forces and the friction condition does not change for a sheet's true strain above about 0.15. In the case of small contact pressures (true strain below 0.15), the friction coefficient increases with a true strain, which is in agreement with results of Ramezani et al. [19]. Friction coefficient of materials with little hardening capacity quickly increases at relatively small pressure. An additional comparison of pulling and back tension forces determined for different roughness qualities Ra (0.32 µm, 0.63 µm and 2.5 µm) and friction conditions (dry – dry friction, oil – lubrication conditions) shows that the F_1/F_2 ratio depends on pin roughness and friction conditions. The blue line in Fig. 11 represents when both forces are equal, i.e. $F_1 = F_2$. The F_1/F_2 ratio value increases faster for higher values of pulling force.

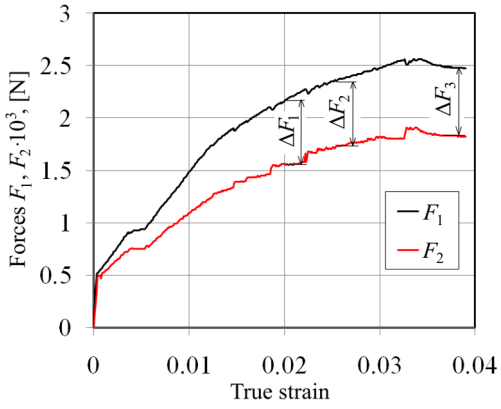

Fig. 10. *Values of forces during friction tests conducted in fixed roller conditions*

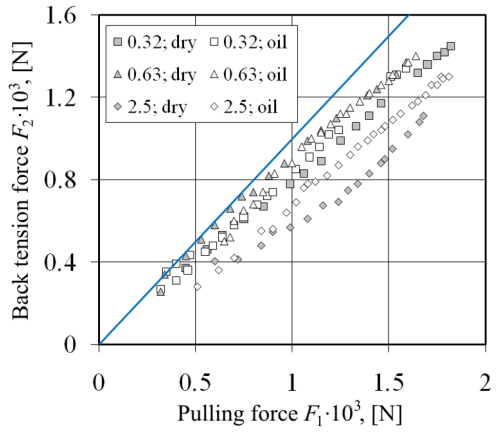

Fig. 11. *Comparison of pulling F_1 and back tension F_2 forces determined for different roughness qualities Ra (0.32, 0.63 and 2.5 µm) and friction conditions (dry – dry friction, oil – lubrication conditions)*

For bending force value evaluated as the difference between pulling and back tension force values in the case of a freely rotating pin, similar characteristics are observed (Fig. 12). The freely

rotating pin did not eliminate the friction between the counter-sample and its fastening, so the bending force value varied during the test. In the case of an FE model, there are small variations of bending force in the whole range of values of sample true strains, because it is possible to eliminate the friction in the test in the numerical model. This is one advantage of the numerical evaluation of bending force in a BUT test.

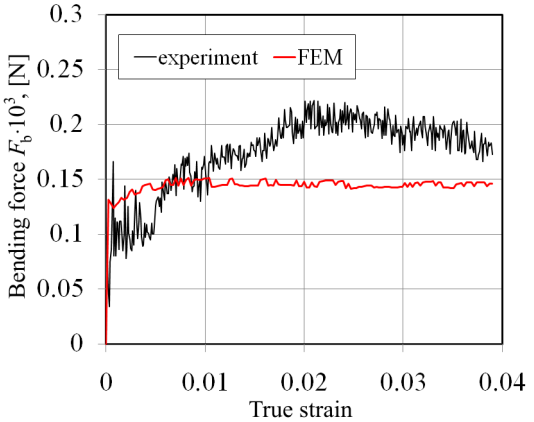

Fig. 12. *Comparison of variation of bending force value determined experimentally and numerically*

The increasing of sample strain allows an intensification of flattening of surface peaks. The scratches parallel to the sliding direction allow the identification of abrasion by grooving as the main contact mechanism. Simultaneously, it leads to a reduction of the volume of the valleys in the surface topography, which are mainly working as oil-reservoirs (Fig. 13).

The effectiveness of the supply of lubrication at the contact zones described by the WC index is studied by Wihlborg and Crafoord [3]. The increasing of real contact area is related to peaks flattening and the change of the surface topography because of sample stretching. Furthermore, during the deformation of the sheet metal over a tool, contact occurs only at the peak asperities of both surfaces, as concluded by Figueiredo et al. [23]. The frictional response in a BUT test under mixed lubricated condition was measured by Wiklund et al. [24], who found the larger the number of oil pockets, the lower the friction. The lubricant is squeezed out on the contact spots and thus the friction is decreased. The contact conditions of anisotropical surfaces are probably not highly dependent on the sliding direction, but the increasing of active oil pockets (Fig. 13) can considerably decrease the friction. Podgornik et al. [25] and [26] investigated and compared different surface modification techniques in terms of galling properties when applied to forming tools. They concluded that the galling tendency can be greatly reduced by proper polishing of the tool surface. Based on the results of friction tests in different friction conditions, Sedlaček et al. [27] have also found the most important surface roughness parameters describing work-piece topography.

Based on the process forces of the experimental BUT test realized in fixed roller conditions and bending forces determined by experiment and numerical method, the friction coefficient value (Fig. 14) was determined by using Eq. (6). For small values of the sample true strain, a transient region of variation of the friction coefficient value is observed, because the used strain gauges can produce inaccurate forces values in the case of small measured values of forces.

In the range of the true strain of 0.01 to 0.04, the average friction coefficient value determined experimentally equals about 0.15. The test forces in this range increase continuously but the difference between them ΔF is quite similar $\Delta F_1 \sim \Delta F_2 \sim \Delta F_3$ (Fig. 12). This relation is in excellent agreement with the

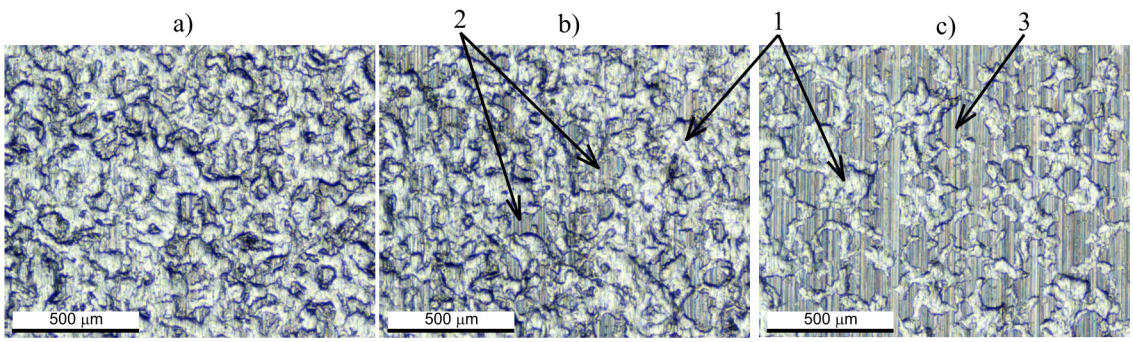

Fig. 13. *Surface topography of DDQ steel sheet: a) original, b) after sheet true strain 0.15 and c) after sheet true strain 0.3; oil lubrication conditions: 1 – oil pockets, 2, 3 – scratches*

results of Fratini et al. [28], who studied the influence of different lubricants on the reduction of friction in the BUT test. The main impact on the value of the friction coefficient for the analysed counter-sample shape has the values of pulling and back tension forces determined in case of the fixed pin. To take into consideration in Eq. (6) the numerically evaluated bending force $F_{bnum}=F_{1num}-F_{2num}$ allows preserving the trend of changes of the friction coefficient value (region A in Fig. 14).

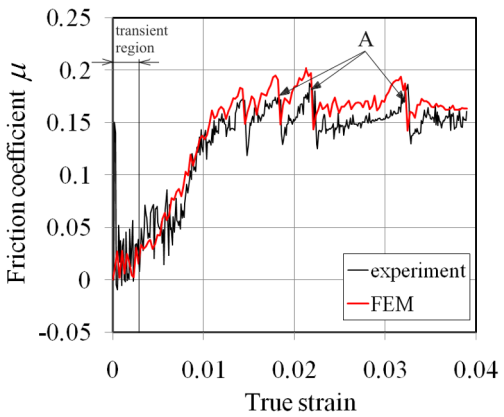

Fig. 14. *Variation of friction coefficient value determined experimentally and numerically*

7 SUMMARY

The proposed concept in this article allows the determination of friction coefficient in the case of dies with varying outline curvatures and varying radii of edge fillets. The state of stress at the rounded edges of the die and punch is determined by the geometry of these edges and has a significant impact on the plastic deformation nature of the sheet and consequently changes its topography.

The counter-sample profile determines the distribution and values of equivalent plastic strain of the sheet: for the concave profile the maximum pressure is greater, whereas for the convex profile there is less maximum plastic strain obtained for the cylindrical profile. Different friction conditions of all analysed profiles are also determined by the distribution and value of contact pressure. The difference in the value of maximum contact pressure depends on the sample elongation and varies between 10 MPa and 30 MPa for all analysed die rounded profiles.

The values of pulling and back tension forces determined in the case of the fixed pin have the main impact on the value of friction coefficient for the analysed counter-sample shape. The bending force value has a smaller effect on the accuracy of friction coefficient value determination in the BUT test. The experimental investigations and numerical approach confirmed that the proposed experimental-numerical method can be useful for the determination of the friction coefficient in the rounded profile of dies.

8 REFERENCES

[1] Volk, M., Nardin, B., Dolšak, B. (2011). Application of numerical simulations in deep-drawing process and holding system with segments' inserts. *Strojniški vestnik - Journal of Mechanical Engineering*, vol. 57, no. 9, p. 697-703, **DOI:10.5545/sv-jme.2010.258**.

[2] Stachowicz, F., Trzepieciński, T., Pieja, T. (2010). Warm forming of stainless steel sheets. *Archives of Civil and Mechanical Engineering*, vol. 10, no. 4, p. 85-94, **DOI:10.1016/S1644-9665(12)60034-X**.

[3] Wihlborg, A, Crafoord, R. (2001). Steel sheet surface topography and its influence on friction in a bending under tension friction test. *International Journal of Machine Tools and Manufacture*, vol. 41, no. 13-14, p. 1953-1959, **DOI:10.1016/S0890-6955(01)00060-8**.

[4] Hilditch, T.B., Speer, J.G., Matlock, D.K. (2007). Influence of low-strain deformation characteristics of high strength sheet steel on curl and springback in bend-under-tension tests. *Journal of Material Processing Technology*, vol. 182, no. 1-3, p. 84-94, **DOI:10.1016/j.jmatprotec.2006.06.020**.

[5] Kim, Y.S., Jain, M.K., Metzger, D.R. (2012). Determination of pressure-dependent friction coefficient from draw-bend test and its application to cup drawing. *International Journal of Machine Tools & Manufacture*, vol. 56, p. 69-78, **DOI:10.1016/j.ijmachtools.2011.12.011**.

[6] Miguel, V., Coello, J., Calatayund, A., Manjabacas, M.C., Martínez, A., Ferrer, C. (2009). An approach to evaluation of sheet bending force under successive multiaxial stress condition. *Journal of Materials Processing Technology*, vol. 209, no. 3, p. 1588-1596, **DOI:10.1016/j.jmatprotec.2008.04.016**.

[7] Deng, Z., Lovell, M.R. (2000). Effects of lubrication and die radius on the friction behavior of Pb-coated sheet steels. *Wear*, vol. 244, no. 1-2, p. 41-51, **DOI:10.1016/S0043-1648(00)00430-0**.

[8] Lovell, M.R. Deng, Z. (2002). Characterization of interfacial friction in coated sheet steels: influence of stamping process parameters and wear mechanisms. *Tribology International*, vol. 35, no. 2, p. 85-95, **DOI:10.1016/S0301-679X(01)00097-4**.

[9] Andreasen, J.L., Olsson, D.D., Chodnikiewicz, K., Bay, N. (2006). Bending under tension test with direct friction measurement. *IMechE Part B Journal of Engineering Manufacture*, vol. 220, no. 1, p. 73-80, **DOI:10.1243/095440505X32913**.

[10] Ceron, E., Bay, N. (2013). A methodology for off-line evaluation of new environmentally friendly tribo-systems for sheet metal forming. *CIRP Annals – Manufacturing Technology*, vol. 62, no. 1, p. 231-234, **DOI:10.1016/j.cirp.2013.03.062**.

[11] Garza, L.G., Van Tyne, C.J. (2007). Friction and formability of galvannealed interstitial free sheet steels. *Journal of*

Materials Processing Technology, vol. 187-188, p. 164-168, **DOI:10.1016/j.jmatprotec.2006.11.062**.

[12] Alinger, M.J., Van Tyne, C.J. (2003). Evolution of die surfaces during repeated stretch-bend sheet steel deformation. *Journals of Materials Processing Technology*, vol. 141, no. 3, p. 411-419, **DOI:10.1016/S0924-0136(03)00390-X**.

[13] Wiklund, D., Rosén, B.-G., Wihlborg, A. (2009). A friction model evaluated with results from a bending-under-tension test. *Tribology International*, vol. 42, no. 10, p. 1448-1452, **DOI:10.1016/j.triboint.2009.05.008**.

[14] Pereira, M.P., Duncan J.L., Yan W., Rolfe B.F. (2009). Contact pressure evolution at the die radius in sheet metal stamping. *Journal of Materials Processing Technology*, vol. 209, no. 7, p. 3532-3541, **DOI:10.1016/j.jmatprotec.2008.08.010**.

[15] Lemu, H.G., Trzepieciński, T. (2013). Numerical and experimental study of frictional behavior in bending under tension test. *Strojniški vestnik – Journal of Mechanical Engineering*, vol. 59, no. 1, p. 41-49, **DOI:10.5545/sv-jme.2012.383**.

[16] Figueiredo, L., Ramalho, A., Oliveira, M.C., Menezes, L.F. (2011). Experimental study of friction in sheet metal forming. Wear, vol. 271, no. 9-10, p. 1651-1657, **DOI:10.1016/j.wear.2011.02.020**.

[17] Hadoush, A., van den Boogaard, A.H., Emmens, W.C. (2011). A numerical investigation of the continuous bending under tension test. *Journal of Materials Processing Technology*, vol. 211, no. 12, p. 1948-1956, **DOI:10.1016/j.jmatprotec.2011.06.013**.

[18] Kim, Y.S., Jain, M.K., Metzger, D.R. (2004). A finite element study of capstan friction test. *AIP Conference Proceedings*, vol. 712, p. 2264-2269, **DOI:10.1063/1.1766872**.

[19] Ramezani, M., Neitzert, T., Pasang, T., Sellès, M.A. (2014). Characterization of friction behaviour of AZ80 and ZE10 magnesium alloys under lubricated contact condition by strip draw and bend test. *International Journal of Machine Tools & Manufacture*, vol. 85, p. 70-78, **DOI:10.1016/j.ijmachtools.2014.05.006**.

[20] Trzepieciński, T. (2010). 3D elasto-plastic FEM analysis of the sheet drawing of anisotropic steel sheet metals. *Archives of Civil and Mechanical Engineering*, vol. 10, no. 4, p. 95-106, **DOI:10.1016/S1644-9665(12)60035-1**.

[21] Pereira, M.P., Yan, W., Rolfe, B.F. (2008). Contact pressure evolution and its relation to wear in sheet metal forming. *Wear*, vol. 265, no. 11-12, p. 1687-1699, **DOI:10.1016/j.wear.2008.04.042**.

[22] Hill, R. (1948). A theory of the yielding and plastic flow of anisotropic metals. *Proceedings of the Royal Society of London*, vol. 193, p. 281-297, **DOI:10.1098/rspa.1948.004**.

[23] Figueiredo, L., Ramalho, A., Oliveira, M.C, Menezes, L.F. (2011). Experimental study of friction in sheet metal forming. Wear, vol. 271, no. 9-10, p. 1651-1657, **DOI:10.1016/j.wear.2011.02.020**.

[24] Wiklund, D., Rosén, B.-G., Gunnarsson, L. (2008). Frictional mechanisms in mixed lubricated regime in steel sheet metal forming. *Wear*, vol. 264, no. 5-6, p. 474-479, **DOI:10.1016/j.wear.2006.08.032**.

[25] Podgornik, B., Hogmark, S. (2006). Surface modification to improve friction and galling properties of forming tools. *Journal of Materials Processing Technology*, vol. 174, no. 1-3, p. 334-341, **DOI:10.1016/j.jmatprotec.2006.01.016**.

[26] Podgornik, B., Hogmark, S., Sandberg, O. (2006). Proper coating selection for improved galling performance of forming tool steel. *Wear*, vol. 261, no. 1, p. 15-21, **DOI:10.1016/j.wear.2005.09.005**.

[27] Sedlaček, M., Vilhena, L.M.S., Podgornik, B., Vižintin, J. (2011). Surface topography modelling for reduced friction. *Strojniški vestnik - Journal of Mechanical Engineering*, vol. 57, no. 9, p. 674-680, **DOI:10.5545/sv-jme.2010.140**.

[28] Fratini, L., Lo Casto, S., Lo Valvo, E. (2006), A technical note on an experimental device to measure friction coefficient in sheet metal forming. *Journal of Materials processing Technology*, vol. 172, no. 1, p. 16-21, **DOI:10.1016/j.matprotec.2005.08.008**.

Strojniški vestnik - Journal of Mechanical Engineering 61(2015)6, 392-398
DOI:10.5545/sv-jme.2014.2364
Original Scientific Paper
Received for review: 2014-12-10
Received revised form: 2015-04-07
Accepted for publication: 2015-04-22

A Model for the Estimation of Brake Interface Temperature

Aleksandar Grkić[1]*–Davorin Mikluc[1] – Slavko Muždeka[1] – Živan Arsenić[2] – Čedomir Duboka[3]

[1] University of Defence, Military Academy, Serbia
[2] University of Belgrade, Faculty of Mechanical Engineering, Serbia
[3] University of Belgrade, Serbia

The temperature achieved at the contact surface of the disc and the pad of a friction brake during its operation has a significant impact on brake performance. Temperature measurement techniques, which are usually available under laboratory test conditions, enable obtaining relatively accurate values of the temperature at the friction surface. However, measuring the sliding surface temperature during the entire lifetime of the brake pad is very difficult due to the demanding operating conditions of the brakes, i.e. the appearance of wear, the presence of water, corrosion, and other immersive impacts. Purely mathematical models for the prediction of friction or contact surface temperature are often complex, and they are affected by a number of limitations. In this paper, an appropriate mathematical model was developed in order to enable estimation of the sliding surface temperature values between the brake disk and brake pads throughout the entire duration of brake application. This is achieved by using the results of the temperature measurement within the brake pad and its processing, by means of an originally developed mathematical model.

Keywords: temperature estimation, braking, friction surface, measurement, modelling

Highlights

- *Available temperature measurement techniques and mathematical models for prediction of contact surface temperature.*
- *Measuring the temperature of the frictional surface and within the brake pad by using thermo couples.*
- *The model for estimation of temperature on the contact surface of the disc and the pad.*
- *Analysis of results and validation of the mathematical model.*

0 INTRODUCTION

The braking process is a complex stochastic tribological process by which the motion energy of vehicles is irrevocably transferred into heat and dissipated into the environment. Generally, the amount of heat is a time-related function, depending on the thermal characteristics of the parts enabling friction contact, as well as their size, shape, activation pressure, and sliding speed [1] and [2] .

The temperature on the friction surfaces of automotive brakes can reach very high values. In this sense, it is an influential factor of the brakes' performance [3] to [7]. According to [8], the temperature distribution on the friction surfaces is generated by combined processes and complex phenomena that directly affect brake performance. High temperatures on the friction surface may cause the decrease in efficiency of braking, so called fading [9]. Moreover, extremely high temperatures can cause convex bending of the brake pads and an uneven distribution of pressure leading to uneven wear rate distribution [10].

In [11], it was shown that brake factor values differ significantly depending on the variation of brake interface temperature, which is quite uniform under the same initial brake temperature. This means that, depending on the initial brake temperature, deceleration and braking time significantly differ from one braking application to another. Taking into consideration that the initial brake rotational speed and control line pressure take predetermined and well-known values, knowing the temperature values of the contact surface enables estimating the coefficient of friction in automotive brakes [12].

Having knowledge of the main influencing values at the initiation of the braking process, and also during braking process, enables the prediction of the output brake parameters, i.e. brake performance can be predicted and thus managed. However, in order to ensure a reliable and efficient management of the braking process, it is necessary to continuously obtain information concerning the actual values of the braking influential parameters. Consequently, it is vital to have knowledge about the temperature on the contact surface of the disk and the brake pads throughout the braking application duration.

It is very difficult to measure and predict the values and character of temperature changes in the brake. Temperature measurements on the contact surface are practically impossible over a longer period, due to the physics of the friction process. Apart from that, automotive brakes work in difficult operating conditions, which is reflected in the appearance of wear, the presence of water, corrosion and so on. Through this task, it is possible to apply several

*Corr. Author's Address: MilitaryAcademy, University of Defence in Belgrade, VeljkaLukica-Kurjaka 33, Serbia, iralex@eunet.rs

different temperature non-contact measurement methods [13], such as optical and infrared methods, and contact type methods, as well as temperature measurement using thermo-couples or different temperature-sensitive materials. According to [14], the most effective way to determine the temperature on the contact surface of the disc and brake pads in the vehicle during braking is by applying thermocouples.

In contrast, a number of authors used different mathematical methods to describe and present temperatures in the contact zone of the friction pair and the behaviour of the temperature field in the braking process, as well as their impact on wear and brake performance. The prediction of brake temperature in the contact surface can be realized in two ways: analytically and numerically [15] to [19]. The basis of the analytical method relies on the Fourier equation of temperature field [20], while the finite element method (FEM) [2] represents the most important numerical method. In recent years, the application of artificial intelligence (AI) methods (such as neural networks) has become a particularly interesting as a tool for predicting temperatures in automotive brakes [21].

All of the above-mentioned methods can provide satisfactory results in comparison the actual measurements. However, the application of any of these methods typically requires numerous simplifications and restrictions in order to offer solutions to the observed problem.

Taking this into consideration, this paper investigates the possibilities of estimating both the character in changes and the values in the contact surface temperature between the disc and brake pads. The developed model is based on the results of temperature measurements in the vicinity of the contact surface and in the depth of a brake pad. A model for estimating the temperature on the contact surface requires continuous information about the temperature values within brake pads by means of measurement. This is possible during the entire working life of brake pads.

1 EXPERIMENTAL RESEARCH

As previously stated, temperature measurement in the friction surfaces of a brake is a difficult task. This is due to numerous influencing factors specific to rubbing surfaces such as those in friction brakes, especially since it is necessary to provide temperature measurement with an appropriate accuracy and minimum delay.

When comparing all the available techniques of temperature measurement, the method using thermocouples shows significant advantages over others; they are very effective for measuring the temperature in the contact of the friction pair. In this case, a so-called "hot end" or hot junction is located very close to the friction surface.

However, it must be taken into consideration that the thermocouple should not at any time be exposed to direct rubbing over the friction surface in order to eliminate the potential impact on the quality of the measuring signal of the thermocouple sliding itself over the metal surface as much as possible.

This kind of problems may be avoided if the thermocouple is positioned within the pad, very close to the sliding surface, e.g. 0.5 mm deep from it (SAE J843). In the present study, one temperature sensor was located in such a position, and it will be used to measure the temperature on the friction surface (T_1). However, given the requirement that the temperature at the friction surface be measured throughout the lifespan of brake pads, this position is not satisfactory due to wearing phenomena.

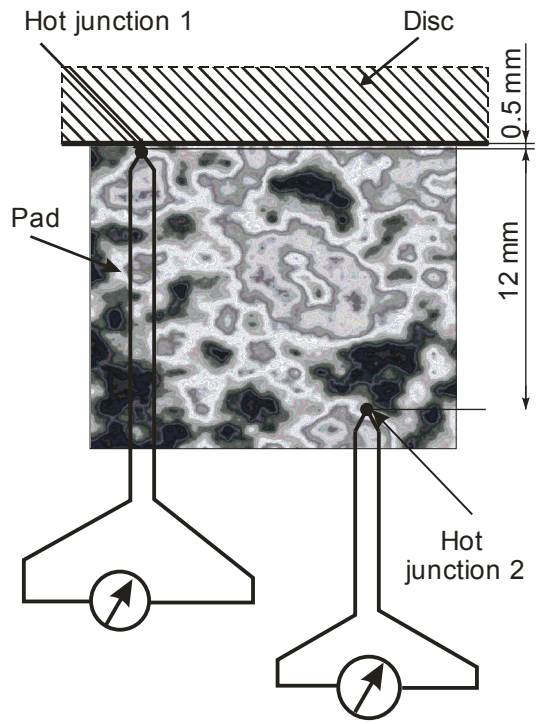

Fig. 1. *Position of thermocouples in brake pad*

Therefore, another thermocouple T_2 will be positioned 12.5 mm deep from the contact surface, within the pad, as shown in Fig.1. The position of this thermocouple is close to the backing plate, and it is defined by the thickness of the brake lining material. This thermocouple is not exposed to the effects

of wearing, which ensures its use throughout the operating period.

It is important to note that both thermocouples were placed at the friction radius of the pad.

Typical test results of the temperature measurement are presented in Fig. 2; the solid line shows temperature measurement results at the sliding surface (i.e. 0.5 mm deep from the friction surface), while the dahed dot line shows temperature measurement results 12.5 mm deep from the friction surface of the disc pad. The measurement was carried out at the Frimeks laboratory of the Faculty of Mechanical Engineering, University of Belgrade, with a car disc brake tested at a single-ended full-scale inertia dynamometer [11].

Temperature measurements were carried out during 5 consecutive (or repeated) full-stop brake applications over a total time of 600 seconds, with an initial brake speed corresponding to linear vehicle speed of 60 km/h, and with the control line pressure of 60 bar, while the initial brake temperature at the beginning of the measurement cycle was 100 ºC (±3 ºC). The brake was subject to cooling by means of the fan operating throughout the measurement period.

In each brake application, a brake disc was first accelerated until it reached the predetermined initial brake speed, and consequently braked to a full stop. After completing a single brake application, the brake disc remained at a standstill. Speeding up of the disc for the next brake application started a few moments before the brake attained a predetermined initial temperature of 100 ºC.

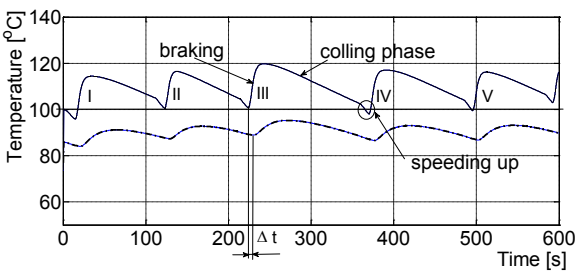

Fig. 2. *Temperatures measured in the disc pad for 5 consecutive brake applications*

This can also be seen in Fig. 2, where the change in the shape of the curve representing temperature measurement is evident in the area near the end of the cooling phase. This occurs because the brake temperature decreases significantly faster due to rotating disc during the speed build-up period. The delay in reaching the minimum temperature value at the depth of 12.5 mm from the sliding surface when compared to the minimum temperature "at the friction surface" is represented with the symbol Δt, as shown in Fig. 2.

2 TEMPERATURE MODELLING ON THE FRICTION SURFACE

The model for estimation of temperature on the contact surface of the disc and the pad is based on the temperature ratio (k), which is determined experimentally as a rate between temperatures T_1 and T_2 at hot junctions 1 and 2, respectively, as shown in Fig. 1 above, by means of the test results from Fig. 2.

The evaluation of k factor (temperature ratio) between temperatures T_1 and T_2 is shown in Fig.3.

As shown in Fig. 3, the values of k factor vary between k_{min}=1.14 and k_{max}=1.32. It may be seen from both Figs. 2 and 3 that k factor certainly depends and varies on whether the brake was in the warming (brake application) or cooling (brake release) phase.

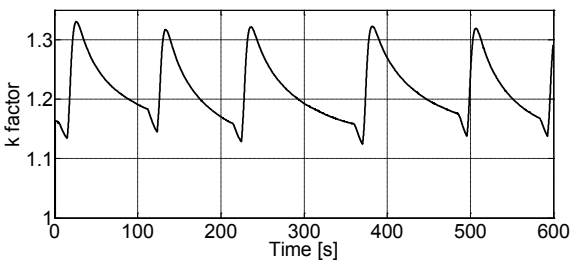

Fig. 3. *k-factor between temperatures T_1 and T_2*

Therefore, the k factor may be best represented by its mean value, which can be determined as follows:

$$k = \frac{k_{min} + k_{max}}{2}. \quad (1)$$

The estimated value of the temperature T_E, which represents the modelled values of the friction sliding surface temperature T_1 can be obtained by multiplying the temperature value T_2, which was measured in the depth of a pad with the mean value of the k factor.

Variations of k factor also depend on the composition of the brake pad friction material, wear status, brake geometry and operating conditions, as well as the position of thermocouple T_2 in the depth of friction material.

It is important to emphasize that this model for prediction of temperature on the friction surface is limited to the brake under examination only, in addition to the given friction material characteristics and the position defined for T_2 temperature measurement.

The temperature T_1 was not used in the model; it only represents control parameter in order to assess the quality of the model.

Fig. 4 shows the results already presented in Fig. 2 in order to enable first approximation in resolving this situation with the help of a new dashed line for T_E. This represents the results of continuous multiplication of the "pad inside temperature" T_2 values (dashed dot line) by the mean value of the k factor, thus obtaining a "predicted" value of the temperature T_E, which will correspond to the correct value of the temperature T_1 (solid line) in the contact surface, as measured during the test.

However, it is obvious that such an estimation of brake-sliding surface temperature is not only applicable to the given brake characteristics, including those related to the friction material used, but also to the given combination of the initial braking conditions (speed and pressure). The big question, in this case, would not be how to calculate the values of the sliding surface temperature accurately, but how to reach a universal relationship between the brake contact surface temperature and the temperature within the pad, i.e. at a given depth from the sliding surface.

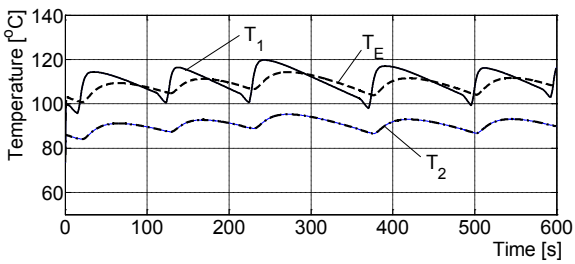

Fig.4. *Result of the correction of temperature T_2 (dashed dot line) by means of the k-factor for temperature T_E (dashed line) compared to temperature T_1 (solid line)*

It is evident that the estimated temperature T_E does not fully correlate with the temperature T_1on the contact surface, neither by value nor by shape, because it follows the shape of the temperature T_2. It is also apparent that the temperature T_2 demonstrates a certain delay in the gain, not only during the application or braking process, but also during free running in the cooling process. This is caused by the heat transfer through the friction material.

It is well known that the heat transfer through the friction pad is a highly complex issue, but the idea of this paper was not to study it in a more detailed form. The results of the measurement and calculation using the k factor shows that in addition to the proportionality between the measured and estimated temperature as defined by k factor, there must also be a certain influence of the time, speed, and the deceleration of the heat transfer through the friction pad, starting from the sliding surface and ending somewhere in the depth of it, where the temperature T_2 can be measured.

Bearing all this in mind, the model for the brake contact surface temperature estimation was developed in the following general form based on polynomial regression **[22]**:

$$T_E(t) = T_2(t) \cdot k + \frac{dT_2}{dt} \cdot t \cdot k_v + \frac{d^2T_2}{dt^2} \cdot \frac{t^2}{2} \cdot k_a, \qquad (2)$$

where T_E is the estimated brake interface temperature, T_2 the temperature measured within the pad, t the time, k the temperature ratio, and k_v, and k_a are coefficients representing speed and acceleration of temperature increase intensity, i.e. representing the coefficients of heat transfer through the friction material.

These coefficients also depend on the composition of the brake pad friction material, wear status, brake geometry and operating conditions, as well as the position of thermocouple T_2 in the depth of the friction material.

The coefficient of the speed of temperature increase intensity k_v is determined by fitting the estimated temperature T_E to the measured temperature T_1. This process is performed in the sequence of monotonous temperature change in order to avoid the influence of coefficient k_a from Eq. (2).

Because the estimated temperature T_E change does not fully correlate to that of the temperature T_1, neither by value nor by shape, the value of the coefficient k_v was calculated with a simple linear regression method based on the least squares criterion **[22]** and **[23]** using measurement data of T_1 and T_2 temperatures. Now, the coefficient k_a remains the only unknown parameter in Eq. (2). The least squares criterion will give best value for parameter k_a for the process model using the polynomial regression method **[22]** and **[23]** between the measured temperatures T_1 and T_2. After this procedure, the estimated temperature T_E could be calculated.

The thus obtained estimated (i.e. calculated) brake contact surface temperature T_E is presented by means of the dashed line in Fig. 5, where it can be seen that estimated temperature T_E follows both the shape and the character of the behaviour of measured temperature T_1 very well, which seems to deviate from the actual value by not more than ± 3 ºC.

This deviation can be assumed to come from the noise of the measurement signal, being the result of

conditions by which measurement was carried out, and a high sampling rate selected, even though it is a relatively slow process.

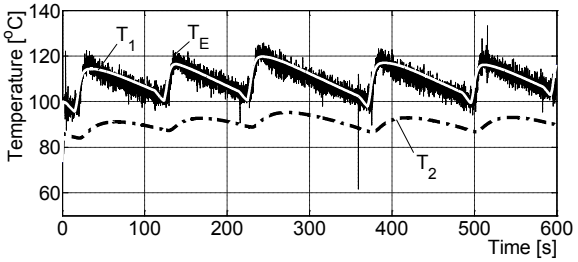

Fig. 5. *Estimated temperature T_E in the contact surface*

Apart from this, if we further note that the calculated temperature was obtained by including the first and the second derivative of temperature changes, then it becomes clear why the noise signal was so strong. The resulting signal is cleaned by applying a filter with constant coefficients; the proposed filter is the alpha-beta-gamma filter. Determination of α, β, and γ coefficients yields the following results according to **[24]**:

$$\alpha = 0.95\,, \tag{3}$$

$$\beta = 2\cdot(2-\alpha) - 4\cdot\sqrt{(1-\alpha)}, \tag{4}$$

$$\gamma = \frac{\beta^2}{2\cdot\alpha}. \tag{5}$$

Within the first step of determination, the signal of measured temperatures inside the brake pads was filtered, after which the estimation of temperature on the contact surface according to Eq. (1) was made. The result is a signal, i.e. the temperature at the contact surface (in black) as shown in Fig. 6; the figure shows that the filtered signal follows the actual (real) value of the measured temperature on the contact surface, with the average deviation of ± 1ºC, but there is also some delay when compared to the measured value.

The reason for this may be the choice of filters with constant coefficients, while the values of these thermal conductivity coefficients in friction material depend on the temperature changes on the contact surface.

Fig. 7 shows the delay in the estimated temperature value in relation to the measured temperature, which begins to increase at the same time as the temperature measured inside the disc pad.

The time of delay is proportional to the thickness of the friction material and the value of the difference between the temperature on the friction surface and inside the pads, respectively.

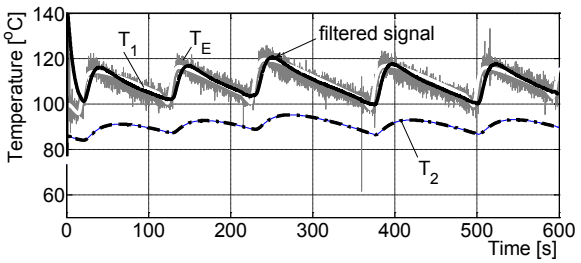

Fig. 6. *Results of signal filtering using α–β–γ filters*

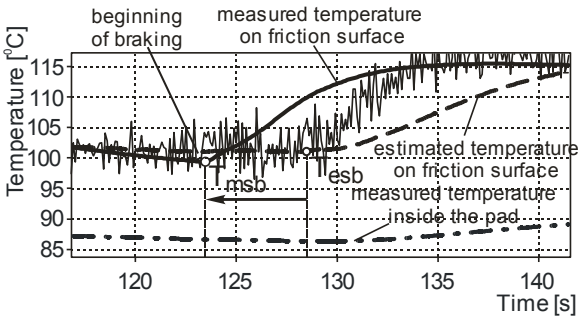

Fig. 7. *Delay in the estimated temperature value in relation to the measured temperature*

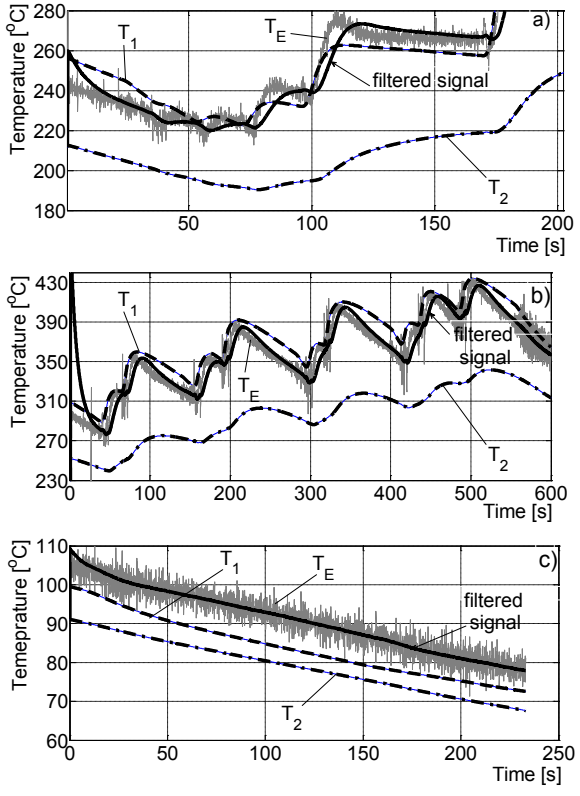

Fig. 8. *Estimation of temperature on the friction surface under different brake operating conditions*

Fig. 8 shows the results of the research on the estimation of the friction surface temperature during different brake-operating conditions.

Fig. 8a shows an estimated friction surface temperature under operating conditions of high braking temperatures, while Fig. 8b displays the results under operating conditions with extremely high temperatures.

In both cases, measurements were carried out during consecutive full-stop brake applications with an initial brake speed and control line pressure, different in relation to the test on the basis of which a mathematical model was introduced.

Fig. 8c shows the results of the evaluation of temperature in the cooling phase. The assessment was conducted using a previously described model without any change in the values of the coefficients *(k, k_v, k_a, α, β* and *γ*).

5 CONCLUSION

This paper presents the results of the estimation of the sliding surface temperature of a brake during the whole braking application. The estimated value of the contact surface temperature was obtained by means of the presented mathematical model, including the results of temperature measured inside the brake pad at a given depth.

Previous research shows that the estimated temperature on the contact surface follows the nature of the change in actual temperature very well, as well as the measured temperature on the contact surface with the average deviation around the actual value of ± 1ºC.

The presented model of estimation of temperature on the friction surface is limited to the brake under examination, in addition to the given friction material and the position defined by the second thermocouple, placed in the depth of the disc pad and the given operating conditions. Here, it was also shown that by using the presented model, the temperature on the friction surface can be assessed even in the case of different operating conditions (sliding velocity, pressure, and temperature), but with significant deviations.

The presented results reveal an evident delay of the assessed temperature flow compared to the temperature measured on the contact surface. The cause for this is heat transfer through the friction surface. In other words, based on the temperature inside the pads, one can fairly and accurately estimate the temperature on the friction surface during braking, but cannot be informed about the initial moment of braking.

Future research will relate to the creation of models with varying coefficients *k, k_v, k_a,* as a function of the operating conditions of the brake for other types of friction materials.

6 REFERENCES

[1] Ostermeyer, G.P., Graf, M. (2013). Influence of wear on thermoelastic instabilities in automotive brakes. *Wear*, vol. 308, no. 1-2, p. 113-120, **DOI:10.1016/j.wear.2013.09.009**.

[2] Day, A.J., Newcomb, T.P. (1984). Dissipation of frictional energy from the interface of an annular disc brake, *Proceedings of the Institution of Mechanical Engineers, Part D: Journal of Automobile Engineering*, vol. 198, no. 11, p. 201-209, **DOI:10.1243/PIME_PROC_1984_198_146_02**.

[3] Emery, A.F., Kumar, P., Firey, J.C. (1997). *Experimental Study of Automotive Brake Systems Temperature*s. Washington State Transportation Center (TRAC), University of Washington, Washington.

[4] Talati, F., Jalalifar, S. (2008). Investiga-tion of heat transfer phenomena in a ventilated disk brake rotor with straight radial rounded vanes. *Journal of Applied Science*s, vol. 8, no.20, p.3583-3592, **DOI:10.3923/jas.2008.3583.3592**.

[5] Litos, P., Honner, M., Lang, V., Bartik, J., Hynek, M. (2008). A measuring system for experimental research on the thermo mechanical coupling of disc brakes, *Proceedings of the Institution of Mechanical Engineers, Part D: Journal of Automobile Engineering*, vol. 222, no. 7, p. 1247-1257, **DOI:10.1243/09544070JAUT0593**.

[6] Bansal, D.G., Streator, L.J. (2009). A method for obtaining the temperature distribution at the interface of sliding bodies. *Wear*, vol. 266, no. 7-8, p. 721-732, **DOI:10.1016/j.wear.2008.08.019**.

[7] Cho, H.-J., Cho, C.-D. (2008). A study of thermal and mechanical behaviour for the optimal design of automotive disc brakes. *Proceedings of the Institution of Mechanical Engineers, Part D: Journal of Automobile Engineering*, vol. 222, no. 6, p. 895-915, **DOI:10.1243/09544070JAUT0722**.

[8] Talati, F., Jalalifar, S. (2009). Analysis of heat conduction in a disk brake system. Heat Mass Transfer, vol. 45, no. 8, p. 1047-1059, **DOI:10.1007/s00231-009-0476-y**.

[9] Duboka, Č., Arsenić,Ž., Milosavljević, M. (1996). Tribo-mutations in tribo-mechanical systems. *2nd International Conference on Tribology*, Thessalonniki.

[10] Eriksson, M., Bergman, F., Jacobson, S. (2002). On the nature of tribological contact in automotive brakes. *Wear*, vol. 252, no. 1-2, p. 26-36, **DOI:10.1007/s00231-009-0476-y**.

[11] Grkić, A., Mikluc, D., Perić, S., Duboka, Č. (2013). Prediction of disc brake contact surface temperatures. *24. International Automotive Conference Science and Motor Vehicle*, Belgrade.

[12] Grkic, A., Muzdeka, S., Arsenic, Z., Duboka, C. (2014). Model for estimation of the friction coefficient in automotive brakes under extremely high temperatures. *International Journal of Engineering and Technical Research*, vol. 2, no. 11, p. 290-294.

[13] Dinc, O.S.C., Ettles, M., Calabrese, S.J., Scarton, H.A. (1993). The measurement of surface temperature in dry or lubricated sliding. *Transaction of ASME, Journal of Tribology*, vol. 115, no. 2, p. 78-82, **DOI:10.1115/1.2920989**.

[14] Qi, H.S., Day, A.J. (2007).Investigation of disc/pad interface temperatures in friction braking. Wear, vol. 262, no. 5-6, p. 505-513, **DOI:10.1016/j.wear.2006.08.027**.

[15] Golubev, Yu. A., Ivanenko, V.V. (2009). A calculation method of energy intensity of brake lining wear as related to temperature. *Journal of Friction and Wear*, vol. 30, no. 4, p. 258-260, **DOI:10.3103/S1068366609040059**.

[16] Evtushenko, A.A., Ivanik, E.G. (1999).Evaluation of the contact temperature and wear of a composite friction pad in braking. *Journal of Engineering Physics and Thermophysics*, vol. 72, no. 5, p. 955-962, **DOI:10.1007/BF02699422**.

[17] Matysiak, S., Evtushenko, O., Kuciej, M. (2007).Temperature field in the process of braking of a massive body with composite coating. *Materials Science*, vol. 43, no. 1, p. 62-69, **DOI:10.1007/s11003-007-0006-3**.

[18] Yevtushenko, A.A., Kuciej, M. (2011). The thermal problem of friction for a three-element tribosystem with composite strip. *International Journal of Heat and Mass Transfer*, vol. 54, no. 25-26, p. 5427-5437, **DOI:10.1016/j.ijheatmasstransfer.2011.07.048**.

[19] Chichinadze, A.V. (2009). Theoretical and practical problems of thermal dynamics and simulation of the friction and wear of tribocouples. *Journal of Friction and Wear,* vol. 30, no. 3, 199-215, **DOI:10.3103/S106836660903009X**.

[20] Tirovic, M., Stevanovic, D., (1986). *Determination of temperature Field Disc Brake Pads*. MVM, Kragujevac.

[21] Ray, S., Chowdhury, S.K.R. (2009). Prediction of contact temperature rise between rough sliding bodies: An artificial neural network approach. *Wear*, vol. 266, no. 9-10, p. 1029-1038, **DOI:10.1016/j.wear.2009.02.016**.

[22] Weisberg, S. (2005). *Applied Linear Regression*, John Wiley & Sons, Hoboken, **DOI:10.1002/0471704091**.

[23] Grossman, M. (1971). Parametric curve fitting, The Computer Journal, vol. 14, no. 2, p. 169-172, **DOI:10.1093/comjnl/14.2.169**.

[24] Tenne, D., Singh T. (2002). Characterizing performance of α-β-γ filters. *Aerospace and Electronic Systems, IEEE Transactions*, vol. 38, no. 3, p. 1072-1087, **DOI:10.1109/TAES.2002.1039425**.

Strojniški vestnik - Journal of Mechanical Engineering 61(2015)6, 399-408
DOI:10.5545/sv-jme.2015.2490
Original Scientific Paper
Received for review: 2015-02-04
Received revised form: 2015-04-22
Accepted for publication: 2015-05-18

Investigation of Drag and Churning Losses on Tapered Roller Bearings

Jürgen Liebrecht[1,*] – Xiaojiang Si[2] – Bernd Sauer[1] – Hubert Schwarze[2]

[1] University of Kaiserslautern, Institute for Machine Elements, Gears and Transmissions, Germany
[2] University of Clausthal-Zellerfeld, Institute of Tribology and Energy Conversion Machinery, Germany

Today there are a lot of findings to determine losses caused by contact forces inside roller bearings. But there are also losses in bearings caused by displacement of lubricant. These are known as churning or drag losses. In general the bearing manufacturers give recommendations how to reduce them. The most common solution is the reduction of the oil bath level. Some bearing manufacturers even provide models or empirical equations to calculate the resistance resulting from rolling elements moving through the oil. These models take the operating conditions such as the viscosity of the oil at the operating temperature, oil level, bearing type and rotational speed into consideration. A comparison between calculated and experimental results shows that there is still a deviation because of further effects which are not considered in those analytical models. This paper presents experimental studies and numerical simulations which illustrate the influence of the oil quantity on the total friction torque of tapered roller bearings and identify the resulting losses.

Keywords: tapered roller bearing, churning losses, drag losses, frictional torque, CFD simulation

Highlights

- *Method for investigation of drag and churning losses.*
- *Influence of viscosity, oil quantity and rotational speed.*
- *CFD simulation of a single-phase flow considering air content in lubricant.*
- *Influence of the air content on the drag and churning losses.*

0 INTRODUCTION

Frictional torque is a significant parameter to describe the efficiency of a roller bearing. It is a result of internal friction which influences the heat generation in the bearing and also determines its losses. The total losses of a bearing can be divided into two parts. The main part is the mechanical friction. It results from contact forces between rolling elements and the runway, the cage and the board contact. The second part of total friction is caused by displacement of lubricant, called churning and drag losses **[1]**. These hydraulic losses become important because they depend on the operating conditions, and can be as high as the mechanical losses (i.e., **[2]** to **[4]**).

To determine the total friction torque bearing manufacturers provide equations (e.g., **[5]**). In these equations various factors are used to consider the influences of the lubrication. Some of these influencing factors are considered by approximation.

To predict the influence of lubricant displacement on the total friction torque the Institute for Machine Elements, Gears and Transmissions (MEGT) and the Institute of Tribology and Energy Conversion Machinery (ITR) investigate the effects associated with oil lubrication. At the MEGT experimental studies under different test conditions have been carried out. For numerical analysis and description of fluid effects ITR used CFD simulation (i.e., **[6]** and **[7]**). The research focus is on axially loaded bearings with a vertical axis of rotation. This concept provides symmetrical operating conditions with a view to uniform lubricant distribution in the bearing. Furthermore symmetrical construction enables the simplification of the simulation model so that only a section of the roller bearing can be considered in the simulation.

Experimental studies focused on the influences of viscosity, cage geometry, bearing type, rotational speed and especially on different oil levels. Furthermore the experimental work includes research of the influence of oil foaming in the lubricant and its effect on the viscosity.

ITR used simulations to illustrate and to understand the significant effects and the fluid flow inside the bearing. Simulations include only-fluid-flow as well as two-phase flow. In this paper the first results of experimental studies and numerical simulations are presented.

1 TEST CONDITIONS

1.1 Test Rig

Conventional test rigs used to measure the total friction torque of bearings usually have a horizontal

*Corr. Author's Address: Institute for Machine Elements, Gears and Transmissons, Gottlieb-Daimler-Str., 67663 Kaiserslautern, Germany, j.liebrecht@mv.uni-kl.de

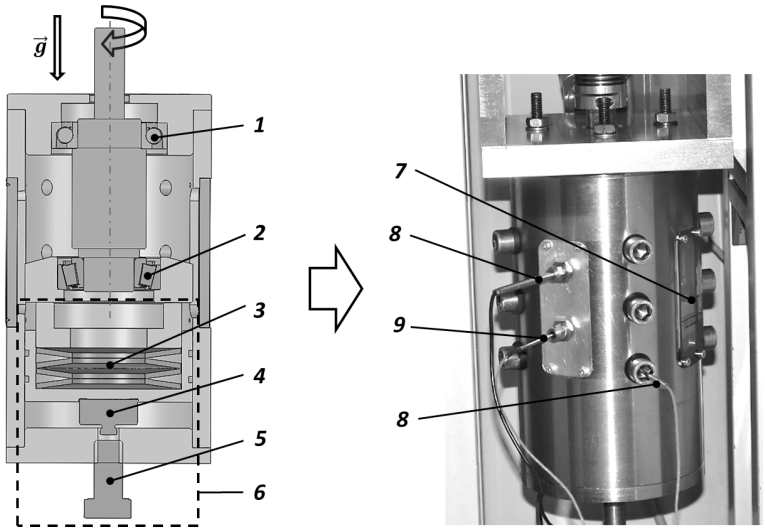

Fig. 1. *Sectional view and side view of the bearing test unit (1- support bearing (7210); 2- test bearing (32208); 3- disc springs; 4- force sensor; 5- axial load bolt; 6- axial load unit; 7- vision panel; 8- temp. sensors oil bath; 9- temp. sensor test bearing)*

orientated axis of rotation. The test rig used for the experimental studies is presented in Fig. 1. It has a vertical orientated shaft. The reason for using this concept is the equal load distribution and lubrication of the test bearing.

The concept involves the use of a test and a support bearing. The test bearing is the tapered roller bearing 32208. An angular contact ball bearing 7210 made of ceramics (ZrO_2) is used as a support bearing. The reason for the use of a ceramic bearing is its low friction so that the use of torque measuring sensors with a small range is possible. Furthermore the resolutions of the drag and churning losses have a higher accuracy. Measurements with two support bearings at once might be used to determine their friction torque and for calculating the friction torque of the test bearings. The bearings are mounted in x-arrangement in a test cylinder. The load application onto the bearing arrangement is done by a screw which pushes a force sensor and disk springs against the bearings. To observe the flow around the bearing four vision panels are attached around the test cylinder. For continuous monitoring of operating conditions sensors for measurement of the speed and temperature of the oil and the bearing's outer ring are used. There are two sensors for measurements of the oil temperature above and below the test bearing. For the application of the rotational speed an electrical engine is available which can be driven up to 10,000 rpm. To capture the drag losses a torque sensor is mounted between the engine shaft and the test shaft via couplings. Its measuring range is $M = 5$ Nm. The accuracy class of the sensor is 0.5. In this setup the required drive torque corresponds to the total friction torque of the bearing arrangement and is measured by the sensor.

The use of tapered roller bearings in oil bath lubrication involves a pumping effect (i.e., **[8]** and **[9]**). This effect is caused by the internal design of the bearing type. The experiment's configuration and bearing arrangement affects the oil flow upwards against gravity (Fig. 2). To provide a constant oil flow rate during the test, the test bearing housing has been modified. There is a slope and few grooves distributed

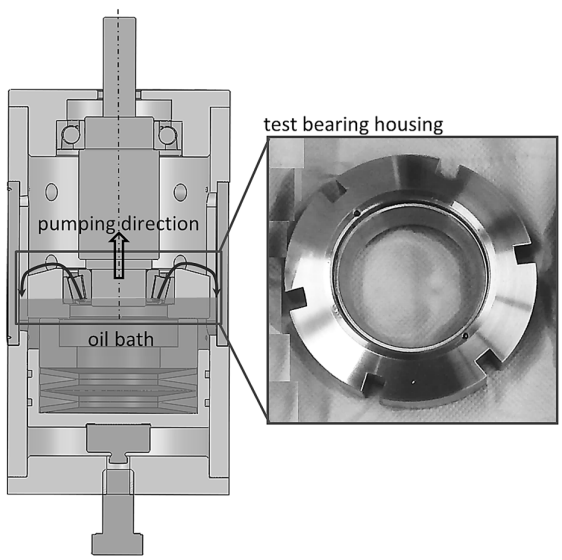

Fig. 2. *Modified test bearing housing for compensation of pump effect*

around the circumference through which the oil flow back.

1.2 Experimental Approach

Important influences on the total friction torque of a bearing are rotational speed, viscosity of the lubricant, load and oil bath level. The losses caused by the displacement of the lubricant can be regarded as independent of load. That is why the load is kept constant during the experimental studies. The oil level, viscosity and speed represent close-coupled parameters. A higher speed and load causes an increase of the oil and bearing temperature. That usually results in a lower oil viscosity and also lower drag and churning losses. To investigate the hydraulic losses resulting from the rotational speed or the oil level constant boundary conditions were defined. Fig. 3 presents the fully flooded and half flooded test bearing. Experiments with minimal quantity lubrication or injection lubrication provide the results which are used to determine the drag and churning losses. Those are the total friction torque differences between the mentioned oil levels.

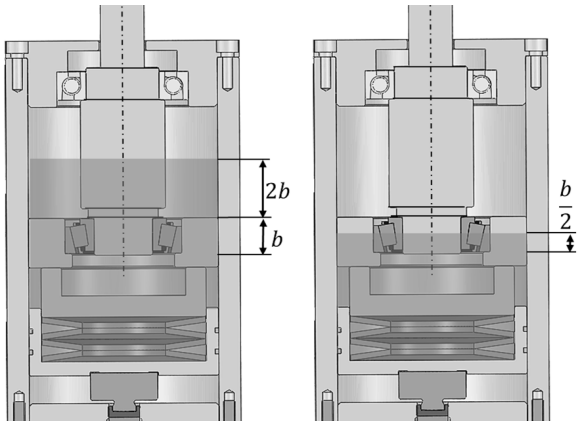

Fig. 3. *Different oil bath levels*

The oil level of the fully flooded bearing is as high as three times the bearing width. The difference between the total friction torque of the test bearing in flooded condition and the friction torque in the case of minimum quantity lubrication is caused by the hydraulic losses. For the validation of simulation models a speed range from n = 500 to 6300 rpm and a constant oil temperature of T = 60 °C were defined. Furthermore two reference oils were selected for the experimental studies. Both are mineral oils and unalloyed, their characteristics and viscosity depending on the temperature are presented in Fig. 4.

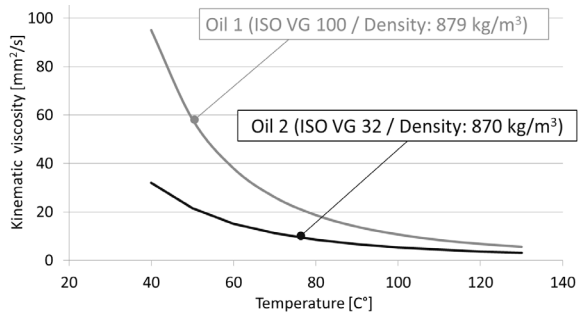

Fig. 4. *Effect of the temperature on the viscosity of the test oils*

Constant operating conditions are the prerequisite for constructive experimental studies. Their definition is also expedient with a view to theoretical investigation. The calculations of hydraulic losses by means of CFD simulations are connected to an enormous computational effort and require long calculation times. That is why only a very short time interval may be considered as part of the simulation and the parameters that affect the oil temperature or the oil viscosity must be predetermined.

The first step before the measurements is the run-in period. This run-in ends after 100,000 revolutions and is used for heating up the test rig. The adjustment of the operating temperature requires, in particular at low speeds, a selective heating of the oil. Higher speeds cause higher friction and amount of heat that dissipates into the oil. Consequently, operating conditions at higher speeds require cooling of the oil. To set the operating temperature without the use of an oil unit, a testing strategy which already proved effectively in [10] was chosen. For heating or cooling the oil and setting the oil viscosity different speed steps are driven successively. This way at low speeds the oil is always heated over the needed temperature and the operating point can be measured during the cooling phase. At higher speeds the oil is always cooled below the needed temperature and measurement is carried out during the heating (see Fig. 5). This procedure is repeated several times to provide a higher statistical certainty.

The experimental determination of the drag and churning losses is enabled by varying the oil level. This requires tests with a minimum amount of oil. The friction torque which is determined in this way provides the reference for assessing the drag and churning losses.

Due to the forming of a lubricating film, the different lubrication states must be comparable. So it is not possible to do tests without lubrication at all. To reproduce the condition of the forming of a lubricating film in experiment the test bearing is oil

jet lubricated. Fig. 6 shows that the lubrication occurs not continuous but stepwise. Between these steps the friction torque decreases, this effect is known as starvation. It decreases until the next oil injection occurs. For each measurement point the same oil volume of 1 ml is injected. Those maxima represent the reference oil level which are used to determine the hydraulic losses. In order to provide uniform operating conditions as described above, the injected oil is heated up to $T = 60$ °C.

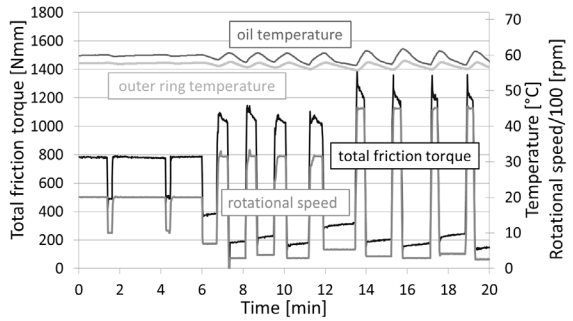

Fig. 5. *Adjustment of operating temperature*

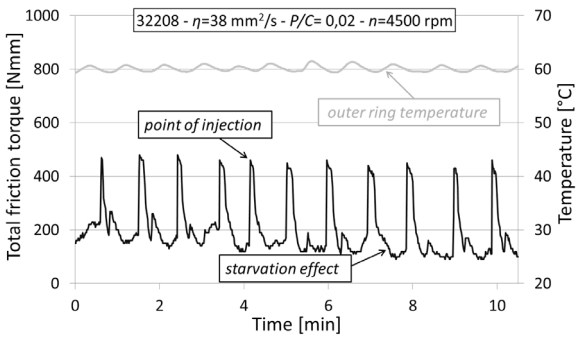

Fig. 6. *Effect of the oil jet lubrication on the total friction torque*

The temperature of the outer ring in oil bath lubrication test bearing corresponds to the oil temperature, like shown in Fig. 5. For this reason the outer ring is heated up with hot air to an appropriate temperature level (58 °C ≤ T_{oil} ≤ 60 °C) before injection of the oil. According to rolling bearing manufacturer information the temperature of the inner ring is usually about 5 °C ≤ T_{ir} ≤ 10 °C higher than the outer ring temperature **[11]**. This temperature was not measured in the experiment. Due to this the operating conditions are only adjusted by the heating up of the outer ring.

The lubrication of the supporting bearing is carried out periodically to avoid damage. It is oil jet lubricated. At the time of lubrication there is a short-time increase in the total friction torque after that it drops to a constant value so that the measurement is not affected by the lubrication of the test bearing.

1.3 Simulation

Hydraulic losses in roller bearings can be divided in two main components. The first one is caused by the movement of the rolling elements and the cage in the lubricant. It results from the shear stress τ by the lubricant friction and the compressive stress p on the rolling elements. Those stresses are exerted contrary to the rolling direction of the rolling elements and form the drag torque which depends on the bearing diameter. This drag torque corresponds to the drag losses. The second component of the hydraulic losses is the churning torque. This is mainly caused by the shearing of the oil at the bearing surfaces during dipping into the oil bath. Those surfaces are rolling elements end, cage surface, cage ends, cage pockets and lips **[12]**. This churning torque corresponds to the churning losses.

To solve fluid mechanical tasks calculation tools are required. One way to calculate the hydraulic losses are CFD simulations **[13]**. The solution for complex flow distributions inside a bearing is based on the volume-of-fluid method (VOF). The main problem here is the flow area, which is three-dimensional, unsteady and two-phase. This means oil and air have to be considered. For simulation of flow CFX software packages with integrated modules for the modelling and evaluation of results are used. For flow calculation a 3-D contour adapted computational grid is used. The free flow area in the test bearing and the shaft are considered in the grid. To provide a high calculation accuracy hexahedron grid cells are used. For modeling the motion of the rolling bearing elements a Frame Change Model is applied which is known as transient rotor stator (TRS). This solution provides accurate models to describe the motion between moving and stationary domains. The disadvantage of this method is that large computer resources are required. The applied model considers the rotation of the rolling elements around its own axis and also the rotation around the symmetry axis of the bearing at the same time. It also considers the different speeds between the rolling elements including cage and inner ring. The outer ring is modeled as the stationary domain.

The computational grid of the simulation model and its size influence the quality of the calculation results and also the computational time. Fig. 8 shows the three-dimensional computational grid of the entire model which is used for the simulation. That computational grid has approximately 2.5 million

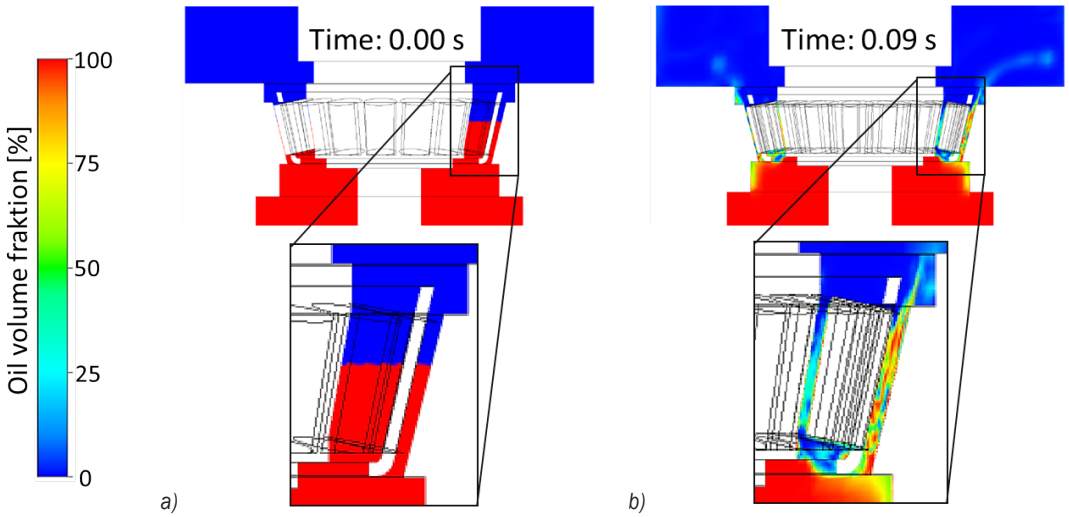

Fig. 7. *Instantaneous oil volume fraction in a tapered roller bearing at a) 0 s and b) 0.09 s*

cells. For a precise calculation of the flow inside the tapered roller bearing the grid in this area is much finer than the grid in the space below and above the test bearing.

When evaluating the CFD simulation a two-dimensional visualization of the oil distribution in the test bearing is available. With this visualization, information on flow phenomena may be obtained. Fig. 7 shows an example of the oil distribution in the cross section of the simulation model for the tapered roller bearing in a half-flooded test bearing. In the figure two discrete time points are presented. The figures provide information on the oil flow caused by the rotation of the tapered roller bearing. The oil is displaced within a very short timeframe by the interaction of the rolling elements, the cage and the internal geometry of the tapered roller bearing in the testing room above the test bearing.

2 EXPERIMENTAL AND SIMULATION RESULTS

2.1 Influence of the Oil Level and Viscosity

Fig. 9 illustrates the influence of the oil level on the hydraulic losses of tested tapered roller bearing 32208 at a constant operating temperature of T = 60 °C. The results for a fully-flooded (h = 3 b) and a half-flooded (h = 0.5 b) test bearing for both test oils are presented. As expected Oil 1 causes higher hydraulic losses, due to its higher viscosity. The rise of rotational speed effects a faster displacement of the lubricant and results in higher losses as well. Consequently, the speed is a significant parameter for reducing the losses. The influence of the oil bath level is also

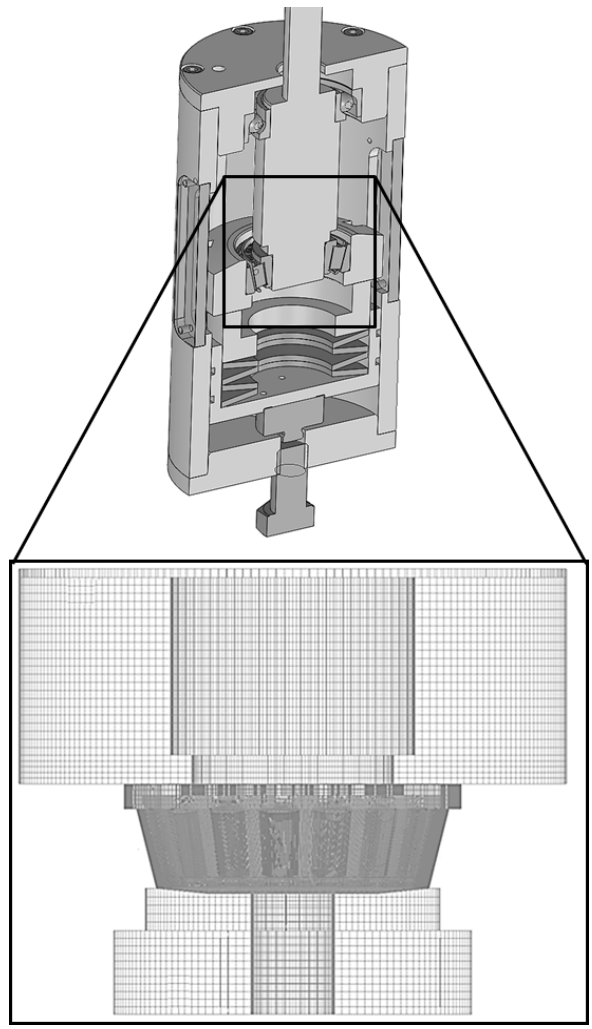

Fig. 8. *Mesh modelling of tapered roller bearing for CFD-simulation of drag and churning losses*

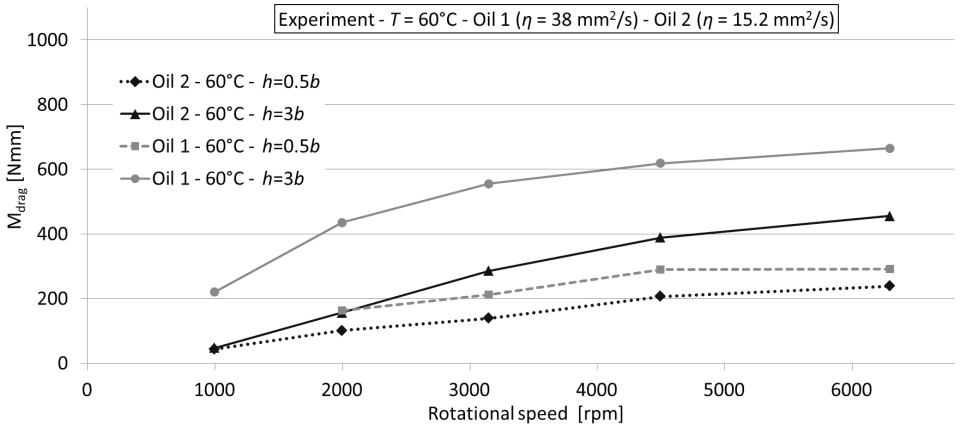

Fig. 9. *Influence of the oil level and rotation speed on the hydraulic losses of a tapered roller bearing 32208 (operating temperature, T=60 °C)*

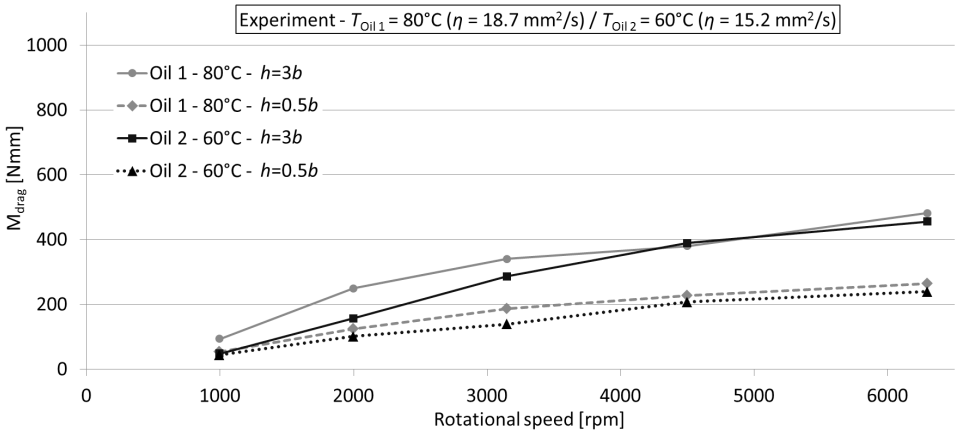

Fig. 10. *Comparison of test oils at a similar operating point with a view to viscosity (hydraulic losses of a tapered roller bearing 32208)*

explicit. Especially the results from experiment with Oil 1 present the clear difference of lubricant losses. To get a similar viscosity of the test oils different operating temperatures were set up. Oil 2 was heated up to $T_{Oil2} = 60$ °C, Oil 1 to $T_{Oil1} = 80$ °C. That way the kinematic viscosity were reduced to $\eta = 18.7$ mm²/s for Oil 1 and $\eta = 15.2$ mm²/s for Oil 2. Fig. 10 illustrates that the hydraulic losses (drag and churning losses) are similar in size when specifying an insignificant viscosity difference. Those results are showing the drag and churning losses are independent of the oil but depend on the viscosity.

The advantage of the CFD simulation in comparison to the experiment is the opportunity to consider the elements of the test bearing with regard to drag and churning losses individually. Table 1 shows the assignment of the losses to the elements of the test bearing. The results make clear that the main part of the losses is caused by the rolling elements, outer and inner ring. In case of rolling elements the pressure on

Table 1. *Subdivision of drag and churning losses in tapered roller bearing 32208 for different rotational speeds in %*

Rolling bearing element	Classification	2000 [rpm]	4500 [rpm]	6300 [rpm]
Rolling elements-raceway	inertial	45.11	45.40	45.00
Rolling elements-raceway	viscous	9.09	9.10	8.90
Rolling elements-face	viscous	0.54	0.55	0.61
Cage	viscous	0.73	0.95	0.92
Inner & Outer ring	viscous	36.43	37.53	37.39

the raceway due to density (drag losses) causes much higher losses than the shear stress of the lubricant (churning losses). The rest of the hydraulic losses which are not mentioned in Table 1 arise outside of the tapered roller bearing.

2.2 Influence of the Inner Geometry

To investigate the influence of the inner geometry of the bearing on the hydraulic losses experiments with a second tapered roller bearing 32208 produced by another manufacturer were carried out. The cone angle and the number of rolling elements of both bearings are identical. Because of standardization the size and the geometry of inner and outer ring are also the same. The only difference between the test bearings is the length of the rolling elements and consequently the length of the cage. The differences are presented in Table 2.

Table 2. *Main parameters of the test bearings*

Test bearing	1	2
Length rol. elements [mm]	≈16	≈17
Length cage [mm]	≈22	≈23
Number of rol. elements	17	17

Fig. 11 illustrates the experimental results. The losses which have been measured on the test bearings have a similar size. In this case geometric differences influence the losses insignificantly. However at higher speed levels the differences such as larger surface area from rolling elements and a longer cage become noticeable because test bearing 2 causes higher drag and churning losses. But in this case the accuracy of the sensor must also be considered with regard to the results.

2.3 Simulation Results and Comparison

The experiments are used to validate the simulation model, presented in Chapter 1.3. Fig. 12 illustrates a comparison of simulation and calculation results. The latter is provided by the SKF-model to calculate the drag and churning losses. The calculation requires only the kinematic viscosity at the operating temperature to consider the lubricant. In opposite to the simulation there is no possibility to consider the changing density. Due to this fact a single-phase simulation was performed to determine drag and churning losses for oil level $h_{oil} = 3b$. In Fig. 12 results of simulation and calculation of a half-flooded ($h_{oil} = 0.5b$) and a fully-flooded ($h_{oil} = 3b$) tapered roller bearing 32208 at operating temperature of 60 °C are compared. There is a difference between calculated and simulated results for the higher oil bath level. One explanation is the factor which considers vertical shaft orientation. In the case of an oil bath level $h_{oil} \geq 1b$ it always amounts to 1. For the low oil bath level the correlation between calculation and simulation is much better.

The shaft rotation induces a two phase mixture of oil and air and the air volume rises with rotational speed. This effect can be considered in a single-phase simulation by changing the dynamic viscosity. In general liquid and gas can be observed as a fluid [14]. Its properties correspond to the parts by volume of both components:

$$\mu = \mu_f c + \mu_g (1 - c). \quad (1)$$

The factors c und μ represent the volume share and the dynamic viscosity at the operating point. Indices f and g stand for fluid (lubricant) and gas (air). Volume share c can be calculated with Eq. (2) by using the densities ρ_f and ρ_g of oil and air.

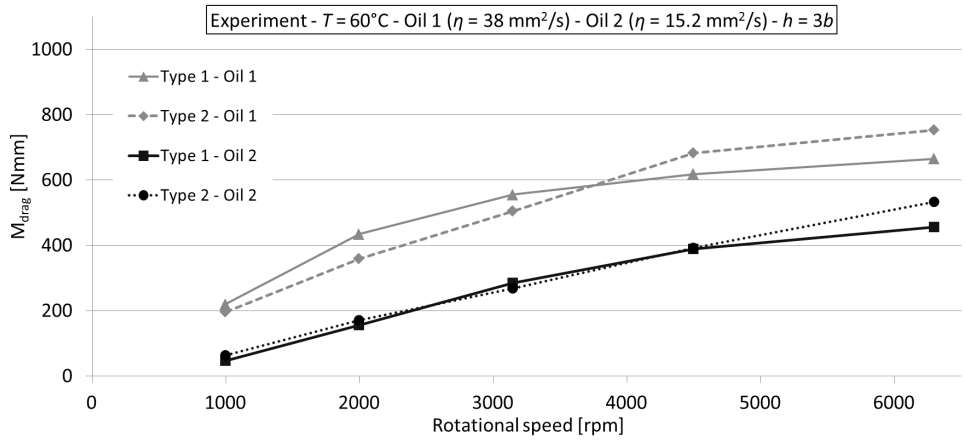

Fig. 11. *Influence of the inner geometry on the drag and churning losses*

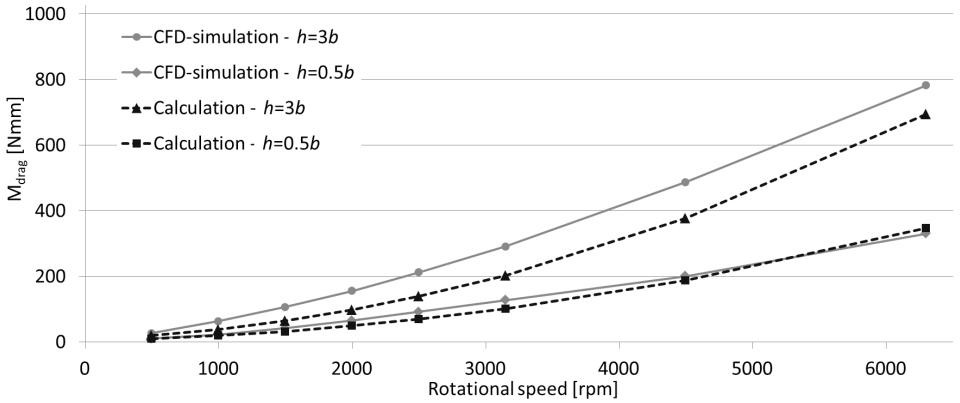

Fig. 12. *Comparison of CFD-simulation and calculation results (SKF-model)*

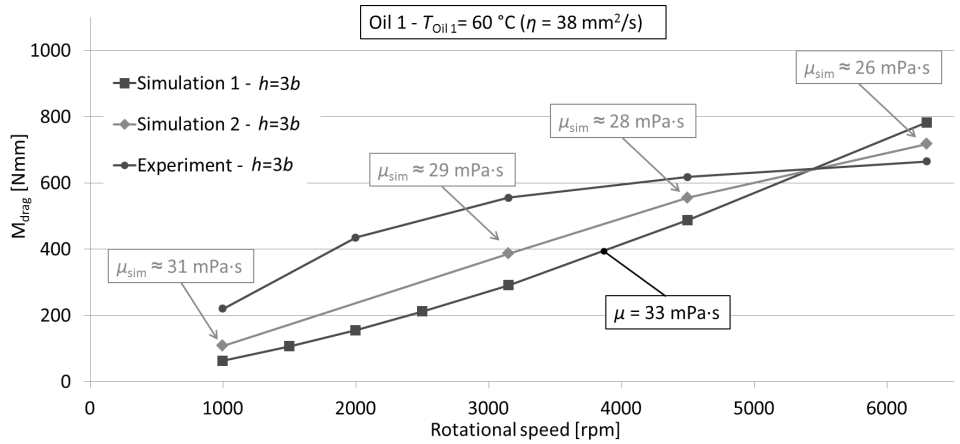

Fig. 13. *Influence of the foaming of oil on the dynamic viscosity and simulation results*

$$\rho = \rho_f c + \rho_g (1-c). \tag{2}$$

For this purpose, the changes in the weight of a defined oil volume at different speeds have to be measured. The approximation of air density may stay disregarded, as well as the dynamic viscosity in Eq. (1). Multiplication of the volume share with the dynamic viscosity provides the modified dynamic viscosity for the simulation. The shares of the dynamic viscosity which are used in simulation to consider the foaming of oil are shown in Table 3.

Fig. 13 presents the simulation results using dynamic viscosities considering the foaming of oil. They are compared to the simulation results already presented in Fig. 12 and experimental results. The hydraulic losses which have been calculated by considering the modified viscosity more accurately conform to the experimental results. Especially the curve progression has changed to a better fit. Its tendency corresponds to the curve progression of the experimental values. The differences between simulation and experiment may be caused by the way of determining the dynamic viscosity.

Table 3. *Viscosity of test Oil 1 in consideration of air content (Volume Oil ≈ 24 ml, Weight ≈ 20.8 g, T_{Oil} = 60 °C, η = 38 mm²/s)*

Speed [rpm]	Δ Weight Oil [g]	Viscosity share [%]
0	0	100
1000	–0.93	95
2000	–1.68	92
3150	–2.38	88
4500	–3.14	84
6300	–4.16	80

Further simulation results are provided in Fig. 14. It represents simulation and experimental results with test Oil 2. As shown in the figure the experiment corresponds to the simulation. The differences between measured and calculated losses are insignificant. These simulations consider the foaming of the oil as well as the simulations with test Oil 1 (Table 4).

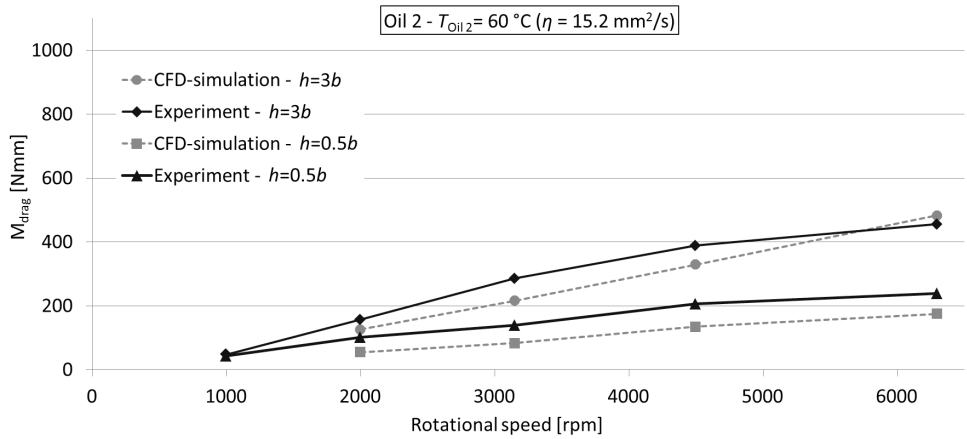

Fig. 14. *Comparison of experimental and simulation results for test Oil 2*

Table 4. *Viscosity of test Oil 2 in consideration of air content (Volume Oil ≈ 24 ml, Weight ≈ 20.7 g, T_{Oil} = 60 °C, η = 15.2 mm²/s)*

Speed [rpm]	Δ Weight Oil [g]	Viscosity share [%]
0	0	100
1000	-1.37	93
2000	-2.35	89
3150	-3.41	84
4500	-4.03	81
6300	-4.62	78

3 CONCLUSION

The first results presented in this paper give an overview on the experimental and theoretical investigations of drag and churning losses in tapered roller bearings. They clearly indicate that rotational speed, oil viscosity and especially the oil level affect the drag and churning losses of this bearing type significantly. Furthermore CFD-simulations illustrate the accuracy of available methods to calculate the drag and churning losses. Simulations considering modified dynamic viscosity caused by oil foaming correspond better to experiment. Even the tendency of curve progression is approximated. For better results enhanced viscosity measurement needs to be implemented.

Next steps will be to compile a generally accepted analytical model to calculate the drag and churning losses. This model will include tapered roller bearings with a vertical shaft. Also experiments and simulations with other bearing types, such as deep groove ball bearings and angular contact ball bearings will be carried out. Furthermore it is possible to influence the air content in the lubricant by the use of antifoam additives (foam inhibitors). To investigate the effects of such additives with regard to drag and churning losses further experiments are planned.

4 ACKNOWLEDGMENT

The results presented in that paper are prepared in the framework of a project financed by the German Research Association (DFG-SA898/12-1 and DFG-SCHW826/9-1).

5 REFERENCES

[1] Pradeep, K.G. (1984). *Advanced Dynamics of Rolling Elements*. Springer-Verlag, New York.

[2] Koryciak, J. (2007). *Einfluss der Ölmenge auf das Reibmoment von Wälzlagern mit Linienberührung*. PhD Thesis. Lehrstuhl für Konstruktionstechnik der Ruhr-Universität Bochum, Bochum.

[3] Aul, V., Kiekbusch, T., Marquart, M., Sauer, B. (2010). *Experimentelle und Simulative Ermittlung von Reibmomenten in Wälzlagern*. Fachtagung der Gesellschaft für Tribologie und Schmierung, Göttingen, 2010, S. 30/1-17.

[4] Aul, V., Kiekbusch, T., Marquart, M., Sauer, B. (2011). *Experimentelle und simulative Ermittlung von Reibmomenten in Wälzlagern bei Minimalmengenschmierung*. Fachtagung der Gesellschaft für Tribologie und Schmierung Göttingen, 2011, S. 51/1-16

[5] SKF Gruppe. Wälzlager. *Wälzlager-Katalog*. PUB BU/P1 10000/2 DE. 2014, S. 99-114.

[6] Becker, D., Schwarze, H., Brenner, G. (2009). *Verbesserte Simulation der Reibungs- und Verschleissverhältnisse hochbelasteter Tribosysteme*. ATZ / MTZ - Konferenz Reibungsminimierung, Esslingen.

[7] Brenner, G., Al-Zoubi, A., Mukinovic, M., Schwarze, H., Swoboda, S. (2007). Numerical simulation of surface roughness effects in laminar lubrication using the Lattice-Boltzmann method. *Journal of Tribology*, vol. 129, no. 3, p. 603-610, **DOI:10.1115/1.2736452**.

[8] Leibensperger, R.L. (1972). Analysis of the flow of oil through a tapered roller bearing. *Journal of Lubrication Technologie*, vol. 94 no. 2, p. 125-130, **DOI:10.1115/1.3451652**.

[9] Kazutoshi, T., Masamichi, S., Teruo, H. (1997). Observation of lubricating oil behavior in internal free space of tapered roller bearing. *Japanese Journal of Tribology*, vol. 42, no. 4, p. 491-496.

[10] Liebrecht, J., Si, X., Sauer, B., Schwarze, H. (2014). *Untersuchungen von hydraulischen Verlusten an Kegelrollenlagern.* Fachtagung der Gesellschaft für Tribologie und Schmierung, Göttingen, 2014, S. 22/1-11.

[11] Schaeffler Technologies AG&Co. KG. *Wälzlager.* Wälzlager-Katalog. August, 2012, S. 110.

[12] Concli, F., Gorla, C. (2012). Computational and experimental analysis of the churning power losses in an industrial planetary speed reducers. *WIT Transactions on Engineering, Sciences,* vol. 74, p. 287-298, **DOI:10.2495/afm120261**.

[13] Seebode, F. (2011). *Axialer Ölfluss durch Wälzlagerungen.* PhD Thesis. Institut für Tribologie und Energiewandlungsmaschinen. TU Clausthal, Clausthal.

[14] Ferziger, H., Peric, M. (2008). Strömungen mit freien Oberflächen. *Nummerische Strömungsmechanik*. Springer-Verlag Berlin Heidelberg. p. 463-468.

Strojniški vestnik - Journal of Mechanical Engineering 61(2015)6, 409-418
DOI:10.5545/sv-jme.2015.2460
Original Scientific Paper
Received for review: 2015-01-20
Received revised form: 2015-04-02
Accepted for publication: 2015-04-22

Improvement of Electric Discharge Machining (EDM) Performance of Ti-6Al-4V Alloy with Added Graphite Powder to Dielectric

Emre Unses[1] – Can Cogun[2,*]

[1] TUBITAK Space Technologies Research Institute, Turkey
[2] Cankaya University, Faculty of Engineering, Mechatronics Engineering Department, Turkey

Ti-6Al-4V is a well-known Ti alloy widely used in the aerospace industry and belongs to the group of difficult-to-machine materials. It is less suitable for both conventional chip removal (machining) techniques and electric discharge machining (EDM). The very low material removal rate (MRR) of the Ti alloys during the EDM process causes prohibitively long machining durations. The goal of this study was to improve the EDM performance of the Ti-6Al-4V alloy by the addition of graphite powder into the kerosene dielectric liquid. The EDM performance was quantified by MRR, tool electrode wear rate (EWR), relative wear (RW), surface roughness and texture properties. The experiments conducted have shown that the use of graphite powder mixed with the kerosene dielectric (GPMKD) during machining considerably increases the MRR, improves the R_a and $R_{z(DIN)}$ surface roughness and decreases the RW. 3D topographic views of the machined workpiece surfaces attained with GPMKD revealed uniformly distributed surface valleys and peaks over the surface and peaks with short and round tops since the discharge energy of a spark is distributed over a large area at the machining gap. The experimental results strongly indicate the adaptability of the proposed technique to EDM die sinking and EDM drilling applications of the Ti-6Al-4V alloy in the aerospace industry. The ED machining performance of Ti-6Al-4V alloy using GPMKD is also compared to that of AISI 1040 steel, which is commonly used in EDM applications.

Key words: electric discharge machining (EDM), Ti-6Al-4V, graphite powder, material removal, tool electrode wear, roughness, 3D surface topography

Highlights

- *The use of graphite powder mixed kerosene dielectric (GPMKD) in Ti-6Al-4V machining increases the material removal rate (MRR).*
- *GPMKD use resulted in lower peak-to-valley heights than the kerosene dielectric considering surface topographies.*
- *The machined surfaces were free of carbon contamination in the GPMKD experiments.*
- *Graphite powder used in this study is much cheaper than other metallic and non-metallic powders used in the literature.*

0 INTRODUCTION

Electric discharge machining (EDM) is one of the non-traditional machining methods that is commonly used to produce die cavities by the erosive effect of electrical discharges. The success of EDM is associated with its capability of machining workpieces of high hardness and complex shapes that cannot be machined by conventional chip removal methods. This method is especially effective in machining hard die steels, complex cavities and small workpieces.

Ti-6Al-4V is a well-known Ti alloy widely used in the aerospace industry in jet engines, particularly in the disk and fan blade components of the compressor. Ti-6Al-4V has a 7 to 10 times higher electrical resistance, a 7 to 8 times lower heat conductivity and a 10 % to 15 % higher melting temperature than the AISI 1040 steel which is widely used in the production of machine elements and die applications. Ti-6Al-4V belongs to the group of difficult-to-cut materials in traditional machining. The two main problems in the traditional machining of Ti-6Al-4V are as follows:

a) The heat generated during cutting action cannot be easily dissipated since Ti-6Al-4V is a poor heat conductor. The heat is concentrated on the cutting edge causing very short tool life.
b) The Ti-6Al-4V has a strong alloying tendency with cutting tool materials causing palling, welding and smearing on tool surface especially at high cutting temperatures.

For these reasons, cutting is performed at low cutting speeds to ensure a reasonable tool life. The economical machining rates of the Ti-6Al-4V vary between 20 mm^3/min and 8000 mm^3/min depending on machining operations, cutting tool characteristics, feed rates, cutting speeds and depth of cuts. The EDM of Ti alloys is also difficult as compared to Ni based super alloys due to high electrical resistivity (low electrical conductivity). During EDM of Ti-6Al-4V, a low level of current flows through the machining gap due to the high electrical resistance of the workpiece material [1]. Moreover, the locally increased temperature due to electrical discharges on the Ti alloy surface increases the electrical resistance of the

*Corr. Author's Address: Mechatronics Engineering Deptartment, Cankaya University, Ankara, Turkey, cogun@cankaya.edu.tr

material [2]. The low heat conductivity of the material also prevents the transfer of plasma channel heat to the work surface thus causing smaller surface craters. Both facts reduce the machinability and material removal rate (MRR) of the material significantly. Asokan et al. [1] used EDM for drilling holes in Ti-6Al-4V with a Cu tool electrode and deionized water dielectric. They concluded that the current, pulse time (pulse on time) t_s, pause time (pulse off time) t_p and capacitance affected the MRR and the dimensional accuracy. Soni and Chakraverti [3] experimentally investigated the effects of discharge current i_d and tool electrode rotational speed (0 rpm to 1000 rpm) on MRR, tool electrode wear rate (EWR) and average surface roughness (R_a) of the Ti alloy using commercial grade kerosene without a powder addition. They found that the increasing rotational speed of the Cu-W tool electrode improved the MRR, but increased the EWR and R_a. Chen et al. [4] investigated the effects of deionized water and kerosene dielectric on machining performance of the Ti-6Al-4V alloy using a Cu tool electrode. The study revealed that the deionized water resulted in higher MRR and lower EWR than the kerosene. The lower MRR with the kerosene dielectric was attributed to: i) the formation of a TiC layer on the workpiece surface which has higher melting temperature than the workpiece material, ii) the formation of a C layer on the tool electrode surface causing passivation of electric discharge phenomena. Mhatre et al. [5] experimentally investigated the electric discharge drilling characteristics of Ti-6Al-4V using a commercial EDM dielectric IPOL. The i_d is found to be the most significant parameter affecting the MRR, the dimensional accuracy and the surface integrity of the drilled hole. They also claimed that increasing the i_d and the pulse voltage increases the MRR to a certain extent and decreases the EWR, while increasing t_s causes a reduction in the EWR.

Numerous research studies have shown that using a powder mixed dielectric EDM (P-EDM) process can improve the surface roughness, increase MRR, and reduce EWR and relative wear (RW=EWR/MRR). Addition of electrical conductive powder into the dielectric leads to a bridging effect and reduces the insulating strength of the dielectric fluid, thus forming a discharge channel more easily [3] and [6]. The bridging phenomena results in the multisplitting of one discharge occurrence over a larger area in the machining gap during a pulse cycle time. Thus, the energy of a pulse is shared across multiple discharges (with less energy), which form shallow and large diameter craters on the surface. These craters result in a better surface roughness and lower peak-to-valley heights in the machined surface profiles. In one of the earlier studies in the field, Jeswani [7] investigated the effects of adding 4 g/l graphite powder into the kerosene dielectric during machining of mild steel with a copper tool electrode. An increase in MRR and a decrease in EWR and RW were reported. Uno and Okada [8] and Uno et al. [9] mixed Si and Ni powder into the dielectric to coat the Al-bronze die surface. The increasing Ni powder concentration (C_p) resulted in smaller crater dimensions and a thicker re-solidified layer on the die surface alloyed with Ni. They also obtained a hard TiC layer on the tool steel surface by using a Ti tool electrode and graphite mixed kerosene under reverse electrode polarity (to increase the wear of Ti tool electrode). Ming and He [10] stated that the addition of conductive and inorganic-oxide powders into kerosene decreases the ionization voltage of the dielectric and increases the machining gap. Cogun et al. [11] experimentally studied the effects of adding graphite and non-conductive boric acid powder into kerosene on MRR, EWR, RW, R_a and surface hardness for the Cu tool electrode-steel workpiece pair. The graphite powder C_p and the t_s were the two machining parameters found to strongly effect MRR and EWR. Furutani et al. [12] mixed Ti powder into the dielectric to form a thick TiC layer on metal surfaces using small Cu wire or rotating disc electrodes. They realized that the higher Ti powder C_p resulted in harder TiC coatings. In Prihandana et al. [13], the silver-tungsten workpiece was micro-drilled (holes with 300 μm and 500 μm depth) with a tungsten tool electrode at 10 g/l graphite powder C_p in the kerosene. They reported a five times higher MRR than for pure kerosene. Reddy et al. [14] investigated the machining characteristics of a PH17-4 stainless steel workpiece using surfactant (non-ionic SPAN20) and graphite mixed commercial EDM oil. They claimed an increase in electric conductivity of the dielectric fluid with increasing concentration of the surfactant. The maximum MRR has been achieved at 6 g/l surfactant and 4.5 g/l graphite powder concentration settings.

The literature survey reveals that little work has been carried out on the P-EDM of Ti-6Al-4V alloy. Lin et al. [15] used a hybrid process (EDM+USM (ultrasonic machining)) to machine the Ti-6Al-4V. The SiC powder added to deionized water and kerosene was used as a conductive powder in the dielectric for EDM and as an abrasive for the USM process. It is reported that increasing the SiC powder concentration up to 90 g/l improved the MRR significantly. On the other hand, a very high C_p resulted in the accumulation of excessive powder in the machining gap resulting in frequent arc pulses (undesirable) and low MRR.

The kerosene with SiC powder led to better surface roughness than the deionized water with SiC powder. Chow et al. [16] investigated the effects of Al and SiC powder additions to the kerosene dielectric on MRR, EWR, R_a and discharge voltage waveforms of the Ti-6Al-4V workpiece. It is reported that the MRR was increased and R_a was decreased for P-EDM cases. It was found that the SiC powder mixed kerosene resulted in a higher MRR than that of Al powder, whereas the lowest R_a was experienced in Al powder mixed cases. In another work of Chow et al. [17], the MRR and EWR performance of Ti-6Al-4V were tested for the deionized water dielectric with and without SiC powder addition by using a rotational copper disk tool electrode. The highest MRR and the lowest EWR were obtained when 25 g/l SiC powder is mixed with deionized water. However, better R_a and surface texture were reported for the SiC powder mixed cases compared to using the pure deionized water. Rival [18] experimentally investigated the effects of SiC powder addition (2 g/l to 6 g/l) into kerosene on MRR, EWR and R_a for a Ti-6Al-4V workpiece and Cu-W tool electrode. He found that the MRR and R_a values were higher with higher i_d for the powder mixed kerosene experiments. The lowest R_a was obtained at 2 g/l SiC powder concentration. In Yasar and Ekmekci [19], the effects on surface topography of the Ti-6Al-4V workpiece were investigated when SiC powder was added into deionized water and kerosene. In their experimental work, the SiC powder C_p, the powder particle size, t_s and i_d were determined as the key parameters affecting surface topography. Homogenous surface topographies with small surface craters were observed on workpiece surfaces machined with SiC added dielectrics.

1 PURPOSE OF THE STUDY

The literature survey revealed that a P-EDM study on the effect of a graphite powder mixed dielectric on machining performance of Ti-6Al-4V, an alloy seeing growing use in the aerospace industry, has not been reported on so far. The authors of this work believe from their past experience [11] that adding graphite powder to the dielectric can significantly improve specific machining performance outputs of Ti-6Al-4V alloy such as MRR, EWR, RW and surface roughness. Moreover, the proposed graphite powder in this study is ~70% cheaper than the cheapest metallic and non-metallic powders used in the literature (like SiC, Al, Ni). This makes the graphite powder economically attractive with respect to the others. Moreover, the lower density of the graphite powder (2.1 g/cm^3) than the other powders (ρ_{SiC}=3.2 g/cm^3, ρ_{Ni}=8.9 g/cm^3, ρ_{Al}=2.7 g/cm^3) makes the formation of a homogenous suspension of the powder in the dielectric easier (due to the same particle size distributions). Following these considerations, we study the effects of adding graphite powder to kerosene on the MRR, EWR, RW and machined workpiece surface characteristics ((R_a, $R_{z(DIN)}$ and surface topography) depending on t_s, i_d and the dielectric flushing pressure P_d.

2 EXPERIMENTAL SETUP AND METHODS

The electric discharge machine used in this investigation is FURKAN EDM M25 Model die sinking machine with EDM25A generator. The pulse generator is an iso-pulse type with 80 V open circuit voltage.

In the first group of experiments, the kerosene (KD) was used. In the second group of experiments, graphite powder smaller than 37 μm particle size was mixed into kerosene (graphite powder mixed kerosene dielectric, GPMKD). Both the KD and the GPMKD experiments were conducted in a self-made machining tank with 40 cm × 55 cm × 24 cm dimensions made of 1.5 mm thick stainless steel sheets (Fig. 1). In order to maintain a homogenous suspension of graphite powder in the tank during tests, a flush mixing was applied by means of two parallel spaced (at the two bottom sides of the tank) 12 mm diameter Cu pipes with 2.4 mm diameter holes on it. The dielectric was sucked from the bottom level of the tank by means of a pump. One of the two branches of the pump exit was directed to the Cu pipes for homogenous mixing of the powder. The other branch was directed towards the machining gap (side flushing) for flushing the machining debris away. A manometer and an adjustment vane were mounted to the flushing branch to set the flushing pressure.

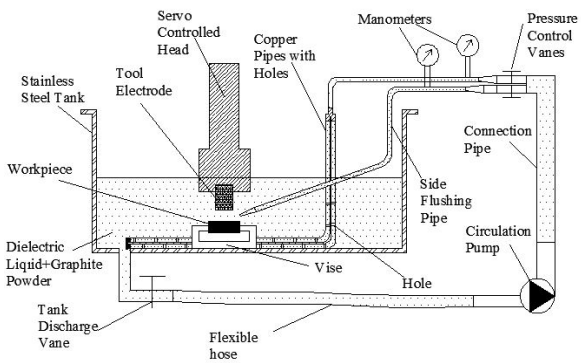

Fig. 1. *Experimental setup*

The graphite powder C_p to be used in the experiments was determined by a set of experiments conducted at t_s=100 µs, i_d=12 A, P_d=0.1 bar (Exp. 13) machining settings for C_p at 1 g/l, 3 g/l, 5 g/l, 10 g/l and 15 g/l. The machining duration was 70 minutes. Compared to the KD experiments (Fig. 2a and b), negligibly slight deviations in MRR and EWR values were observed at both 1 g/l and 3 g/l C_p values. At C_p=5 g/l, the MRR is almost doubled with respect to the KD. A very slight increase in MRR was observed at C_p=10 g/l and C_p=15 g/l (Fig. 2a) with respect to C_p=5 g/l. No significant difference in EWR values between KD and GPMKD with C_p=5 g/l was observed. However, the EWR increased noticeably for C_p=10 g/l and C_p=15 g/l (Fig. 2b). The R_a value was decreased with increasing C_p up to the 5 g/l level and no further improvement was observed above this particular level (Fig. 2c). Thus, C_p=5 g/l was selected as the level giving the best machining performance outputs among the tested C_p levels. In the literature, the elevated MRR values of various grades of steel and silver-tungsten workpieces with a range of 4 g/l to10 g/l graphite powder C_p in the kerosene [7], [11] and [13] and at 4.5 g/l graphite powder + 6 g/l surfactant concentration in the EDM oil [14] were also reported.

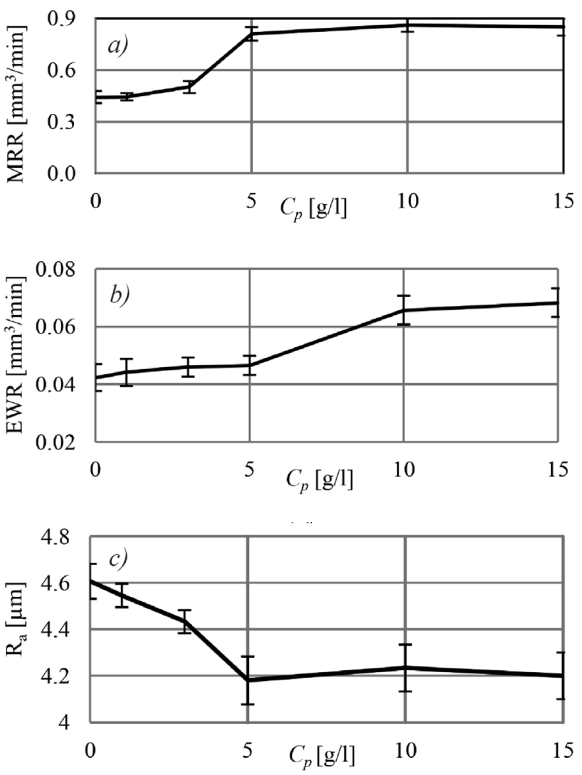

Fig. 2. *The effect of C_p on: a)* MRR, *b)* EWR *and c)* R_a

In the experiments, the workpiece material used was a Ti-6Al-4V Grade 5 alloy (90% Ti, 5.9% Al, 4% Va, 0.07% Fe, 0.02% C). The physical, mechanical, electrical and thermal properties of the alloy are given in Table 1. The workpieces were cut from a 30 mm diameter bar at 6 mm lengths. The bottom and top circular surfaces were finished using a fine emery paper. The workpieces were cut-off at their plane of symmetry to form two identical halves (Fig. 3). The two halves were contacted to each other to form a solid workpiece during experiments by using a simple vise. At the end of the machining, the separated halves facilitated easy surface roughness measurement since the mechanical contact stylus of the device should move along (traverse) the ED machined surface in horizontal. The same size of AISI 1040 steel (0.38% C, 0.6% Mn, 0.04% P, 0.05% S) workpieces (properties given in Table 1) were also prepared and ED machined to compare the MRR, EWR, R_a and RW values with that of Ti-6Al-4V. The electrolytic copper tool electrodes used in the experiments were in a cylindrical shape cut from a 14 mm diameter copper bar. The tool electrodes were 13 mm in diameter and 40 mm in length.

Table 1. *Properties of the Ti-6Al-4V alloy and the AISI 1040 steel*

Properties	Ti-6Al-4V [20]	AISI 1040
Density [g/cm³]	4.43	7.85
Brinell hardness [-]	334	163
Yield/ UT Strength [MPa]	1040/1080	361/585
Elasticity module [GPa]	113.8	200
Poisson ratio [-]	0.34	0.31
Electrical resistance [Ω·cm]	178e^{-6}	171e^{-7}
Spec. heat capacity [J/(kg·K)])	526	486
Heat conductivity [W/(m·K)]	6.7	50.7
Melting point [°C]	1604 to 1660	1400 to 1450

In this study, the preliminary experiments with t_s and i_d values lower than 50 µs and 6 A, respectively, indicated prohibitively long machining cycles. On the other hand, extremely poor surface roughness prevented us from using t_s and i_d values above 100 µs and 12 A, respectively. In the experiments, a long t_p (100 µs) was selected to allow more time for the removal of heat from the machining medium both via dielectric circulation (convective heat transfer) [21] and conductive heat transfer. The machining parameters and experimental design are given in Tables 2 and 3. Every experiment was repeated three times and the average of the measurements was used in the analysis. Error bars were also added to the graphical representation of the results to depict the

fluctuations in the measurements. Weight loss of the tool electrodes and workpieces were determined by taking initial and final (after machining) weights of the tool electrodes and workpieces using a HANA HG-1 type digital scale with 0.005 g accuracy. The weight losses were used to calculate the MRR, EWR and RW. Workpiece R_a and $R_{Z(DIN)}$ (average of the highest peak-to-valley measurements found for each cut-off length) measurements were performed using a portable Rank Taylor-Hobson Surtronic 3+ HB-103 stylus tracing instrument. The average of the measurements taken at six locations was used in the analysis.

The experiments were intentionally carried out using the arc control mode of the pulse generator at "medium suppression" level to observe the effects of machining parameters (i_d, t_s, P_d) and GPMKD on machining stability (regime). This setting level doesn't completely prevent the formation of arcs. However, we retracted the tool electrode in a timely manner (Table 2) to reduce the risk of tool electrode and workpiece surface damage due to arcing.

3D topographic views of the machined workpiece surfaces were generated by using a photometric stereo technique. A Point Grey Dragon Fly camera was used as the photographic capture system. The 2 mm × 2 mm surfaces were selected from the machined workpiece to obtain the topographic views. The 0.5 mm × 0.5 mm areas on the 2 mm × 2 mm views were magnified for closer examination of the surface characteristics. A Mitutoya MF176 toolmakers microscope was also used to examine the formed surface craters' characteristics.

Fig. 3. *A machined Ti-6Al-4V workpiece*

3 EXPERIMENTAL RESULTS AND DISCUSSION

3.1 Effect of GPMKD on MRR

The MRR increased with increasing t_s and P_d for both KD and GPMKD experiments (Fig. 4). The longer t_s resulted in a higher amount of energy transfer to the workpiece surface leading to higher amounts of work material removal by melting and evaporation phenomena [11]. For all machining settings, the MRR was increased by the use of GPMKD (Fig. 4), which was attributed to the following factors:

a) GPMKD reduces the electric resistance of the machining gap enabling high current (energy) flow through the gap and high amount of material removal from the workpiece craters [6].
b) The GPMKD widens the gap eliminating the difficulties in dielectric circulation and removal of debris in the machining medium, which in turn results in a higher number effective discharges [21] leading to higher MRR.

The second factor is more dominant in increasing MRR since Ti-6Al-4V has an extremely low thermal conductivity (proportional to the electrical conductivity) causing only small workpiece craters.

In this study, a 25 % to 104.3 % increase in Ti-6Al-4V MRR is achieved by using GPMKD for the machining settings used. In the literature, a 60 % to 500 % increase in MRR of non-Ti alloy workpieces (such as mild steel, 1040 steel and stainless steel) was reported when using GPMKD [7], [11] and [13]. Yet, only a 28.5 % to 60 % increase in Ti-6Al-4V MRR using Al or SiC powder mixed kerosene or deionized water was reported [15] to [17]. Therefore, the addition of graphite powder into kerosene resulted in a higher Ti-6Al-4V MRR than the addition of Al and SiC powders into the dielectrics.

Table 2. *Experimental settings*

Machining Parameter	Setting
Discharge current, i_d [A]	6, 12
Pulse (on) time, t_s [μs]	50, 100
Pause (pulse-off) time, t_p [μs]	100
Work duration [s]	1.6
Retraction duration [s]	0.8
Dielectric pressure, P_d [bar]	0.1, 0.4
Dielectric liquid	KD, GPMKD
Dielectric flushing type	side
Polarity	tool electrode (+)
Machining depth [mm]	0.7

3.2 Effect of GPMKD on Surface Roughness and Topography

Referring to Fig. 5, an increase in P_d does not lead to a significant difference in the values of R_a when comparing the KD and GPMKD experiments. It can also be seen that varying t_s has a smaller effect on R_a in the KD experiments. The higher P_d yielded a stable machining regime and less carbon accumulation on the surface. Destruction of the workpiece and tool electrode surface was observed in the KD experiments

when improper t_s and t_p values were selected for the used i_d values. The typical type of destruction was the lamination of the Cu tool electrode due to high temperatures generated in the gap, since Cu has lower melting temperature than the Ti-6Al-4V.

Table 3. *Experimental design*

Exp. no	Dielectric	t_s [μs]	i_d [A]	P_d [bar]
1	KD	50	12	0.1
2	KD	50	12	0.4
3	KD	50	6	0.1
4	KD	50	6	0.4
5	KD	100	12	0.1
6	KD	100	12	0.4
7	KD	100	6	0.1
8	KD	100	6	0.4
9	GPMKD	50	12	0.1
10	GPMKD	50	12	0.4
11	GPMKD	50	6	0.1
12	GPMKD	50	6	0.4
13	GPMKD	100	12	0.1
14	GPMKD	100	12	0.4
15	GPMKD	100	6	0.1
16	GPMKD	100	6	0.4

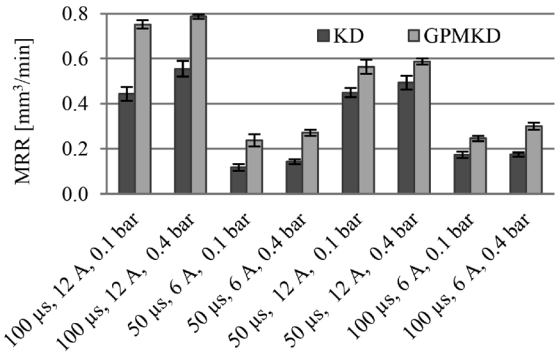

Fig. 4. *Effect of* GPMKD *on* MRR

The high temperature in the gap was due to poor heat conductivity of the Ti-6Al-4V workpiece [1]. The laminated tool electrode surface also causes deterioration of the workpiece surface. Accordingly, the GPMKD experiments resulted in lower R_a values (Fig. 5) and shinier surfaces compared to the KD experiments. The main reasons for this result are the enlarged heat discharge area forming large diameter and shallow craters [6], [11] and [16] and the accumulation of less carbon black (due to less frequent arc formations) on the surface.

In this study, a 2.4 % to 18.3 % decrease in R_a is observed by using GPMKD for the machining settings used. In the literature, a 5.4 % to 67 % decrease in R_a in machining of the 1040 steel workpiece by using GPMKD was reported [11]. However, R_a decreases of at most 25 % [15], 30.5 % [16], 35 % [17] and 27 % [18] have been reported in the machining of Ti-6Al-4V with kerosene+SiC powder, kerosene+Al powder, deionized water+SiC powder and kerosene+SiC powder mixtures, respectively. So, the R_a values measured in this study (3.8 mm to 4.7 mm) in the machining of Ti-6Al-4V with GPMKD are consistent with the reported findings in the literature (2.5 mm to 3.6 mm) for the same workpiece but for different dielectric and powder mixture combinations.

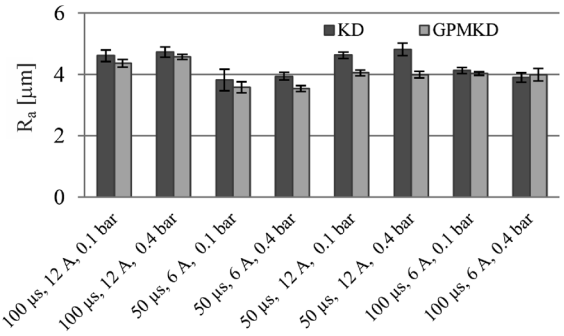

Fig. 5. *Effect of* GPMKD *on* R_a

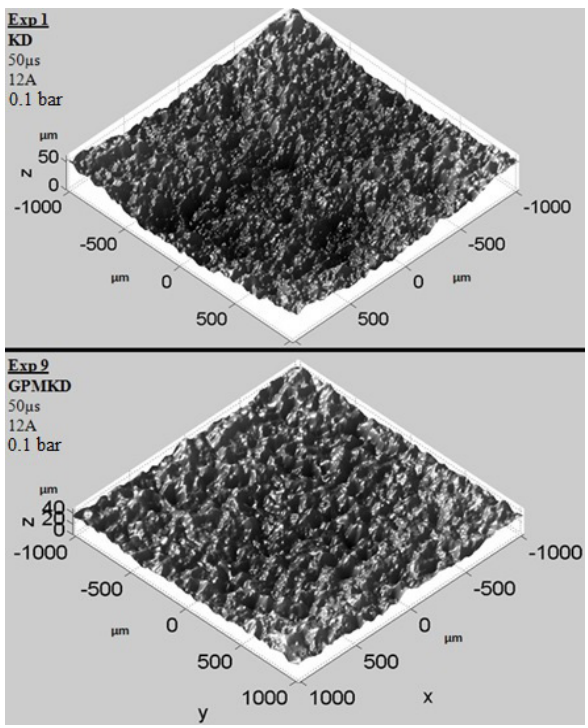

Fig. 6. *The 3D topographic views of the workpiece surfaces (Exp. 1 and 9)*

The average workpiece surface peak-to-valley heights of the KD experiments (~50 µm in Exp. 1 (Fig.

6a)) were decreased in GPMKD cases (~40 μm in Exp. 9 (Fig. 6b)). Uneven distribution of peaks and valleys was also observed in KD experiments due to frequent occurrences of undesirable arcs at the same spot. Magnified surface topography photographs revealed uniformly distributed short and round top peaks due to the uniform distribution of discharge energy in the gap in the GPMKD experiments. The surface topographies shown in Fig. 7 were formed by half of the energy discharges of Fig. 6 resulting in smaller craters and shorter peaks. In the GPMKD experiments, the z axis average height is decreased from ~40 μm to ~20 μm with respect to KD experiments. Roughness measurements revealed 4.8 % to 13.4 % reduction in $R_{Z(DIN)}$ values in GPMKD cases (Table 4). This reduction also verified the formation of shorter peaks (smaller peak-to-valley heights) through the use of the GPMKD.

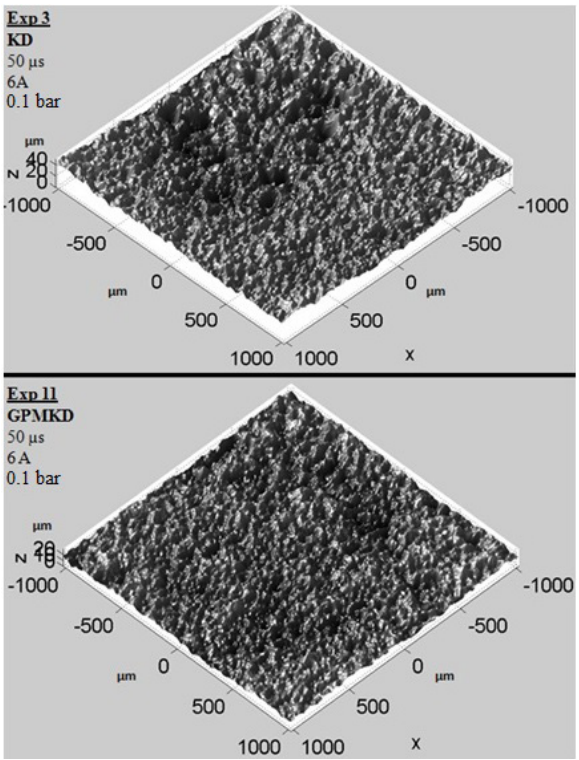

Fig. 7. *The 3D topographic views of the workpiece surfaces (Exp. 3 and 11)*

Table 4. $R_{z(DIN)}$ *measurements*

KD		GPMKD		Diff. [%]
Exp. no	$R_{z(DIN)}$ [μm]	Exp. no	$R_{z(DIN)}$ [μm]	
1	23.4	9	21.2	9.4
3	23.0	11	19.9	13.4
5	24.8	13	22.5	9.2
6	25.2	14	24.0	4.8

3.3 Effect of GPMKD on EWR and RW

Although it can be observed that EWR and RW increased with increasing values of P_d for both KD and GPMKD experiments, the EWR and RW values show significant variations depending on the values of t_s and i_d. The EWR and RW were decreased noticeably with increasing t_s (Figs. 8 and 9). The decrease in RW with increasing t_s was an expected result since the MRR increases and EWR decreases with increasing t_s. It was found that the i_d was the most significant machining parameter affecting machining performance outputs of Ti-6Al-4V. At high i_d settings, more electric current (energy) passing through the gap results in a large amount of workpiece and electrode material removal by melting and evaporation [11] and [22]. Due to this fact, the increased i_d resulted in higher R_a (Fig. 5), EWR (Fig. 8) and RW (Fig. 9).

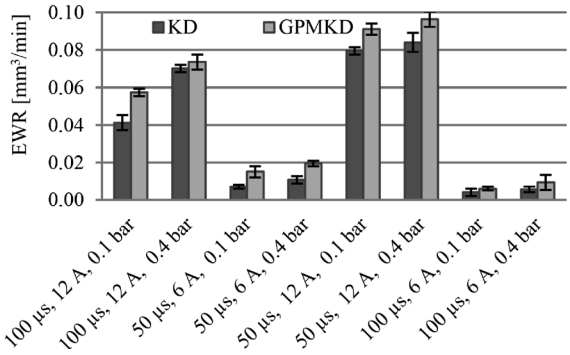

Fig. 8. *Effect of* GPMKD *on* EWR

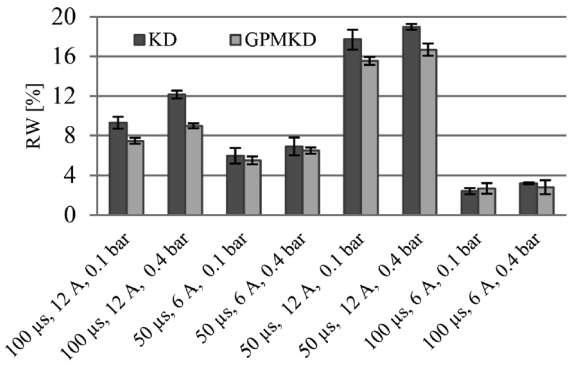

Fig. 9. *Effect of* GPMKD *on* RW

Slight increases in the EWR values were observed in the GPMKD compared to KD experiments (Fig. 8). This was attributed to big crater formations with the increasing electrical conductivity of the dielectric liquid in the GPMKD cases. In this study, a 4 % to 72 % increase in EWR was observed by using GPMKD for the tested machining settings. In machining of

Ti-6Al-4V with Al or SiC powder mixed kerosene or deionized water, a 150 % to 200 % [16], 57 % [17] and 105 % to 175 % [18] increase in EWR have been reported. Therefore, the increase in EWR observed in this study could be considered to be in reasonable agreement with other studies. On the other hand, a 15 % decrease in EWR was reported in machining of a mild steel workpiece with GPMKD at a low pulse discharge energy [7].

Fig. 9 clearly highlights the contribution of GPMKD use on the reduction of RW (7.7 % to 26 %). This is an important measure of long tool electrode life and economical machining.

3.4 Comparison of ED Machinability of AISI 1040 and Ti 6Al-4V Workpieces

The MRR of Ti-6Al-4V was 14.9 to 18.6 times slower than that of AISI 1040 for the KD experiments. Although the MRR was improved greatly by GPMKD use, the MRR of Ti-6Al-4V was still 11.9 to 13 times slower than that of AISI 1040 (Fig. 10). The RW values obtained in Ti-6Al-4V were 0.4 to 2.4 times higher than AISI 1040 in KD experiments. The GPMKD use reduced these values by ~20 % (Fig. 11). The lower electrical resistance and higher heat conductivity of the AISI 1040 than the Ti-6Al-4V led to larger diameter and deeper crater formations (evident from microscopic examinations) causing higher R_a values (Fig. 12).

4 CONCLUSION

This study is the first significant effort to use a graphite powder mixed dielectric to improve ED machining performance of the Ti-6Al-4V alloy in an EDM die sinking operation. The experimental results allow us to draw the following conclusions:

1) The increasing dielectric flushing pressure (P_d) improved the MRR significantly and increased the tool electrode wear rate (EWR) slightly for both the kerosene dielectric (KD) and the graphite powder mixed kerosene dielectric GPMKD cases. The R_a wasn't affected noticeably by the variation in P_d. Increasing t_s increased the MRR and decreased the EWR for KD and GPMKD. No changes in R_a were observed with the variation in t_s.
2) The machining was very stable and machined surfaces were free of carbon contamination in the GPMKD experiments, especially at high P_d settings.

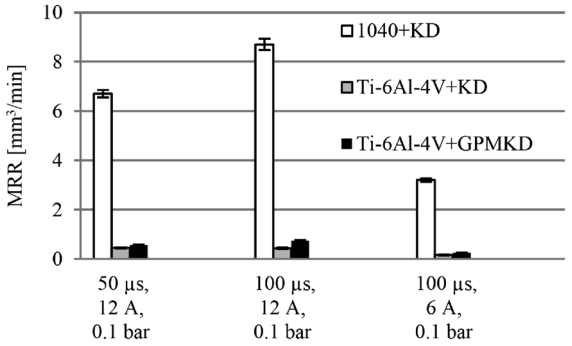

Fig. 10. *Comparison of* MRR *values of AISI 1040 and Ti-6Al-4V*

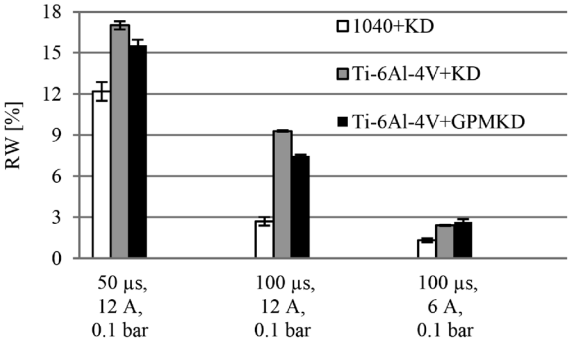

Fig. 11. *Comparison of* RW *values of AISI 1040 and Ti-6Al-4V*

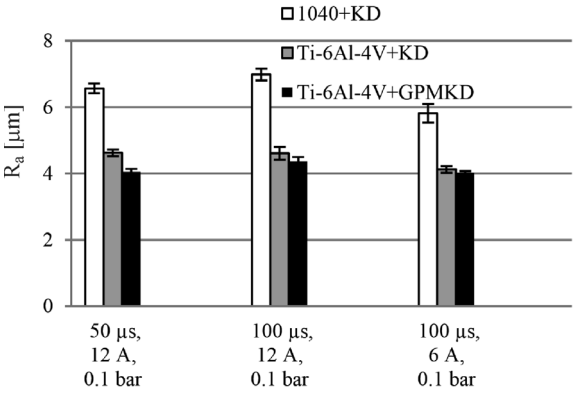

Fig. 12. *Comparison of* R_a *values of AISI 1040 and Ti-6Al-4V*

3) The GPMKD improved the MRR, R_a and RW of Ti-6Al-4V workpiece. The 3D surface topography of the machined surfaces revealed that the GPMKD use resulted in lower peak-to-valley heights than the KD experiments.
4) Although the use of GPMKD improved the MRR of the Ti-6Al-4V significantly, the MRR values with respect to the AISI 1040 steel workpiece were still low. However, much better R_a values in Ti-6Al-4V than in AISI 1040 were obtained with the use of KD and GPMKD.

Graphite powder is at least 70 % cheaper than other metallic and non-metallic powders used in the literature and is, thus, economically highly attractive. Moreover, the lower density of the graphite powder than the other powders provides a more homogenous suspension of the powder, which provides a stable ED machining regime. We also emphasize that the proposed graphite powder addition to the dielectric can be readily adapted to EDM die sinking and EDM drilling applications of Ti-6Al-4V in the aerospace industry considering the observed improvements in machining performance and lower costs.

5 NOMENCLATURE

MRR	Material removal rate [mm^3/min]
EWR	Tool electrode wear rate [mm^3/min]
RW	Relative wear (EWR/MRR) [%]
R_a	Average surface roughness [μm]
$R_{z(DIN)}$	Average of the highest peak to valley measurements found for each cut-off length [μm]
t_s	Pulse time (pulse on time) [μs]
t_p	Pause time (pulse off time) [μs]
i_d	Discharge current [A]
C_p	Powder concentration [g/l]
P_d	Dielectric flushing pressure [bar]

6 REFERENCES

[1] Asokan, T., Sudhakar, R.S., De Costa, P. (2000). Electrical discharge drilling of titanium alloys for aerospace applications. *Proceedings of the 19th AIMTDR Conference*, p. 161-165.

[2] Zhang, W.J., Reddy, B.V., Deevi, S.C. (2001). Physical properties of TiAl-base alloys. *Scripta Materialia*, vol. 45, no. 6, p. 645-651, **DOI:10.1016/S1359-6462(01)01075-2**.

[3] Soni, J.S., Chakraverti, G. (1994). Machining characteristics of titanium with rotary electro-discharge machining. *Wear*, vol. 171, no. 1-2, p. 51-58, **DOI:10.1016/0043-1648(94)90347-6**.

[4] Chen, S.L., Yan, B.H., Huang F.Y. (1999). Influence of kerosene and distilled water as dielectrics on the electric discharge machining characteristics of Ti-6Al-4V. *Journal of Materials Processing Technology*, vol. 87, no. 1-3, p. 107-111, **DOI:10.1016/S0924-0136(98)00340-9**.

[5] Mhatre, M.S., Sapkal, S.U., Pawade, R.S. (2014). Electro discharge machining characteristics of Ti-6Al-4V alloy: A grey relational optimization. *Procedia Materials Science*, vol. 5, p. 2014-2022, **DOI:10.1016/j.mspro.2014.07.534**.

[6] Zhao, W.S., Meng, Q.G., Wang, Z.L. (2002). The application of research on powder mixed EDM in rough machining. *Journal of Materials Processing Technology*, vol. 129, no. 1, p. 30-33, **DOI:10.1016/S0924-0136(02)00570-8**.

[7] Jeswani, M.L. (1981). Effect of the addition of graphite powder to kerosene used as the dielectric fluid electrical discharge machining. *Wear*, vol. 70, p. 133-139, **DOI:10.1016/0043-1648(81)90148-4**.

[8] Uno, Y., Okada, A. (1997). Surface generation in electrical discharge machining with silicon powder mixed fluid. *International Journal of Electrical Machining*, vol. 2, no. 1, p. 13-18.

[9] Uno, Y., Okada, A., Cetin, S. (2001). Surface modification of EDMed surface with powder mixed fluid. *2nd International Conference on Design and Production of Dies and Molds*, p. 86-92.

[10] Ming, Q.Y., He, L.Y. (1995). Powder-suspension dielectric fluid for EDM. *Journal of Materials Processing Technology*, vol. 52, no. 1-3, p. 44-54, **DOI:10.1016/0924-0136(94)01442-4**.

[11] Cogun, C., Ozerkan, H.B., Karacay, T. (2006). An experimental investigation on effect of powder mixed dielectric on machining performance in electric discharge machining (EDM). *Proceedings of the Institution of Mechanical Engineers, Part B: Journal of Engineering Manufacture*, vol. 14, no. 4, p. 202-212 **DOI:10.1243/09544054JEM320**.

[12] Furutani, K., Saneto, A., Takezawa, H., Mohri, N., Miyake, H. (2001). Accretion of titanium carbide by electrical discharge machining with powder suspended in working fluid. *Journal of the International Societies for Precision Engineering and Nanotechnology*, vol. l, no. 25, p. 138-144, **DOI:10.1016/S0141-6359(00)00068-4**.

[13] Prihandana, G.S., Sriani, T., Mahardika, M. (2012). Improvement of machining time in micro-EDM with workpiece vibration and graphite powder mixed in dielectric fluid. *Indian Journal of Engineering and Materials Sciences*, vol. 19, no. 6, p. 375-378.

[14] Reddy, V.V., Kumar, A., Valli, P.M., Reddy, C.S. (2015). Influence of surfactant and graphite powder concentration on electrical discharge machining of PH17-4 stainless steel. *Journal of the Brazilian Society of Mechanical Science and Engineering*, vol. 37, no. 2, p. 641-655, **DOI:10.1007/s40430-014-0193-4**.

[15] Lin, Y.C., Yan, B.H., Chang, Y.S. (2000). Machining characteristics of titanium alloy (Ti-6Al-4V) using a combination process of EDM with USM. *Journal of Materials Processing Technology*, vol. 104, no. 3, p. 171-177, **DOI:10.1016/S0924-0136(00)00539-2**.

[16] Chow, H.M., Yan, B.H., Huang, F.Y., Hung, J.C. (2000). Study of added powder in kerosene for the micro-slit machining of titanium alloy using electro-discharge machining. *Journal of Materials Processing Technology*, vol. 101, no. 1-3, p. 95-103, **DOI:10.1016/S0924-0136(99)00458-6**.

[17] Chow, H.M., Yan, L.D., Lin, C., Chen, C.F. (2008). The use of SiC powder in water as dielectric for micro-slit EDM Machining. *Journal of Materials Processing Technology*, vol. 195, no. 1-3, p. 160-170, **DOI:10.1016/j.jmatprotec.2007.04.130**.

[18] Rival, R. (2005). *Electrical Discharge Machining of Titanium Alloy Using Copper Tungsten Electrode with SiC Powder Suspension Dielectric*. MSc Thesis, University of Technology, Kuala Lumpur.

[19] Yasar, H., Ekmekci, B. (2014). Ti-6Al-4V surfaces in SiC mixed electric discharge machining. Advanced Materials Research, vol. 856, p. 226-230, **DOI:10.4028/www.scientific.net/AMR.856.226**.

[20] Fonda, P., Wang, Z., Yamazaki, K., Akutsu, Y. (2008). A fundamental study on Ti-6Al-4V's thermal and electrical properties and their relation to EDM productivity. *Journal of Materials Processing Technology*, vol. 202, no. 1-3, p. 583-589, **DOI:10.1016/j.jmatprotec.2007.09.060**.

[21] Cogun, C. (1990). A technique and its application for evaluation of materials contributions in electric discharge machining. *International Journal of Machine Tools and Manufacture*, vol. 30, no. 1, p. 19-31, **DOI:10.1016/0890-6955(90)90038-K**.

[22] Ozgedik, A., Cogun, C. (2006). An experimental investigation on tool wear in electric discharge machining. *International Journal of Advanced Manufacturing Technology*, vol. 27, no. 5-6, p. 488-500, **DOI:10.1007/s00170-004-2220-6**.

Vsebina

Strojniški vestnik - Journal of Mechanical Engineering
letnik 61, (2015), številka 6
Ljubljana, junij 2015
ISSN 0039-2480

Izhaja mesečno

Razširjeni povzetki

Strojniški vestnik - Journal of Mechanical Engineering 61(2015)6, SI 67

Prejeto v recenzijo: 2015-02-03
Prejeto popravljeno: 2015-04-14
Odobreno za objavo: 2015-05-06

Raziskava in analiza histereze potnega ventila za velike pretoke

Yaoyao Liao – Hongbing Yuan* – Zisheng Lian – Jiling Feng – Yongchang Guo
Kolidž za strojništvo, Tehniška univerza v Taiyuanu, Kitajska

V zadnjih letih je bilo odkritih več debelih premogovnih žil, ki zahtevajo hidravlično podporje na večjih globinah. Večji cilindri hidravličnega podporja pa delajo z večjimi pretoki in zato obstaja nujna potreba po hidravličnem sistemu za podporja s pretokom 1000 l/min, od tod pa potreba po zasnovi velikih potnih ventilov za omenjeni pretok. Pri preizkusu enokanalnega ventila na preizkuševališču za velike pretoke do 1000 l/min se je pokazala velika histereza pri izklopu, medtem ko so bili rezultati na manjšem preizkuševališču (do 16 l/min) dobri. Članek preučuje ta pojav histereze.

Problem histereze pri potnem ventilu za pretok 1000 l/min je bil raziskan s kombinacijo pristopa CDF in eksperimentalnega testa.

Za raziskave pretočnih lastnosti v ventilu je bila uporabljena simulacija po metodi CFD in ugotovljena je bila porazdelitev tlaka in neravnotežna sila na bat ventila. Potni ventil je bil nato optimiziran in njegove dinamične lastnosti so bile potrjene z eksperimentalnimi testi.

Konvencionalna enokanalna konstrukcija povzroča neenakomeren pritisk na bat. Radialna neravnotežna sila nastane predvsem na površini bata in na sosednji površini, ki ju oplakuje tekočina pod visokim tlakom. Radialna neravnotežna sila pri običajnih ventilih NS12 in NS23 je samo 15 N oz. 75 N in histereza tam zato ni opazna. S povečevanjem imenskega pretoka pa se povečajo tudi dimenzije ventila in površine, ki so izpostavljene neravnotežnemu pritisku. Radialna neravnotežna sila pri imenskem pretoku ventila NS25 je že 250 N in povzroča velike torne sile. Enokanalni ventil nima zadostne sposobnosti zapiranja in zato je bil zasnovan nov dvokanalni ventil. Radialna neravnotežna sila, ki deluje na dvokanalni ventil NS26, je v primerjavi z enokanalnim ventilom za 67,2 % manjša in znaša samo 82 N. Pojav histereze pri testu s pretokom 1000 l/min je izginil. Dvokanalni ventil ima večjo pretočno površino med vstopnim kanalom in obročastim delom, temu ustrezno pa je manjši tudi pretočni upor. Tlačni padec na dvokanalnem ventilu je za 34,7 % manjši kot pri enokanalnem ventilu, kar prinaša tudi pomemben prihranek energije.

Dvokanalna konstrukcija zmanjša neravnotežno silo na bat ventila, ne more pa je popolnoma odpraviti. Neravnotežna sila bi s povečanjem pretoka nad 1000 l/min spet zrasla, zato bodo raziskave v prihodnje usmerjene v ventile za zelo velike pretoke (nad 1000 l/min).

(1) Eksperimentalni preizkusi so bili opravljeni v pogojih manjšega in večjega pretoka. Rezultati kažejo, da je pojav histereze posledica pretočnih lastnosti.
(2) Ugotovljena je bila maksimalna radialna neravnotežna sila, ki jo vzdrži bat. Simulacija CFD se je izkazala kot primerna zamenjava za eksperimentalne teste pri večjih ventilih, s tem pa prinaša prihranek časa in denarja.
(3) Pri ventilih za velike pretoke je treba namesto z običajnimi prehodi računati s simetričnimi pretočnimi kanali.

Ključne besede: potni ventil za velike pretoke, radialna neravnotežna sila, histereza, CFD, hidravlično podporje, hidravlični sistem

*Naslov avtorja za dopisovanje: Kolidž za strojništvo, Tehniška univerza v Taiyuanu, Yingze West Avenue 79, Taiyuan, Kitajska, yhb1961@126.com

Strojniški vestnik - Journal of Mechanical Engineering 61(2015)6, SI 68

Prejeto v recenzijo: 2014-09-12
Prejeto popravljeno: 2015-02-05
Odobreno za objavo: 2015-04-22

Superplastično preoblikovanje tristopenjskega polkrogelnega profila iz aluminija 5083

Muthusamy Balasubramanian[1] – Pasupathy Ganesh[2] –
Kalimuthu Ramanathan[3] – Velukkudi Santhanam Senthil Kumar[2,*]

[1] Univerza Anna, Univerzitetni tehniški kolidž, Ramanathapuram, Indija
[2] Univerza Anna, Tehniški kolidž, Guindy, Indija
[3] Kolidž za inženiring in tehnologijo Alagappa Chettiar, Indija

Superplastično preoblikovanje je pomembna tehnologija, primerna za izdelavo delov kompleksnih oblik v eni sami preoblikovalni operaciji in z možnimi aplikacijami v avtomobilski industriji, v letalski in vesoljski industriji, ali pri izdelavi lopatic vetrnih in vodnih turbin. Pri takšnih aplikacijah je dobrodošlo vse obstoječe znanje in informacije o večstopenjskih (tristopenjskih) operacijah superplastičnega preoblikovanja. Ključno vlogo pri procesu superplastičnega preoblikovanja imajo dejavniki, kot so enakomerna porazdelitev debeline, preprečevanje čezmernega tanjšanja in večdimenzijske komponente brez gub. Enakomerna porazdelitev debeline večdimenzijskega profila je npr. nujna za določanje tlaka pri postopku pihanja.

Glavni cilj tega raziskovalnega dela je doseganje maksimalne preoblikovalnosti in enakomerne porazdelitve debeline kompleksnega tristopenjskega polkrogelnega profila, ustvarjenega po postopku superplastičnega preoblikovanja zlitine AA5083 pri konstantnem tlaku. Članek predstavlja tudi napoved porazdelitve debeline v treh območjih orodja z različnimi polmeri na podlagi koeficienta trenja in različnih vstopnih polmerov orodja. Predstavljen je tudi poizkus preiskave superplastičnega preoblikovanja zlitine AA5083 v tristopenjsko (orodje s parametrično zasnovo ima tri različne polmere) polkrogelno kupolo; karakteristike preoblikovanja, kot so preoblikovalna višina, debelina polov, porazdelitev debeline, povprečna debelina, faktor tanjšanja in čas preoblikovanja, pa so preučene kot funkcije tlaka preoblikovanja, koeficienta trenja ter vstopnega polmera orodja v tristopenjskem parametričnem modelu. Tristopenjski postopek superplastičnega preoblikovanja je bil opravljen eksperimentalno in simuliran po metodi končnih elementov (MKE) s paketom ABAQUS. Spremembe profila debeline so bile izmerjene eksperimentalno in z analizo MKE na treh različnih prehodih orodja in pri različnih tlakih. Tlak je bil optimiziran za enakomerno porazdelitev debeline na različnih prehodih orodja in z minimalnim časom preoblikovanja.

Eksperimentalni preizkusi superplastičnega preoblikovanja so bili opravljeni pri različnih tlakih. Pri vsakem so bile uporabljene različne izstopajoče višine za napovedovanje optimalnega tlaka, ki je pomemben za enakomerno porazdelitev debeline. Za vsako izstopajočo višino so bile oblikovane posamezne komponente in določeni parametri, kot so debelina polov, povprečna debelina in faktor tanjšanja. Maksimalni faktor tanjšanja zagotavlja enakomernejšo debelino kompleksnega tristopenjskega profila. Eksperimentalno določeni faktorji tanjšanja in povprečna debelina so pokazali, da obstaja optimalen tlak za enakomerno debelino parametričnega profila, ki znaša 0,5 MPa. Z odmikanjem od optimalnega tlaka se povečuje variabilnost debeline in se oblikujejo nestabilnosti v profilu. Tristopenjske simulacije v enakih pogojih preoblikovanja so pokazale, da je enakomerna debelina profila dosegljiva pri koeficientu trenja pod 0,1 in pri tristopenjskem parametričnem profilu orodja z vstopnim polmerom nad 4 mm.

Rezultati eksperimentov pri konstantnem tlaku so odlični in material je bil v dobrem stiku s površino tristopenjskega polkrogelnega orodja skoraj dokončne oblike, z enakomerno porazdelitvijo debeline brez gubanja v območju treh različnih polmerov. Za primerjavo z eksperimentalnimi rezultati je bila narejena simulacija po MKE s paketom ABAQUS. Rezultati analize po metodi končnih elementov se dobro ujemajo z eksperimentalnimi rezultati glede enakomerne porazdelitve debeline, časa preoblikovanja, tlaka preoblikovanja in stika s površino. Predlagani model parametrične zasnove tristopenjskega polkrogelnega profila zagotavlja enakomerno porazdelitev debeline v eni sami operaciji pihanja z optimalnim tlakom. Na podlagi tega parametričnega modela je mogoče postaviti zahteve za optimalen tlak. Nadaljnje raziskave bi bile lahko usmerjene v razvoj mehatronskega logičnega krmilnega sistema za natančno določanje tlačnega cikla za enakomerno porazdelitev debeline brez gubanja pri večstopenjskih polkrogelnih in kompleksnih pravokotnih komponentah, ki se pojavljajo v mnogih industrijskih aplikacijah.

Ključne besede: postopek superplastičnega preoblikovanja, tristopenjska polkrogelna kupola, eksperiment, MKE, aluminijeva zlitina 5083

*Naslov avtorja za dopisovanje: Univerza Anna, Tehniški kolidž, CEG Campus, Chennai-600 025, Tamil Nadu, Indija, vssk70@gmail.com

Strojniški vestnik - Journal of Mechanical Engineering 61(2015)6, SI 69

Prejeto v recenzijo: 2014-10-08
Prejeto popravljeno: 2015-03-23
Odobreno za objavo: 2015-04-08

Zasnova sistema prečnega stabilizatorja na podlagi hierarhičnega upravljanja

Balázs Varga[1] – Balázs Németh[2] – Péter Gáspár[1,2,*]

[1] Tehniška in ekonomska univerza v Budimpešti, Oddelek za upravljanje transportnih sistemov in vozil, Madžarska
[2] Institut za računalništvo in upravljanje, Laboratorij za sisteme in upravljanje, Madžarska

Članek podaja predlog modela in zasnove krmiljenja aktivnega prečnega stabilizatorja. Namen takšnega sistema je zagotavljanje delovanja aktivnega momenta na šasijo za izboljšanje dinamike gibanja okrog vzdolžne osi. Krmilni sistem mora upoštevati več vidikov. Prvič, kot vrtenja okrog vzdolžne osi vpliva na udobje potnikov v vozilu, prevelik kot pa lahko povzroči nevarnost prevračanja. Drugič, upoštevati moramo tudi kotni pospešek omenjenega gibanja zaradi impulznih vzbujanj. Vzbujanja, ki se prenašajo prek ceste, povzročajo velik kotni pospešek šasije takrat, ko je odklonski kot še majhen. Tretjič, krmilni sistem mora upoštevati omejitve krmilnega toka, ki izhajajo iz lastnosti električnega sistema. Krmiljenje vozila mora torej zagotavljati vse tri lastnosti.

Aktivni prečni stabilizator vpliva na dinamiko vrtenja okrog vzdolžne osi tako, da spreminja togost vzmetenja. Pri tem sistemu krmiljenja je vzmetenje na levi in na desni strani vozila povezano s torzijskimi drogovi. Aktivni prečni stabilizatorji se lahko prilagajajo trenutnemu stanju vozišča in bočnim vplivom ter tako izboljšujejo stabilnost vozila v smeri okrog vzdolžne osi. Dinamika elektrohidravličnega prečnega stabilizatorja je popisana z enačbami dinamike fluidov, elektrike in mehanike. Za namene krmiljenja je bil izpeljan linearni model. Zaradi različnih zahtev in funkcij krmiljenja je smiselna hierarhična zasnova krmiljenja. V hierarhični arhitekturi se dinamika gibanja okrog vzdolžne osi izboljšuje na višjem nivoju z linearno-kvadratičnim (LQ) krmiljenjem z načrtovanim ojačenjem, medtem ko nižji nivo zagotavlja omejevanje vhodov in zagotavlja potrebni moment z omejenim krmiljenjem LQ.

Članek predlaga novosti na višjem in na nižjem nivoju krmiljenja. Na višjem nivoju je kompromis med funkcijami dosežen s spremenljivkami načrtovanja in z rešitvijo metode interpolacije krmiljenja. Omejitve na nižjem nivoju obvladuje preklopna metoda LQ. Zaradi ločitve na dva nivoja v zasnovi upravljanja tudi ni potrebno naknadno preoblikovanje višjenivojskega upravljanja, če pride do sprememb na ravni izvršnih členov.

Delovanje krmilnega sistema prečnega stabilizatorja je predstavljeno s simulacijo. Vpliv vzbujanja prek vozišča in bočnih motilnih sil na kot in pospešek vrtenja šasije okrog vzdolžne osi je minimalen. Iz predstavljenih scenarijev je razvidno, da krmilni sistem izboljšuje dinamiko omenjenega gibanja in obenem obvladuje omejitve vhodov. Možna smer nadaljnjega razvoja aktivnega prečnega stabilizatorja bi bila modularna zasnova relacij med višjim in nižjim nivojem krmiljenja. Takšna zasnova bi lahko povečala učinkovitost izvršnih členov in izboljšala dinamiko gibanja. Naslednji izziv strategije krmiljenja je robustna zasnova: sistemu je lastnih več negotovosti, zato morata biti zagotovljeni zmogljivost in stabilnost v različnih pogojih.

Ključne besede: prečni stabilizator, hidravlični aktuator, načrtovanje ojačenja, LQ, krmilna tehnika v avtomobilih

*Naslov avtorja za dopisovanje: Tehniška in ekonomska univerza v Budimpešti, H-1111, 2. Stoczek utca, Budapest, Medžarska, gaspar.peter@mail.bme.hu

Strojniški vestnik - Journal of Mechanical Engineering 61(2015)6, SI 70

Prejeto v recenzijo: 2015-01-03
Prejeto popravljeno: 2015-03-30
Odobreno za objavo: 2015-04-22

Predlog eksperimentalno-numerične metode za popis trenja pri preoblikovanju pločevine

Tomasz Trzepieciński[1] – Hirpa G. Lemu[2,*]

[1] Tehniška univerza v Rzeszowu, Oddelek za oblikovanje, Poljska
[2] Univerza v Stavangerju, Oddelek za strojništvo in materiale, Norveška

Preoblikovanje delov kompleksnih oblik, kot se pojavljajo npr. pri elementih avtomobilske karoserije, zahteva uporabo orodij z različnimi polmeri in zaokrožitvami robov. Uporaba cilindričnega preizkušanca za modeliranje trenja na zaokroženi površini orodja ne odraža v popolnosti tornih pogojev na robu orodja. Članek zato podaja predlog eksperimentalno-numerične metode za določanje trenja na zaokroženem profilu roba prebijala.

Za simulacijo tornih pogojev na polmerih prebijala in določitev trenja je bil razvit preizkus upogibanja pod napetostjo (BUT), ki je bil izveden v dveh korakih. Vrednosti vlečnih in povratnih nateznih sil so bile najprej določene z vlekom traku prek prosto vrtljivega valja. Sledil je vlek drugega traku prek fiksnega valja za določitev ustreznih vlečnih in povratnih nateznih sil. Opravljene so bile tudi numerične simulacije preizkusa BUT brez trenja v programu ABAQUS, uporabljena pa sta bila elastoplastični pristop z anizotropnim popisom materiala po Hillu in izotropno deformacijsko utrjanje.

Rezultati porazdelitve in vrednosti ekvivalentnih plastičnih deformacij pločevine kažejo maksimalni pritisk na konkavnem profilu, medtem ko so maksimalne plastične deformacije na konveksni strani cilindričnega profila manjše. Torni pogoji, ki so določeni s porazdelitvijo in vrednostjo kontaktnega pritiska, nakazujejo tudi na to, da je razlika v vrednosti maksimalnega kontaktnega tlaka odvisna od podaljšanja preizkušanca. Vrednosti vlečnih in povratnih nateznih sil, ugotovljene v primeru fiksnega valja, imajo največji vpliv na vrednost koeficienta trenja pri analizirani obliki preizkušanca. Vrednost upogibne sile ima manjši vpliv na točnost koeficienta trenja, ki je bila ugotovljena v testu BUT. Rezultati raziskav so tako potrdili, da je predlagana eksperimentalno-numerična metoda uporabna za določanje koeficienta trenja pri orodjih zaokroženega profila.

Glavni problem pri tej raziskavi je bil razvoj realističnega preizkusnega postopka, ki omogoča ločitev tornega upora in upogibnega upora traku na zaokroženih profilih. To je možno le z uporabo cilindričnih preizkušancev, saj necilindrični ne omogočajo izvedbo testa z rotacijskim preizkušancem. Predlagana metoda v članku omogoča določitev koeficienta trenja na zaokroženem robu orodja. Novost je v vrednotenju koeficienta trenja s preizkusom BUT pri preizkušancih necilindričnega profila, ki v predhodnih raziskavah ni bilo ustrezno dokumentirano. Metode zagotavljajo triosno napetostno stanje v kontaktnem področju pločevine z necilindričnim preizkušancem, spremembe površinske topografije pa zato bolje opisujejo realnost kot pri cilindričnih preizkušancih. Znanje o napetostnem stanju na zaokroženih robovih pomembno prispeva k razumevanju narave plastičnih deformacij pločevine na zaokroženem orodju in sprememb topografije.

Ključne besede: upogibanje pod napetostjo, preizkus BUT, metoda končnih elementov, trenje, koeficient trenja, preoblikovanje pločevine

*Naslov avtorja za dopisovanje: Univerza v Stavangerju, Oddelek za strojništvo in materiale, 4036 Stavanger, Norveška; Hirpa.g.lemu@uis.no

Strojniški vestnik - Journal of Mechanical Engineering 61(2015)6, SI 71

Prejeto v recenzijo: 2014-12-10
Prejeto popravljeno: 2015-04-07
Odobreno za objavo: 2015-04-22

Model za ocenjevanje kontaktne temperature zavor

Aleksandar Grkić[1,*] – Davorin Mikluc[1] – Slavko Muždeka[1] – Živan Arsenić[2] – Čedomir Duboka[3]

[1] Vojaška akademija, Univerza za obrambo, Srbija
[2] Univerza v Beogradu, Fakulteta za strojništvo, Srbija
[3] Univerza v Beogradu, Srbija

Glavni cilj tega dela je poiskati rešitev za ocenjevanje temperature na stiku zavor tekom celotne življenjske dobe zavornih ploščic.

Temperatura na kontaktni površini med kolutom in oblogo zavorne ploščice ima velik vpliv na učinkovitost zavor. Če poznamo glavne vplivne dejavnike (t. j. temperaturo na torni površini) ob začetku zaviranja in med zaviranjem, lahko napovedujemo in torej tudi upravljamo izhodne parametre zavor oz. učinkovitost zaviranja. Merjenje temperature tornih površin tekom celotne življenjske dobe zavorne ploščice pa ni prav nič preprosta naloga. Vzrok je v zahtevnih delovnih pogojih zavor, ki vključujejo različne vrste obrabe, prisotnost vode, korozijo in druge vplive. Tudi matematični modeli, s katerimi napovedujemo trenje ali temperaturo stične površine, so pogosto kompleksni in imajo vrsto omejitev.

V članku je razvit ustrezen matematični model za ocenjevanje temperature na stiku drsnih površin zavornega koluta in zavornih ploščic tekom celotnega časa delovanja zavor. V ta namen so bili uporabljeni rezultati in obdelava meritev temperature po globini zavorne ploščice s pomočjo izvirnega matematičnega modela.

Predlagani model za ocenjevanje temperature kontaktne površine zavor je bil razvit na podlagi meritev temperature po globini tornega materiala, vključno s prvim in drugim odvodom temperaturnih sprememb in ustreznimi koeficienti. Koeficienti v modelu predstavljajo hitrost in pospešek intenzitete povečevanja temperature, oz. koeficiente prenosa toplote po tornem materialu. Ti koeficienti so odvisni od sestave tornega materiala zavornih ploščic, obrabnega stanja, geometrije zavor in delovnih pogojev, kakor tudi od položaja termopara T2 v globini tornega materiala. Analiza tako ocenjene oz. izračunane temperature kontaktne površine TE v primerjavi z izmerjeno temperaturo T1 na torni površini je pokazala, da ocenjena temperatura TE zelo dobro sledi obliki in vedenju izmerjene temperature T1, odstopanje od dejanske vrednosti pa ne presega vrednosti ±3 °C.

Predstavljeni model ocenjevanja temperature torne površine je omejen le na zavoro, ki je bila predmet raziskave, velja pa za izbrani torni material in položaj drugega termopara v globini ploščice v danih delovnih pogojih. Izkazalo se je, da lahko s predstavljenim modelom ocenjujemo temperaturo na torni površini tudi pri različnih delovnih pogojih (drsna hitrost, tlak in temperatura), vendar z večjimi odstopanji. Predstavljeni rezultati kažejo očiten zamik med ocenjeno temperaturo in izmerjeno temperaturo kontaktne površine. Razlog za to je prenos toplote skozi torno površino. Z drugimi besedami: na podlagi temperature v ploščicah lahko dobro in natančno ocenjujemo temperaturo torne površine med zaviranjem, ne dobimo pa podatkov o prvih trenutkih zaviranja.

Članek predstavlja oceno temperature torne površine zavor tekom celotne operacije zaviranja. Ocena za temperaturo kontaktne površine je bila pridobljena na podlagi predstavljenega matematičnega modela in ob upoštevanju meritev temperature na določeni globini v ploščici. Prejšnje raziskave potrjujejo, da ocenjena temperatura kontaktne površine dobro sledi dejanski temperaturi, povprečno odstopanje od izmerjene temperature na kontaktni površini pa je ±1 °C.

Ključne besede: ocena temperature, zaviranje, torna površina, meritev, modeliranje

*Naslov avtorja za dopisovanje: Vojaška akademija, Univerza za obrambo, VeljkaLukica-Kurjaka 33, Srbija, iralex@eunet.rs

Strojniški vestnik - Journal of Mechanical Engineering 61(2015)6, SI 72

Prejeto v recenzijo: 2015-02-04
Prejeto popravljeno: 2015-04-22
Odobreno za objavo: 2015-05-06

Preiskava izgub zaradi upora in vrtinčenja olja pri koničnih kotalnih ležajih

Jürgen Liebrecht[1,*] – Xiaojiang Si[2] – Bernd Sauer[1] – Hubert Schwarze[2]

[1] Univerza v Kaiserslauternu, Institut za strojne elemente, zobnike in transmisije, Nemčija
[2] Univerza v Clausthal-Zellerfeldu, Institut za tribologijo in stroje za energetske pretvorbe, Nemčija

Kotalni ležaji so pomembni strojni elementi, ki se uporabljajo v najrazličnejših tehničnih sistemih. Njihova prednost v primerjavi z drsnimi ležaji je v manjšem tornem momentu. To je parameter, ki se uporablja za kvantifikacijo izgub pri kotalnih ležajih. Del izgub povzročajo kontaktne sile med kotalnimi elementi in tekalno površino, kletko in obročem. Drugi del so izgube zaradi upora in vrtinčenja, ki jih povzroča izpodrivanje maziva. Ta del je odvisen od delovnih pogojev in lahko močno vpliva na celoten torni moment, zato ga je treba upoštevati pri izračunu izgub kotalnih ležajev.

Ena od možnosti za zmanjšanje izgub upora in vrtinčenja je z zmanjšanjem oljne kopeli. Pri konstrukcijah in aplikacijah, kjer se z oljem znižuje delovna temperatura, je potrebna večja količina olja. Posledično se povečajo izgube zaradi upora in vrtinčenja, ki jih lahko določamo le približno z enačbami nekaterih proizvajalcev ležajev. Eksperimentalni rezultati kažejo, da natančnejši izračuni terjajo tudi upoštevanje nekaterih drugih vplivov.

Članek predstavlja eksperimentalno študijo in simulacijo za določitev izgub upora in vrtinčenja pri koničnih kotalnih ležajih. Eksperimentalne študije so bile osredotočene na vplive viskoznosti, geometrije kletke, vrste ležaja, vrtilne hitrosti, vsebnosti zraka v mazivu in še posebej na različne nivoje olja. Za zagotavljanje enakomernih robnih pogojev z ozirom na porazdelitev obremenitev in mazivo je bilo razvito preizkuševališče z vertikalno osjo. Izgube zaradi upora in vrtinčenja so bile določene pri različnih nivojih oljne kopeli in pri minimalnem mazanju. Eksperimentalne študije so bile dopolnjene z numeričnimi preiskavami. V ta namen so bile opravljene simulacije CFD, ki pojasnjujejo pomembne vplive in tok fluida v ležaju. Za izračun izgub zaradi izpodrivanja maziva je bila uporabljena metoda količine fluida (VOF). Za modeliranje gibanja kotalnih elementov ležaja je bil uporabljen model spremembe okvirja tranzientni rotor-stator (TRS). Zaradi različnih nivojev olja, ki so bili uporabljeni pri eksperimentih, je bil v simulacije vključen tako enofazni kakor tudi dvofazni tok. Za natančen izračun pretoka je bila uporabljena računska mreža s prilagojeno konturo in približno 2,5 milijona celic. Mreža je v območju znotraj koničnega kotalnega ležaja bistveno bolj fina kot v prostoru zunaj njega.

Rezultati jasno kažejo, kako vrtilna hitrost, viskoznost olja in še posebej nivo olja vplivajo na izgube zaradi upora in vrtinčenja koničnih kotalnih ležajev. Simulacije CFD kažejo tudi natančnost razpoložljivih metod za izračun izgub upora in vrtinčenja. Simulacije kažejo, do kolikšne mere je treba v izračunih upoštevati vsebnost zraka v mazivu, ki nastane zaradi vrtenja ležajnih elementov in se povečuje z vrtilno hitrostjo.

Pri primerjavi rezultatov eksperimentov in simulacije je treba upoštevati poenostavitve glede vsebnosti zraka v mazivu. Za skrajšanje računskega časa pri poplavljenih koničnih kotalnih ležajih so bile uporabljene enofazne simulacije. Vsebnost zraka je bila upoštevana prek modificirane dinamične viskoznosti, ki je bila določena eksperimentalno.

Delo predstavlja pomemben prispevek pri določanju faktorjev izgub zaradi izpodrivanja maziva. Te ugotovitve so nujne za sestavljanje računskega modela določanja izgub zaradi upora in vrtinčenja pri koničnih kotalnih ležajih, ki ne zahteva kompleksnih računskih orodij.

Ključne besede: konični kotalni ležaji, vertikalna os, izgube zaradi vrtinčenja, izgube zaradi upora, torni moment, simulacije CFD

*Naslov avtorja za dopisovanje: Univerza v Kaiserslauternu, Institut za strojne elemente, zobnike in transmisije, Gottlieb-Daimler-Str., 67663 Kaiserslautern, Nemčija, j.liebrecht@mv.uni-kl.de

Strojniški vestnik - Journal of Mechanical Engineering 61(2015)6, SI 73

Prejeto v recenzijo: 2015-01-20
Prejeto popravljeno: 2015-04-02
Odobreno za objavo: 2015-04-22

Izboljšanje elektroerozijske (EDM) obdelave zlitine Ti-6Al-4V z dodatkom grafitnega prahu v dielektriku

Emre Unses[1] – Can Cogun[2,*]

[1]Raziskovalni institut za vesoljske tehnologije TUBITAK, Turčija
[2] Univerza v Cankayi, Tehniška fakulteta, Oddelek za mehatroniko, Turčija

Ti-6Al-4V je ena najbolj razširjenih titanovih zlitin v letalski in vesoljski industriji, spada pa v skupino materialov, ki so zahtevni za obdelavo. Zlitina je manj primerna za konvencionalno obdelavo z odrezavanjem in za elektroerozijsko obdelavo (EDM). Zelo majhna stopnja odvzema materiala pri elektroerozijski obdelavi titanovih zlitin namreč pomeni nesprejemljivo dolg čas obdelave.

Pregled literature je razkril, da ni obstoječih študij vpliva dodatka grafitnega prahu v dielektriku na učinkovitost obdelave zlitine Ti-6Al-4V, ki je zelo priljubljena v letalski in vesoljski industriji. Avtorji prispevka na podlagi svojih izkušenj verjamejo, da se lahko z dodajanjem grafitnega prahu v dielektrik občutno izboljšajo parametri EDM-obdelave zlitine Ti-6Al-4V, kot so stopnja odvzema materiala, obraba elektrode (EWR), relativna obraba (RW) in površinska hrapavost. Grafitni prah je poleg tega cenejši od najcenejših kovinskih in nekovinskih prahov, ki jih najdemo v literaturi (kot so SiC, Al, Ni). Preučen je vpliv dodatka grafitnega prahu v kerozinu (dielektrik) na MRR, EWR, RW in površinsko hrapavost obdelovanca (Ra, Rz(DIN) in topografija površine) v odvisnosti od parametrov ts (50 ms in 100 ms), id (6 A in 12 A) in tlaka izpiranja dielektrika Pd (0,1 bar in 0,4 bar). Pričujoča študija je prvi resnejši poizkus uporabe primesi grafitnega prahu v dielektriku za izboljšanje zmogljivosti potopne elektroerozijske obdelave zlitine Ti-6Al-4V.

Uporabljena je bila zlitina Ti-6Al-4V kvalitete 5 s sestavo: 90% Ti, 5,9% Al, 4% Va, 0,07% Fe, 0,02% C. Za primerjavo vrednosti MRR, EWR, Ra in RW so bili pripravljeni in elektroerozijsko obdelani kosi iz jekla AISI 1040. Elektrode iz elektrolitskega bakra so bile postružene na premer 13 mm in na dolžino 40 mm. Uporabljena je bila koncentracija grafitnega prahu (Cp) 5 g/l, ki daje najboljše rezultate obdelave med preizkušenimi koncentracijami Cp. Eksperimenti s kerozinom (KD) ter z mešanico kerozina in grafitnega prahu (GPMKD) so bili opravljeni v tanku lastne izdelave. Homogena suspenzija grafitnega prahu v tanku med testi je bila dosežena z učinkom mešanja dveh vzporednih bakrenih cevi premera 12 mm (nameščenih spodaj v tanku), preluknjanih z odprtinami premera 2,4 mm. 3D-topografski posnetek obdelanih površin obdelovanca je bil ustvarjen s stereofotometrično tehniko.

Rezultati eksperimenta so privedli do naslednjih zaključkov:

1) Z večanjem Pd se je občutno izboljšala stopnja MRR, stopnja EWR pa se je rahlo povečala tako pri KD kakor tudi pri GPMKD. Sprememba Pd ni imela večjega vpliva na Ra. Ob povečanju ts se je povečala stopnja MRR in zmanjšala stopnja EWR za KD in GPMKD. Spremembe ts niso vplivale na Ra.
2) Obdelava v GPKMD je bila zelo stabilna, obdelane površine pa niso bile kontaminirane z ogljikom, še posebej pri visokih nastavitvah Pd.
3) Elektrolit GPMKD je izboljšal vrednosti MRR, Ra in RW pri obdelovancu Ti-6Al-4V. 3D-topografija obdelane površine pa je razkrila manjšo globino profila pri GPMKD kot pri KD.
4) Čeprav je uporaba GPKMD znatno izboljšala MRR pri Ti-6Al-4V, pa so bile vrednosti MRR v primerjavi z obdelovancem iz jekla AISI 1040 še vedno majhne. Uporaba KD in GPMKD daje bistveno boljše vrednosti Ra za Ti-6Al-4V kot za AISI 1040.

Grafitni prah je vsaj za 70 % cenejši kot drugi kovinski in nekovinski prahovi, ki jih omenjajo viri, zato pa ekonomsko privlačen. Manjša gostota grafitnega prahu v primerjavi z drugimi prahovi omogoča bolj homogeno suspenzijo in s tem stabilnejši režim elektroerozijske obdelave. Avtorji poudarjajo, da je pristop z dodatkom grafitnega prahu v dielektriku mogoče prilagoditi aplikacijam potopne obdelave EDM in vrtanja Ti-6Al-4V v letalski in vesoljski industriji in tako izkoristiti priložnost za izboljšanje učinkovitosti obdelave ter znižanje stroškov.

Ključne besede: elektroerozijska obdelava (EDM), Ti-6Al-4V, grafitni prah, odstranjevanje materiala, obraba orodne elektrode, hrapavost, 3D-topografija površine

*Naslov avtorja za dopisovanje: Univerza v Cankayi, Tehniška fakulteta, Oddelek za mehatroniko, Ankara, Turčija, cogun@cankaya.edu.tr

Doktorske disertacije, specialistično delo, magistrska dela, diplomske naloge

DOKTORSKE DISERTACIJE

Na Fakulteti za strojništvo Univerze v Ljubljani sta obranili svojo doktorsko disertacijo:

- dne *5. maja 2015* **Titina BANJAC** z naslovom: »Enodimenzionalni samo-adaptivni simulacijski model za enovito modeliranje stisljivih in nestisljivih tekočin v termoregulacijskih sistemih motornih vozil« (mentor: izr. prof. dr. Tomaž Katrašnik, somentor: prof. dr. Ferdinand Trenc);

V doktorski nalogi je predstavljen numeričen model termoregulacijskih sistemov motornega vozila, ki je zasnovan kot modularni sestav komponent za povezovanje v poljubne topologije zaprtih sistemov z nestisljivo in stisljivo tekočino. Cilji raziskav za stisljiv in za nestisljiv tok so bili modeli, ki jih odlikuje visoka stopnja natančnosti in napovednovalnosti ob čim krajših računskih časih z ozirom na kriterije sistemskih simulacij. S tem namenom je v modelu hladilnega sistema z nestisljivim medijem razvit numeričen algoritem, ki energijsko enačbo rešuje razklopljeno od enačb tokovnega polja in ki samodejno generira sistem diferencialno algebrajskih enačb z ozirom na poljubno topologijo sistema brez podvojevanja spremenljivk. V modelu hladilnega sistema s stisljivim medijem sta bila implementirana inovativna pristopa: 1.) invertiranje gibalne enačbe in 2.) razvoj samo-adaptivnega algoritma, ki na osnovi lokalne stisljivosti medija v posameznem kontrolnem volumnu obravnava medij kot stisljiv ali nestisljiv, celoten sistem enačb pa je integriran z implicitno shemo z analitično Jakobijevo matriko. Na osnovi primerjav med simuliranimi in izmerjenimi rezultati je bila v delu pokazana visoka stopnja natančnosti modela stisljivega in nestisljivega medija. V primerjavi z drugimi vodilnimi komercialnimi orodji pa smo dokazali krajše računske čase obeh modelov razvitih v okviru doktorskega dela, ki izhajajo iz implementiranih inovativnih pristopov;

- dne *11. maja 2015* **Ana TRAJKOVSKI** z naslovom: »Karakterizacija mehanskih lastnosti ligamentov vratne hrbtenice« (mentor: prof. dr. Ivan Prebil, somentorja: prof. dr. Igor Emri in prof. dr. Marija Hribernik);

Ligamenti vratne hrbtenice imajo življenjsko pomembno vlogo pri zagotavljanju stabilnosti vratne hrbtenice in varnih fizioloških meja gibanja vratu in glave. Zato so raziskave na področju karakterizacije mehanskih lastnosti in numeričnega modeliranja odziva ligamentov vratne hrbtenice zelo pomembne. V predstavljeni študiji je raziskan in s poenostavljenim pristopom numerično modeliran vpliv starosti darovalca na poškodbo treh glavnih ligamentov vratne hrbtenice: sprednjega longitudinalnega ligamenta (ang. Anterior Longitudinal Ligament oz. ALL), zadnjega longitudinalnega ligamenta (ang. Posterior Longitudinal Ligament oz. PLL) in rumenega ligamenta (ang. Ligamentum Flavum oz. LF). Skupno 46 vzorcev človeških ligamentov vratne hrbtenice je bilo 24 do 48 ur po smrti darovalca pripravljenih za izvajanje preizkusov. Opravljeni so bili enoosni natezni preizkusi v smeri poteka vlakenc v fizioloških pogojih na namensko pripravljeni napravi za nateg. Rezultati preizkusov so pokazali značilen vpliv starosti darovalca na nastanek poškodbe preizkušenih ligamentov (največjo silo in raztezek). Mehanski odziv ligamentov vratne hrbtenice je bil modeliran s pomočjo poenostavljenega fenomenološkega modela v področju ‚toe' in linearnem področju. Trend vpliva starosti darovalca na strukturne lastnosti tkiva je bil numerično modeliran s pomočjo snovnih parametrov v funkciji staranja, kar nakazuje pristop k poenostavljenem modeliranju ligamentov vratne hrbtenice v modelih z metodo končnih elementov. Modelu je bila dodana funkcija (spremenljivka) staranja darovalca, tako da numerični model pokaže način popisa mehanskega odziva ligamentov vratne hrbtenice pri starosti darovalca med 20 in 80 let, kljub temu da ne more zajeti fizikalnega ozadja obnašanja materiala.

*

Na Fakulteti za strojništvo Univerze v Mariboru je obranil svojo doktorsko disertacijo:

- dne *20. maja 2015* **Andrej LIKEB** z naslovom: »Primernost obročnega preizkušanca za določitev lomne žilavosti materiala cevovoda« (mentor: prof. dr. Nenad Gubeljak);

Zagotavljanje celovitosti cevovodov je ključnega pomena za varno in zanesljivo oskrbo s kemijskimi in petrokemijskimi substancami. Cevovodi so običajno, za transport zemeljskega plina, konstruirani, kot tankostenske konstrukcije, iz katerih je težko izdelati standardne preizkušance za določanje lomnih materialnih lastnosti. Ker je poznavanje lomnomehanskih materialnih lastnosti ključno za preračun dopustne velikosti napake, je izredno pomembno zagotoviti transparenten pristop merjenja lomne žilavosti, ki ustreza predpisom in navodilom po standardih, kot so: ASTM E-1820, BS 7448, oziroma GKSS procedura. Značilno je, da so v cevovodih

najbolj kritične vzdolžno (aksialno) orientirane razpoke, ki se lahko razvijejo iz raznih vključkov ali napak v materialu cevi, saj so napetosti v vzdolžni smeri dvakrat višje kot v prečni. Ker je določitev lomnih lastnosti z uporabo standardnih preizkušancev v primeru cevovoda, vse prej kot enostavno, je bil kot rešitev za merjenje lomne žilavosti cevovodov v vzdolžni smeri, predlagan obroč z aksialno razpoko kot preizkušanec, ki se odreže iz dela cevi in tritočkovno aksialno upogibno obremeni, ter z uporabo merilne opreme določi lomna žilavosti materiala. Vendar ker je obroč nestandarden preizkušanec, je bilo potrebno dokazati in analizirati, ali lahko obroče uporabimo kot alternativni pristop k merjenju lomnih lastnosti v primerjavi s standardnimi preizkušanci. V doktorski disertaciji je na osnovi eksperimentalnega dela, analitičnega pristopa in numeričnega analiziranja ocenjena primernost obročnega preizkušanca za določitev lomne žilavosti materiala. Rezultati so na osnovi primerjave prikazani, v obliki numeričnih analiz, R odpornostnih krivulj in krivulj gonilne sile rasti razpoke. Preučena je tudi možnost uporabe obroča kot preizkušanca z zarezo za izvajanje meritev, z vsemi pojasnjenimi učinki, ki povzročajo iniciacijo in stabilno rast razpoke. Za konstruiranje diagrama ocenitve sprejemljivosti napake sta numerično določeni funkciji za mejno obremenitev in faktor intenzitete napetosti v odvisnosti od velikosti obroča in dolžine razpoke. V okviru naloge je na enak način določen korekcijski faktor z uporabo separacijske metode v odvisnosti od radija zareze, za določitev plastičnega dela elasto-plastičnega energijskega parametra J-integrala.

*

SPECIALISTIČNO DELO

Na Fakulteti za strojništvo Univerze v Mariboru je z uspehom zagovarjal svoje specialistično delo:

dne 8. maja 2015:

Janez Vilhelm PETAN z naslovom: »Optimizacija proizvodnje uparjalnikov velikih gospodinjskih aparatov« (mentor: prof. dr. Borut Buchmeister).

*

MAGISTRSKA DELA

Na Fakulteti za strojništvo Univerze v Ljubljani so pridobili naziv magister inženir strojništva:

dne 28. maja 2015:

Tomaž LAVRENČIČ z naslovom: »Uporaba hibridnih simulacijskih tehnik pri razvoju krmilnika za električna vozila« (mentor: prof. dr. Peter Butala);

Mario MARINOVIĆ z naslovom: »Krmilni algoritmi za navigacijo avtonomnih mobilnih robotov v ravnini « (mentor: prof. dr. Peter Butala);

Anže VIDIC z naslovom: »Optimizacija srednjetlačne dvižne blazine v virtualnem okolju« (mentor: prof. dr. Marko Nagode);

dne 29. maja 2015:

Patricija BREZOVAR z naslovom: »Razvoj preizkuševališča za avtomatsko karakterizacijo ležajev pralnih strojev« (mentor: prof. dr. Edvard Govekar, somentor: doc. dr. Primož Potočnik);

Bine KRPIČ z naslovom: »Varjenje z gnetenjem aluminijeve zlitine 5024« (mentor: doc. dr. Damjan Klobčar, somentor: izr. prof. dr. Norbert Enzinger);

Matej NOVAK z naslovom: »Izdelava ozobja na velikih aksialnih ležajih« (mentor: prof. dr. Janez Kopač);

Matej VIDIC z naslovom: »Raziskava osnovnih karakteristik pri dispergiranju v industrijskem fermentorju in modelni mešalni napravi « (mentor: doc. dr. Andrej Bombač).

*

Na Fakulteti za strojništvo Univerze v Mariboru je pridobil naziv magister inženir strojništva:

dne 27. maja 2015:

Gregor GRAČNER z naslovom: »Modeliranje sekundarnega sistema v Nuklearni elektrarni Krško« (mentor: izr. prof. dr. Jure Marn).

*

Na Fakulteti za strojništvo Univerze v Mariboru je pridobil naziv magister gospodarski inženir:

dne 27. maja 2015:

Tadej PUNGARTNIK z naslovom: »Napovedovanje proizvodnega programa« (mentorja: izr. prof. dr. Iztok Palčič, doc. dr. Matjaž Iršič).

*

Na Fakulteti za strojništvo Univerze v Mariboru je pridobil naziv magister inženir mehatronike:

dne 27. maja 2015:

Antonio RADIĆ z naslovom: »Modeliranje procesa frezanja več-slojnih kovinskih materialov« (mentorja: doc. dr. Uroš Župerl, izr. prof. dr. Aleš Hace, somentor: prof. dr. Franci Čuš).

*

DIPLOMSKE NALOGE

Na Fakulteti za strojništvo Univerze v Ljubljani je pridobil naziv univerzitetni diplomirani inženir strojništva:

dne 10. aprila 2015:

Gregor JORDAN z naslovom: »Senzorska mreža za spremljanje parametrov okolja za sistem natančnega kmetovanja« (mentor: prof. dr. Peter Butala).

*

Na Fakulteti za strojništvo Univerze v Ljubljani so pridobili naziv diplomirani inženir strojništva:

dne 14. maja 2015:

Janez ARZENŠEK z naslovom: »Uporaba podatkov iz zapisovalnikov zvoka in parametrov leta letalnika za postopek preverjanja letalnostnih sposobnosti s strani pooblaščenih nadzornih organov« (mentor: izr. prof. dr. Tadej Kosel);

Boštjan ROZMAN z naslovom: »Izbira tehnologije za izdelavo pločevinastih polizdelkov« (mentor: doc. dr. Davorin Kramar);

dne 15. maja 2015:

Niko BEVK z naslovom: »Optimizacija zavornega hidravličnega ventila z dvojnim tokokrogom« (mentor: doc. dr. Franc Majdič);

Klemen KOBAL z naslovom: »Vpliv skupne učinkovitosti opreme na vitkost proizvodnje« (mentor: izr. prof. dr. Janez Kušar, somentor: prof. dr. Marko Starbek);

Tomaž PRAPROTNIK z naslovom: »Meroslovna analiza določanja količine kapljevitega goriva v rezervoarjih « (mentor: izr. prof. dr. Ivan Bajsić);

Tadej SEVŠEK z naslovom: »Načrtovanje merilne proge za preizkušanje nevtralizatorjev vodnega kamna« (mentor: izr. prof. dr. Ivan Bajsić).

*

Na Fakulteti za strojništvo Univerze v Mariboru sta pridobila naziv diplomirani inženir strojništva:

dne 26. maja 2015:

Rok SUŠEC z naslovom: »Krmiljenje procesa cementiranja v računalniško vodeni liniji« (mentor: prof. dr. Franc Zupanič);

dne 28. maja 2015:

Denis STAJNKO z naslovom: »Konstruiranje in vzdrževanje priprav v proizvodnji« (mentor: doc. dr. Samo Ulaga).

*

Na Fakulteti za strojništvo Univerze v Ljubljani je pridobil naziv diplomirani inženir strojništva (VS):

dne 14. maja 2015:

Davor BENKOVIĆ z naslovom: »Analiza cikličnih variacij procesa zgorevanja ob uporabi različnih plinskih goriv v motorju z notranjim zgorevanjem s prisilnim vžigom« (mentor: izr. prof. dr. Tomaž Katrašnik).

*

Na Fakulteti za strojništvo Univerze v Mariboru je pridobil naziv diplomirani inženir strojništva (VS):

dne 28. maja 2015:

Rok VENGUST z naslovom: »Izdelava polžne dvojice« (mentor: doc. dr. Mirko Ficko).

*

Na Fakulteti za strojništvo Univerze v Mariboru je pridobil naziv diplomirani inženir mehatronike (VS):

dne 28. maja 2015:

Matija SEKIRNIK z naslovom: »Priprava robotiziranega sistema ACMA XR701 in obračalne mize za postopke 3D frezanja« (mentorja: izr. prof. dr. Karl Gotlih, izr. prof. dr. Aleš Hace).

Information for Authors

All manuscripts must be in English. Pages should be numbered sequentially. The manuscript should be composed in accordance with the Article Template given above. The maximum length of contributions is 10 pages. Longer contributions will only be accepted if authors provide juastification in a cover letter. For full instructions see the Information for Authors section on the journal's website: http://en.sv-jme.eu .

SUBMISSION:

Submission to SV-JME is made with the implicit understanding that neither the manuscript nor the essence of its content has been published previously either in whole or in part and that it is not being considered for publication elsewhere. All the listed authors should have agreed on the content and the corresponding (submitting) author is responsible for having ensured that this agreement has been reached. The acceptance of an article is based entirely on its scientific merit, as judged by peer review. Scientific articles comprising simulations only will not be accepted for publication; simulations must be accompanied by experimental results carried out to confirm or deny the accuracy of the simulation. Every manuscript submitted to the SV-JME undergoes a peer-review process.

The authors are kindly invited to submit the paper through our web site: http://ojs.sv-jme.eu. The Author is able to track the submission through the editorial process - as well as participate in the copyediting and proofreading of submissions accepted for publication - by logging in, and using the username and password provided.

SUBMISSION CONTENT:

The typical submission material consists of:

- A **manuscript** (A PDF file, with title, all authors with affiliations, abstract, keywords, highlights, inserted figures and tables and references),
- Supplementary files:
  - a **manuscript** in a WORD file format
  - a **cover letter** (please see instructions for composing the cover letter)
  - a ZIP file containing **figures** in high resolution in one of the graphical formats (please see instructions for preparing the figure files)
  - possible **appendicies** (optional), cover materials, video materials, etc.

Incomplete or improperly prepared submissions will be rejected with explanatory comments provided. In this case we will kindly ask the authors to carefully read the Information for Authors and to resubmit their manuscripts taking into consideration our comments.

COVER LETTER INSTRUCTIONS:

Please add a **cover letter** stating the following information about the submitted paper:

1. Paper **title**, list of **authors** and their **affiliations**.
2. **Type of paper**: original scientific paper (1.01), review scientific paper (1.02) or short scientific paper (1.03).
3. A **declaration** that neither the manuscript nor the essence of its content has been published in whole or in part previously and that it is not being considered for publication elsewhere.
4. State the **value of the paper** or its practical, theoretical and scientific implications. What is new in the paper with respect to the state-of-the-art in the published papers? Do not repeat the content of your abstract for this purpose.
5. We kindly ask you to suggest at least two **reviewers** for your paper and give us their names, their full affiliation and contact information, and their scientific research interest. The suggested reviewers should have at least two relevant references (with an impact factor) to the scientific field concerned; they should not be from the same country as the authors and should have no close connection with the authors.

FORMAT OF THE MANUSCRIPT:

The manuscript should be composed in accordance with the Article Template. The manuscript should be written in the following format:

- A **Title** that adequately describes the content of the manuscript.
- A list of **Authors** and their **affiliations**.
- An **Abstract** that should not exceed 250 words. The Abstract should state the principal objectives and the scope of the investigation, as well as the methodology employed. It should summarize the results and state the principal conclusions.
- 4 to 6 significant **key words** should follow the abstract to aid indexing.
- 4 to 6 **highlights;** a short collection of bullet points that convey the core findings and provide readers with a quick textual overview of the article. These four to six bullet points should describe the essence of the research (e.g. results or conclusions) and highlight what is distinctive about it.
- An **Introduction** that should provide a review of recent literature and sufficient background information to allow the results of the article to be understood and evaluated.
- A **Methods** section detailing the theoretical or experimental methods used.
- An **Experimental section** that should provide details of the experimental set-up and the methods used to obtain the results.
- A **Results** section that should clearly and concisely present the data, using figures and tables where appropriate.
- A **Discussion** section that should describe the relationships and generalizations shown by the results and discuss the significance of the results, making comparisons with previously published work. (It may be appropriate to combine the Results and Discussion sections into a single section to improve clarity.)
- A **Conclusions** section that should present one or more conclusions drawn from the results and subsequent discussion and should not duplicate the Abstract.
- **Acknowledgement** (optional) of collaboration or preparation assistance may be included. Please note the source of funding for the research.
- **Nomenclature** (optional). Papers with many symbols should have a nomenclature that defines all symbols with units, inserted above the references. If one is used, it must contain all the symbols used in the manuscript and the definitions should not be repeated in the text. In all cases, identify the symbols used if they are not widely recognized in the profession. Define acronyms in the text, not in the nomenclature.
- **References** must be cited consecutively in the text using square brackets [1] and collected together in a reference list at the end of the manuscript.
- **Appendix(-icies)** if any.

SPECIAL NOTES

Units: The SI system of units for nomenclature, symbols and abbreviations should be followed closely. Symbols for physical quantities in the text should be written in italics (e.g. *v*, *T*, *n*, etc.). Symbols for units that consist of letters should be in plain text (e.g. ms^{-1}, K, min, mm, etc.). Please also see: http://physics.nist.gov/cuu/pdf/sp811.pdf .

Abbreviations should be spelt out in full on first appearance followed by the abbreviation in parentheses, e.g. variable time geometry (VTG). The meaning of symbols and units belonging to symbols should be explained in each case or cited in a **nomenclature** section at the end of the manuscript before the References.

Figures (figures, graphs, illustrations digital images, photographs) must be cited in consecutive numerical order in the text and referred to in both the text and the captions as Fig. 1, Fig. 2, etc. Figures should be prepared without borders and on white grounding and should be sent separately in their original formats. If a figure is composed of several parts, please mark each part with a), b), c), etc. and provide an explanation for each part in Figure caption. The caption should be self-explanatory. Letters and numbers should be readable (Arial or Times New Roman, min 6 pt with equal sizes and fonts in all figures). Graphics (submitted as supplementary files) may be exported in resolution good enough for printing (min. 300 dpi) in any common format, e.g. TIFF, BMP or JPG, PDF and should be named Fig1.jpg, Fig2.tif, etc. However, graphs and line drawings should be prepared as vector images, e.g. CDR, AI. Multi-curve graphs should have individual curves marked with a symbol or otherwise provide distinguishing differences using, for example, different thicknesses or dashing.

Tables should carry separate titles and must be numbered in consecutive numerical order in the text and referred to in both the text and the captions as Table 1, Table 2, etc. In addition to the physical quantities, such as *t* (in italics), the units [s] (normal text) should be added in square brackets. Tables should not duplicate data found elsewhere in the manuscript. Tables should be prepared using a table editor and not inserted as a graphic.

REFERENCES:

A reference list must be included using the following information as a guide. Only cited text references are to be included. Each reference is to be referred to in the text by a number enclosed in a square bracket (i.e. [3] or [2] to [4] for more references; do not combine more than 3 references, explain each). No reference to the author is necessary.

References must be numbered and ordered according to where they are first mentioned in the paper, not alphabetically. All references must be complete and accurate. Please add DOI code when available. Examples follow.

Journal Papers:

Surname 1, Initials, Surname 2, Initials (year). Title. Journal, volume, number, pages, DOI code.

[1] Hackenschmidt, R., Alber-Laukant, B., Rieg, F. (2010). Simulating nonlinear materials under centrifugal forces by using intelligent cross-linked simulations. *Strojniški vestnik - Journal of Mechanical Engineering,* vol. 57, no. 7-8, p. 531-538, DOI:10.5545/sv-jme.2011.013.

Journal titles should not be abbreviated. Note that journal title is set in italics.

Books:

Surname 1, Initials, Surname 2, Initials (year). Title. Publisher, place of publication.

[2] Groover, M.P. (2007). *Fundamentals of Modern Manufacturing*. John Wiley & Sons, Hoboken.

Note that the title of the book is italicized.

Chapters in Books:

Surname 1, Initials, Surname 2, Initials (year). Chapter title. Editor(s) of book, book title. Publisher, place of publication, pages.

[3] Carbone, G., Ceccarelli, M. (2005). Legged robotic systems. Kordić, V., Lazinica, A., Merdan, M. (Eds.), Cutting Edge Robotics. Pro literatur Verlag, Mammendorf, p. 553-576.

Proceedings Papers:

Surname 1, Initials, Surname 2, Initials (year). Paper title. Proceedings title, pages.

[4] Štefanić, N., Martinčević-Mikić, S., Tošanović, N. (2009). Applied lean system in process industry. *MOTSP Conference Proceedings*, p. 422-427.

Standards:

Standard-Code (year). Title. Organisation. Place.

[5] ISO/DIS 16000-6.2:2002. *Indoor Air – Part 6: Determination of Volatile Organic Compounds in Indoor and Chamber Air by Active Sampling on TENAX TA Sorbent, Thermal Desorption and Gas Chromatography using MSD/FID.* International Organization for Standardization. Geneva.

WWW pages:

Surname, Initials or Company name. Title, from http://address, date of access.

[6] Rockwell Automation. Arena, from *http://www.arenasimulation.com,* accessed on 2009-09-07.

EXTENDED ABSTRACT:

When the paper is accepted for publishing, the authors will be requested to send an **extended abstract** (approx. one A4 page or 3500 to 4000 characters). The instruction for composing the extended abstract are published on-line: http://www.sv-jme.eu/information-for-authors/ .

COPYRIGHT:

Authors submitting a manuscript do so on the understanding that the work has not been published before, is not being considered for publication elsewhere and has been read and approved by all authors. The submission of the manuscript by the authors means that the authors automatically agree to transfer copyright to SV-JME when the manuscript is accepted for publication. All accepted manuscripts must be accompanied by a Copyright Transfer Agreement, which should be sent to the editor. The work should be original work by the authors and not be published elsewhere in any language without the written consent of the publisher. The proof will be sent to the author showing the final layout of the article. Proof correction must be minimal and executed quickly. Thus it is essential that manuscripts are accurate when submitted. Authors can track the status of their accepted articles on http://en.sv-jme.eu/.

PUBLICATION FEE:

Authors will be asked to pay a publication fee for each article prior to the article appearing in the journal. However, this fee only needs to be paid after the article has been accepted for publishing. The fee is 240.00 EUR (for articles with maximum of 6 pages), 300.00 EUR (for articles with maximum of 10 pages), plus 30.00 EUR for each additional page. The additional cost for a color page is 90.00 EUR. These fees do not include tax.

Strojniški vestnik -Journal of Mechanical Engineering
Aškerčeva 6, 1000 Ljubljana, Slovenia,
e-mail: info@sv-jme.eu

9 770039 248001
ISSN 0039-2480

http://www.sv-jme.eu

Contents

Papers